

# **Development of a tuneable few-femtosecond ultraviolet source up to 50 kHz repetition rate**

Dissertation  
zur Erlangung des Doktorgrades  
an der Fakultät für Mathematik, Informatik und Naturwissenschaften  
Fachbereich Physik  
der Universität Hamburg

vorgelegt von  
Laura Silletti

Hamburg  
2024



Gutachter/innen der Dissertation:	Prof. Dr. Francesca Calegari Prof. Dr. Markus Drescher
Zusammensetzung der Prüfungskommission:	Prof. Dr. Francesca Calegari Prof. Dr. Tobias Herr Prof. Dr. Markus Drescher Prof. Dr. Tais Gorkhover
Vorsitzende/r der Prüfungskommission:	Prof. Dr. Daniela Pfannkuche
Datum der Disputation:	06.12.2024
Vorsitzender des Promotionsausschusses Physik:	Prof. Dr. Markus Drescher
Leiter des Fachbereichs Physik:	Prof. Dr. Wolfgang J. Parak
Dekan der Fakultät MIN:	Prof. Dr.-Ing. Norbert Ritter



# Abstract

Ultraviolet (UV) light plays a crucial role across various scientific fields such as biochemistry, material science and nanotechnology. Producing and using UV pulses with sub-5 fs durations is extremely demanding, but offers new possibilities for studying electron dynamics in light-induced biochemical reactions.

This thesis presents a tuneable ultrafast UV source operating at high repetition rates (up to 50 kHz), designed to be the key component of a table-top few-femtosecond UV-pump and IR-probe beamline to perform time-resolved spectroscopy measurements. Firstly, pulse post-compression of 150 fs pulses with a pulse energy of 250  $\mu$ J, provided by an ytterbium (Yb)-based fibre laser system, down to 20 fs with 90% throughput is achieved via a conventional single-stage multi-pass cell (MPC) filled with 1.4 bar krypton gas. Limited by the narrow bandwidth of the cell mirrors, dispersion-engineered cell mirrors are utilised for the direct control of dispersion inside the MPC to enhance nonlinear spectral broadening based on self-phase modulation (SPM). Through this approach, pulse compression down to 15 fs within a compact single-stage MPC is demonstrated, maintaining an overall throughput of  $> 90\%$ . Additionally, the average power and repetition rate scalability up to 50 W and 200 kHz, respectively, of this method is proven while preserving the spectral broadening characteristics of the output beam.

These short pulses are subsequently used to drive resonant dispersive wave (RDW) emission via a 1.7 meter long hollow-core fibre, filled with argon gas in a negative pressure gradient. A tuneability range of the RDW from 270 nm to 530 nm at 1 and 10 kHz repetition rate is demonstrated, with a transform limited UV pulse of about 3 fs and microjoule level pulse energy at the shortest wavelength. It is also shown that at 50 kHz repetition rate the tuneability range is limited to 370 nm due to the onset of filamentation at higher gas pressures. Moreover, the overall design of the UV-pump and IR-probe beamline is presented, which will benefit statistically demanding experiments.



# Zusammenfassung

Ultraviolettes (UV) Licht spielt eine entscheidende Rolle in verschiedenen wissenschaftlichen Bereichen wie der Biochemie, den Materialwissenschaften und der Nanotechnologie. Die Erzeugung und Nutzung von UV-Pulsen mit sub-5 fs Dauer ist äußerst anspruchsvoll, bietet jedoch neue Möglichkeiten zur Untersuchung der Elektronendynamik in lichtinduzierten biochemischen Reaktionen.

Diese Arbeit präsentiert eine abstimmbare, ultraschnelle UV-Quelle, die bei hohen Wiederholraten (bis zu 50 kHz) arbeitet und als Schlüsselkomponente einer kompakten UV-Pump und IR-Probe Strahlführung für zeitaufgelöste spektroskopische Messungen entwickelt wurde. Zunächst wird eine Pulskompression von 150 fs langen Pulsen mit einer Pulsenergie von 250  $\mu$ J, die von einem auf Ytterbium (Yb) basierenden Faserlasersystem bereitgestellt werden, auf 20 fs mit einem Durchsatz von 90% mittels einer einzelnen herkömmlichen Multi-Pass-Zelle (MPC) demonstriert, die mit 1.4 bar Krypton gefüllt ist. Da die Bandbreite der Zellspiegel begrenzt ist, werden dispersionsoptimierte Zellspiegel verwendet, um die Dispersion innerhalb der MPC direkt zu steuern und die nichtlineare spektrale Verbreiterung basierend auf Selbstphasenmodulation (SPM) zu verstärken. Durch diesen Ansatz wird eine Pulskompression auf 15 fs in einer einzelnen kompakten MPC erreicht, wobei ein Gesamtdurchsatz von  $> 90\%$  beibehalten wird. Zusätzlich wird die Skalierbarkeit der durchschnittlichen Leistung und Wiederholrate auf bis zu 50 W und 200 kHz nachgewiesen, während die spektralen Eigenschaften der Ausgangsstrahlen erhalten bleiben. Diese kurzen Pulse werden anschließend verwendet, um mittels einer 1.7 Meter langen Hohlkernfaser, welche mit Argongas in einem negativen Druckgradienten gefüllt ist, die resonante Dispersionswellen-Emission (RDW) anzutreiben. Ein Abstimmungsbereich der RDW von 270 nm bis 530 nm bei einer Wiederholrate von 1 und 10 kHz wird demonstriert, mit einem Fourier-begrenzten UV-Puls von etwa 3 fs und einer Pulsenergie im Mikrojoule-Bereich. Es wird auch gezeigt, dass bei einer Wiederholrate von 50 kHz der Abstimmungsbereich aufgrund der Filamentierung bei höheren Gasdrücken auf 370 nm begrenzt ist. Darüber hinaus wird das Gesamtdesign der UV-Pump und

IR-Probe Strahlführung vorgestellt, das statistisch anspruchsvollen Experimenten zugutekommen wird.

# Contents

<b>Abstract</b>	<b>v</b>
<b>Zusammenfassung</b>	<b>vii</b>
<b>List of Figures</b>	<b>xii</b>
<b>List of Tables</b>	<b>xiii</b>
<b>1 Introduction</b>	<b>1</b>
<b>2 Fundamentals of Nonlinear Optics</b>	<b>5</b>
2.1 Nonlinear optics in MPCs . . . . .	5
2.1.1 Dispersion . . . . .	6
2.1.2 Third-order nonlinear effects . . . . .	8
Optical Kerr effect . . . . .	9
Self-Phase Modulation . . . . .	10
Self-action effects . . . . .	12
<b>3 Multi-pass Cell compressor</b>	<b>13</b>
3.1 Pulse post-compression . . . . .	13
3.2 Principle of Herriott-type MPC . . . . .	16
3.2.1 Basic parameters of Herriott-type MPC . . . . .	19
3.2.2 MPC Design and Numerical Modeling . . . . .	21
3.3 State-of-the-art MPC compressors . . . . .	23
3.4 Single-stage gas-based MPC . . . . .	26
3.4.1 Experimental setup . . . . .	26
3.4.2 Conventional MPC . . . . .	30
3.5 Conclusion . . . . .	35
<b>4 Dispersion control in MPC</b>	<b>37</b>
4.1 Principle of dispersion management . . . . .	37
4.2 Scaling of post-compressed pulse duration . . . . .	40
4.2.1 Overpressure chamber . . . . .	42

4.2.2	Dispersion-engineered MPC . . . . .	44
4.3	Scaling in average power . . . . .	49
4.4	Conclusion . . . . .	51
4.5	Improvement work . . . . .	52
<b>5</b>	<b>Few-femtosecond UV generation in HCF</b>	<b>55</b>
5.1	Introduction . . . . .	55
5.2	Principle of optical solitons and RDW emission . . . . .	57
5.3	MPC driven resonant dispersive wave emission in a hollow-core fibre . . . . .	60
5.3.1	Experimental setup . . . . .	61
5.3.2	RDW tuneability range . . . . .	63
5.3.3	Scaling in average power . . . . .	66
5.4	Conclusion and Improvement work . . . . .	69
5.5	Outlook on UV-pump and IR-probe beamline . . . . .	70
<b>6</b>	<b>Conclusions</b>	<b>75</b>
	<b>Appendix</b>	<b>79</b>
	<b>Bibliography</b>	<b>81</b>
	<b>Publications and Conferences</b>	<b>93</b>
	<b>Declaration on oath</b>	<b>95</b>

# List of Figures

2.1	Kerr-effect induced self-phase modulation. . . . .	11
3.1	Sketch of SPM-based pulse post-compression principle. . . . .	14
3.2	Characteristic Herriott pattern and geometry of a standard symmetric MPC. . . . .	19
3.3	Schematic of the overall pulse compression setup incorporating a single-stage conventional MPC. . . . .	26
3.4	Characteristics of the laser pulse. . . . .	27
3.5	Layout of the conventional Herriott-type MPC assembled inside a vacuum chamber. . . . .	28
3.6	Specifications of the dielectric compressor mirrors. . . . .	29
3.7	Specifications of the broadband DCM pair. . . . .	30
3.8	Coating specifications of the standard quarter-wave stack multilayer mirrors used in the conventional multi-pass cell configuration. . . . .	31
3.9	Spectral broadening evolution of the conventional MPC achieved for two types of noble gases at 1 kHz. . . . .	32
3.10	Output pulse characteristics of the conventional MPC configuration at 1 kHz. . . . .	33
3.11	Comparison between 3D-simulation and experimental output of the conventional MPC. . . . .	34
4.1	Concept figure of SPM-based spectral broadening in a normal dispersive medium compared to a dispersion-balanced scheme. . . . .	38
4.2	Modified schematic of the overall pulse compression setup introducing two MPC configurations: a dispersion-engineered and a dispersion-optimised MPC. . . . .	40
4.3	Numerical simulations based on the 3D model for two different dispersion-balanced MPC configurations. . . . .	42
4.4	Technical drawing of the compact overpressure chamber utilised for the MPC. . . . .	43

4.5	Custom coating design of the dispersive mirrors used as cavity mirrors in the dispersion-engineered MPC. . . . .	44
4.6	Output pulse characteristics of the dispersion-engineered MPC (setup 1) at 1 kHz repetition rate and 122 $\mu\text{J}$ input pulse energy. . . . .	46
4.7	Output pulse characteristics of the dispersion-optimised MPC (setup 2) at 1 kHz repetition rate and 250 $\mu\text{J}$ input energy. . . . .	47
4.8	Output beam profile characteristics of the dispersion-optimised MPC configuration (setup 2). . . . .	48
4.9	Sketch of the pulse selection modules of the laser incorporating two optical modulators. . . . .	49
4.10	Comparison of measured MPC output spectra detected at different repetition rates, ranging from 1 kHz to 200 kHz. . . . .	50
4.11	Comparison of MPC output pulse energy and output pulse duration achieved in this work with results of previous works utilising Yb-based laser systems centred at 1030 nm. . . . .	52
5.1	Generated spectrum at the output of a hollow-core fibre operated in negative pressure gradient at 1 kHz repetition rate. . . . .	59
5.2	Overall experimental setup comprising a 1.7 m long gas-filled hollow-core fibre with a core size of 200 $\mu\text{m}$ , pumped by sub-20 fs pulses from a multi-pass cell for resonant dispersive wave emission. . . . .	62
5.3	Tuneability range of RDW emission in a hollow-core fibre acquired in argon in negative pressure gradient configuration at 1 kHz repetition rate. . . . .	65
5.4	Average power scalability of the resonant dispersive wave centred at about 270 nm wavelength, generated in argon in negative pressure gradient configuration. . . . .	66
5.5	Tuneability range of RDW emission in a hollow-core fibre acquired in argon in negative pressure gradient configuration at 10 kHz and 50 kHz repetition rate. . . . .	68
5.6	Schematic overview of the UV-pump and IR-probe beam paths. . . . .	72
5.7	Example of the UV spectrum measured after four spectral separators. . . . .	73

# List of Tables

3.1	Summary of experimentally achieved pulse post-compression results utilising various configurations of multi-pass cell compressors. . . . .	25
3.2	Spectral bandwidth values tail-to-tail of the conventional MPC configuration generated in krypton and xenon at different gas pressures. . . . .	32
4.1	Summary of pulse post-compression parameters via three different MPC configurations of an Yb-laser centred at 1030 nm wavelength with an initial pulse duration of 150 fs. . . . .	51
5.1	Measured parameters at 1 kHz repetition rate comprehending the gas pressure (in gradient configuration), the input and output power of the HCF, the UV pulse energy, the centre wavelength of the generated RDW and the calculated transform limit (FWHM) of the RDW emitted in the UV. . . . .	64



# Chapter 1

## Introduction

The capability to observe and control ultrafast processes at the molecular level has been the driving force behind advancements in spectroscopy and photochemistry. Time-resolved spectroscopic techniques offer essential insights into the dynamic behaviour of matter, allowing to capture transient states and unravel reaction mechanisms with exceptional temporal precision. In femtochemistry, tracking rapid events like the evolution of molecular structures or the even faster motion of electron density necessitates pump-probe schemes with few-femtosecond to attosecond time resolution [1, 2]. Most commonly, state-of-the-art sources provide radiation in the extreme ultraviolet (XUV) or vacuum ultraviolet (VUV) regime, allowing access to core-level electronic transitions. The high-energy photons, however, can easily damage or ionise biological specimens or delicate organic materials. Instead, broadband ultraviolet (UV) radiation enables the study of electronic processes in neutral molecules [3] since their photon energy is typically lower than the ionisation threshold of most molecules.

In recent years, significant advancements have been made in the development of laser systems to drive these pump-probe experiments. Generally, titanium-sapphire (Ti:Sa)-based sources are used due to their large gain bandwidth [4], allowing for pulse durations in the few-cycle femtosecond regime [5]. Nevertheless, these systems encounter fundamental constraints in reaching high pulse energy and peak power due to thermal issues, limiting them to sub- $\mu$ J pulse energy and sub-10 W average power. While amplification techniques can boost the pulse energy to several joules and maintain short pulse durations, these systems still experience thermal constraints, which limit their repetition rates. An alternative approach is provided by Ytterbium (Yb)-based laser systems, which have demonstrated scalability to

kilowatt (kW) power levels while maintaining high repetition rates and delivering exceptional beam quality and stability [6]. Consequently, these systems are powerful tools for applications that require high average powers and provide a solution to enhance the signal-to-noise ratio (SNR) of experiments driven by lasers. Temporal pulse constraints are, however, imposed by the amplifier gain bandwidth and gain-narrowing effects [7, 8], restricting pulse durations to only hundreds of femtoseconds. This limitation can be addressed by means of nonlinear pulse post-compression techniques, which involve self-phase modulation (SPM)-based spectral broadening followed by removal of accumulated chirp. This requires a medium with cubic nonlinearity, which can be either solid-state or gaseous.

A very well-established and widely used pulse compression method is the use of gas-filled hollow-core fibres (HCFs), first introduced by Nisoli et al. in 1996 [9], which have since shown remarkable achievements. The further development of this technique for Yb-based systems has led to the generation of few-cycle pulses with energies reaching far into the millijoule (mJ) regime [10, 11]. On the downside, fibre-based pulse compression schemes are highly alignment-sensitive and prone to significant pointing instabilities. As a viable alternative to the more traditional hollow-core fibre methods, solid-state or gas-based multi-pass cells (MPCs) offer high efficiency, excellent energy scaling potential, reduced sensitivity to beam pointing issues, and more compact setups [12, 13]. To achieve few-cycle pulse durations with millijoule-level pulse energies at high repetition rates, recent methods often employ meter-long multi-pass cells arranged in a cascaded configuration, which suffer from significant losses in the second stage due to the use of metallic mirrors to cover sufficient spectral bandwidth [14].

Technological advancements in pulse compression methods are essential for producing broadband UV light, as these pulses act as driving source for third-order processes in nonlinear media. An efficient scheme for generating few-femtosecond UV pulses is offered by third harmonic generation in a high-pressure gas cell, driven by 5 fs infrared (IR) pulses. This approach yields sub-2 fs UV pulses spanning from 210 nm to 340 nm with 150 nJ pulse energy [15]. An alternative method to increase UV pulse energy to the millijoule regime is provided by solitonic waves and their dynamics as they propagate through a hollow-core fibre filled with a nonlinear gaseous medium, resulting in resonant dispersive wave (RDW) emission [16]. A remarkable advantage of this method is its capability to spectrally tune the RDW centre

wavelength by simply adjusting the gas pressure and the driving pulse energy, while maintaining UV pulse durations in the few-cycle regime. Since the wavelength tuning is so far limited to the VUV at about 110 nm, other mechanisms, such as high-order harmonic generation (HHG) [17], need to be used for targeting radiation in the XUV spectral region.

The work presented in this thesis aims at developing a table-top tuneable UV-pump and IR-probe beamline with few-femtosecond time resolution by utilising and combining novel techniques for the compression of infrared pulses and the generation of UV light. This thesis will discuss a method for enhancing SPM-based spectral broadening in a gas-based multi-pass cell compressor, demonstrating its effectiveness in generating tuneable UV light in the few-cycle regime through resonant dispersive wave emission in gas-filled hollow-core fibres. In particular, the scalability in average power and repetition rate of the overall setup will be explored.

The thesis outline is organised as follows:

- **Chapter 2** introduces basic physical concepts which are relevant for the understanding of the work performed in this thesis. The focus is particularly set on third-order nonlinear effects, including self-phase modulation.
- In **Chapter 3**, the design principles and applications of multi-pass cell compressors are introduced, following a brief comparison of pulse post-compression techniques. The chapter then presents the initial spectral broadening performance of a custom-designed and fully implemented gas-based MPC system.
- **Chapter 4** introduces a method based on dispersion control to enhance the spectral broadening performance of the gas-based multi-pass cell technology, paving the way for pulse compression reaching the few-cycle regime within a single-stage MPC. Additionally, average power and repetition rate scaling of this MPC configuration will be demonstrated.

- **Chapter 5** is dedicated to the generation of tuneable few-femtosecond UV pulses, which are generated via resonant dispersive wave emission through an argon-filled hollow-core fibre. In particular, it will be shown that the HCF is driven by the short pulses achieved via post-compression after spectral broadening through a dispersion-controlled MPC. The scalability in average power and repetition rate of the fibre setup will also be demonstrated. Moreover, an outlook on the UV-pump and IR-probe beamline will be presented and discussed.
- **Chapter 6** presents a summary and concluding remarks of the work presented in this thesis.

## Chapter 2

# Fundamentals of Nonlinear Optics

Ultrafast optics is the product of nonlinear effects which arise when intense light beams interact with nonlinear media. A variety of interesting phenomena emerge; however, in this chapter the focus is set on those phenomena which are most relevant to this work, specifically third-order effects. Hence, a theoretical description is provided to fully comprehend the experimental findings discussed in the upcoming chapters. Very good insight and detailed explanations of nonlinear optics and its phenomena can be found in, for example, [18, 19, 20], which have been extensively utilised for the writing of this chapter.

## 2.1 Nonlinear optics in MPCs

The propagation of ultrashort pulses in nonlinear dispersive media can be described by means of the Maxwell equations. They are well known and described in detail, for example, in [19, 21]. Starting by treating light as an electromagnetic wave with an electric field vector  $\mathbf{E}$ , the simplified wave equation for an isotropic, nonmagnetic, source-free medium reads

$$\nabla^2 \mathbf{E} = \frac{1}{c^2} \frac{\partial^2 \mathbf{E}}{\partial t^2} + \frac{1}{\epsilon_0 c^2} \frac{\partial^2 \mathbf{P}}{\partial t^2} \quad (2.1)$$

where  $c$  is the speed of light,  $\epsilon_0$  represents the vacuum permittivity and  $\mathbf{P}$  symbolizes the electric polarization. From this equation, the polarization can be expressed by the applied field strength, since new components of the electromagnetic field can originate from time-dependent  $\mathbf{P}$ . Specifically, due to the nonlinear response of a material, when interacting with a high-intensity pulse, the polarization vector can be expanded into higher-order responses

as

$$\mathbf{P} = \epsilon_0 \chi^{(1)} \mathbf{E} + \underbrace{\epsilon_0 \chi^{(2)} \mathbf{E}^2 + \epsilon_0 \chi^{(3)} \mathbf{E}^3 + \dots}_{\mathbf{P}_{NL}} \quad (2.2)$$

with  $\chi^{n>1}, n \in \mathbb{N}$  being the nonlinear susceptibilities, i.e., the higher-order nonlinear response of the medium. For simplicity, we consider linearly polarised light and neglect the tensor nature of  $\chi$ .

In the following subsections, third-order nonlinear effects will be discussed, as they are the main contributors to this work.

### 2.1.1 Dispersion

Before moving on to the description of the nonlinear effect dominating in the MPC compressor, it is crucial to grasp how dispersion affects the laser pulse during propagation, so as to be controlled in an experimental setting. In this regard, the complex representation of the electric field in Fourier space is written as

$$\tilde{E}(\omega) = E_A(\omega) \cdot e^{i\varphi(\omega)} \quad (2.3)$$

with  $E_A(\omega)$  being the electric field amplitude at frequency  $\omega$  and  $\varphi(\omega)$  the spectral phase. This indicates a dependency of the phase on the frequency, i.e., the absolute phase changes across different spectral frequencies. The spectral phase can also be defined in form of the Taylor series expansion around the central frequency  $\omega_0$  as

$$\varphi(\omega) = \sum_{m=0}^{\infty} \frac{(\omega - \omega_0)^m}{m!} \left( \frac{\partial^m}{\partial \omega^m} \varphi(\omega) \right)_{\omega=\omega_0} = \sum_{m=0}^{\infty} \frac{(\omega - \omega_0)^m}{m!} D_m \quad (2.4)$$

for  $m \in \mathbb{N}$ . Hence, a clear dependency of the phase on the dispersion coefficients  $D_m$  is established. Latter can be mathematically evaluated via the  $m$ -th partial derivative of the phase with respect to the spectral frequency around  $\omega_0$ , resulting in an apparent correlation to the refractive index  $n(\omega)$ , i.e.

$$D_m = \left( \frac{\partial^m}{\partial \omega^m} \varphi(\omega) \right)_{\omega=\omega_0} \stackrel{\varphi=k \cdot x}{=} x \left( \frac{\partial^m k(\omega)}{\partial \omega^m} \right)_{\omega=\omega_0} = \frac{x}{c} \left( \frac{\partial^m (\omega \cdot n(\omega))}{\partial \omega^m} \right)_{\omega=\omega_0} \quad (2.5)$$

where  $k(\omega) = \frac{\omega}{c} \cdot n(\omega)$  is the frequency dependent wave number. Since a precise mathematical expression describing  $k$  is not always given, it is helpful to expand it into the Taylor series

$$k(\omega) = k_0 + k_1(\omega - \omega_0) + \frac{1}{2}k_2(\omega - \omega_0)^2 + \frac{1}{6}k_3(\omega - \omega_0)^3 + \dots \quad (2.6)$$

Each dispersion coefficient affects the pulse differently during propagation, as explained in the following:

- $D_0$  describes the carrier phase shift with respect to the envelope. Here, the pulse experiences a linear spectral phase during propagation, and the phase velocity (i.e. propagation velocity of the wavefront)  $v_p = \frac{\omega_0}{k(\omega_0)} = \frac{1}{k_0}$  can be derived.
- $D_1$  is associated with the amplitude's propagation time through a medium with length or thickness  $x$ , i.e., the shift of the envelope, also called group delay (GD), which leads to the estimation of the group velocity  $v_g = \frac{d\omega}{dk} = \frac{1}{k_1}$ .
- $D_2$  describes the pulse propagation with a quadratic spectral phase leading to temporal pulse broadening, i.e., the group delay dispersion (GDD). The acquired group delay is linear, meaning the temporal part of the pulse changes linearly with respect to the frequency (quadratic spectral phase). As a result, while the spectral profile of the pulse stays the same, its temporal profile is altered, leading to a temporal broadening of the initially Fourier transform limited (FTL) pulse and a decrease in peak power. This effect is commonly referred to as chirp. For  $D_2 > 0$  (positive GDD) the term *normal dispersion* is generally used, whereas  $D_2 < 0$  (negative GDD) is referred to as *anomalous dispersion*.
- $D_3$  is the third-order dispersion (TOD) and acquires a quadratic group delay during propagation (cubic spectral phase). It allows for the generation of pre- and post-pulses at the edges of the pulse's temporal profile.
- $D_{m \geq 4}$  are higher order dispersions. Usually they contribute only weakly to the pulse in post-compression techniques like MPCs, and can hence be neglected.

Dispersion is typically introduced transmissively by common optical materials and needs to be compensated for. In some cases, however, it may be favourable to introduce a certain amount of dispersion. Therefore, it is crucial to control the dispersion of materials, especially when targeting short pulses down to the few- femtosecond cycle regime. As the refractive index of the material changes according to the frequency/wavelength of the propagating light (i.e., the propagation velocity of the individual frequencies or wavelengths differs from each other while passing through a medium), a good solution for the estimation of the material dispersion is provided by the Sellmeier equation [22]

$$n(\lambda) = \sqrt{1 + \sum_i \frac{A_i \lambda^2}{\lambda^2 - \lambda_i^2}} \quad , i \in \mathbb{N} \quad (2.7)$$

where  $\lambda$  is the wavelength in  $\mu\text{m}$  units and  $A_i$  are the Sellmeier coefficients related to the resonances occurring at  $\lambda_i$ . This is valid for the case where frequencies are far away from the absorption resonance. A list of coefficients and dispersion values for various materials can be found, for example, in [23].

### 2.1.2 Third-order nonlinear effects

For materials exhibiting inversion symmetry, such as the noble gases used in this work, the second-order susceptibility  $\chi^2$  vanishes and therefore hinders second-order nonlinear effects [18]. Instead, third-order nonlinear effects dominate, reducing the nonlinear polarization response described by 2.2 to

$$\mathbf{P}_{NL} = \epsilon_0 \chi^{(3)} \mathbf{E}^3 . \quad (2.8)$$

Two phenomena arise from eq. 2.8: 1) the interaction of three photons of an applied field with frequency  $\omega$  with a nonlinear medium generates a new photon at three times the frequency  $3\omega$  of the input photons, also called third harmonic generation (THG). For input frequencies that differ from each other, the term four-wave mixing (FWM) is preferably used. 2) The intensity of a propagating monochromatic wave changes the refractive index of the nonlinear medium (Kerr effect), hence giving rise to self-phase modulation (SPM) and other associated effects such as self-steepening and self-focusing.

In the following, we will focus on the latter nonlinear effects (i.e., Kerr effect and SPM), as they are the predominant phenomena in the experiments performed within the framework of this thesis.

### Optical Kerr effect

The optical Kerr effect refers to the variation in refractive index of a medium which is caused by the light intensity, and is characterised by the relation [18, 24]

$$\begin{aligned} n &= n_0 + 2\bar{n}_2 \langle \mathbf{E}^2 \rangle \\ &= n_0 + n_2 I(t) \end{aligned} \quad (2.9)$$

where  $n_0$  symbolises the linear or weak-field refractive index,  $\bar{n}_2$  is the second-order index of refraction outlining the rate at which the refractive index increases with intensity, and  $I$  is the input pulse intensity. The latter can be both time and space dependent, which will impose the same dependency on the refractive index, leading to a modulation of the phase in the first scenario and to lensing behaviour in the second scenario.

The nonlinear refractive index is related to the susceptibility via the effective susceptibility  $\chi_{\text{eff}} = \chi^{(1)} + 3\epsilon_0\chi^{(3)}|\mathbf{E}|^2$ , leading to  $n^2 = 1 + \chi_{\text{eff}}$ . Consequently, the linear and nonlinear refractive indices are connected to the linear and nonlinear susceptibilities through the following equations:

$$n_0 = \sqrt{1 + \chi^{(1)}} \quad (2.10a)$$

$$\bar{n}_2 = \frac{3\chi^{(3)}}{4n_0} \quad (2.10b)$$

$$n_2 = \frac{3}{4n_0^2\epsilon_0c} \chi^{(3)} \quad (2.10c)$$

Refractive index values  $n_2$  for various noble gases at atmospheric pressures can be found, e.g., in [25].

### Self-Phase Modulation

From previous observations, we concluded that phase modulations in the pulse occur when the refractive index is time-dependent. This effect is known as Self-Phase Modulation (SPM) and is of significant relevance for this thesis, as the temporal phase of the input pulse is affected, which consequently leads to spectral broadening. A mathematical description of SPM is achieved by first considering a pulse propagating along  $z$ -direction with an electric field given by

$$E(z, t) = A(z, t)e^{i(k_0z - \omega_0t)} + c.c. \quad (2.11)$$

with the envelope  $A(z, t)$  and with regard to the material properties described by the refractive index in eq. 2.9 for  $I(t) = 2n_0\epsilon_0c|A(z, t)|^2$ . This is valid only under the premise that the medium response to the optical intensity is instantaneous, the medium length is small enough to avoid reshaping of the pulse, and the slowly varying envelope approximation (SVEA) can be applied [18]. The phase variation affected by the medium on the propagating pulse is characterised by

$$\phi_{NL}(t) = -\frac{n_2\omega_0L}{c}I(t) \quad (2.12)$$

after propagation  $z = L$ . Hence, the time-dependent change in phase results in a broader transmitted pulse spectrum compared to the initial one. In this regard, it is convenient to introduce the instantaneous frequency

$$\omega(t) = \omega_0 + \delta\omega(t) \quad (2.13)$$

with the change in instantaneous frequency given by  $\delta\omega(t) = \frac{d}{dt}\phi_{NL}(t)$ . A visual representation of this effect is depicted in figure 2.1. An overall oscillatory modulation in the broadened spectrum is visible due to spectral interference of spectral components generated at different times, arising from the change in instantaneous frequency. Moreover, the two edges of the initial pulse contribute in opposite directions to the spectral broadening, i.e. the leading edge causes red shifting of the spectrum (red line figure 2.1), whereas the trailing edge causes blue shifting (blue line 2.1). Another feature of SPM broadened spectra is described by the green line in figure 2.1, where at the maximum intensity (peak) of the pulse and at its minima no instantaneous frequency shift takes place and contributes mainly to the centre wavelength of the spectrum [26]. A good quantification of the phase shift acquired due

to nonlinear effects during propagation is expressed in the form of the B-integral

$$B = \frac{\omega_0}{c} \int_0^L n_2(z) I(z) dz \stackrel{\lambda=2\pi c/\omega_0}{=} \frac{2\pi}{\lambda} n_2 I_0 L_{eff} \quad (2.14)$$

with the central wavelength in vacuum  $\lambda$ , the input pulse peak intensity  $I_0$ , and the effective length of the nonlinear interaction  $L_{eff}$  [26].

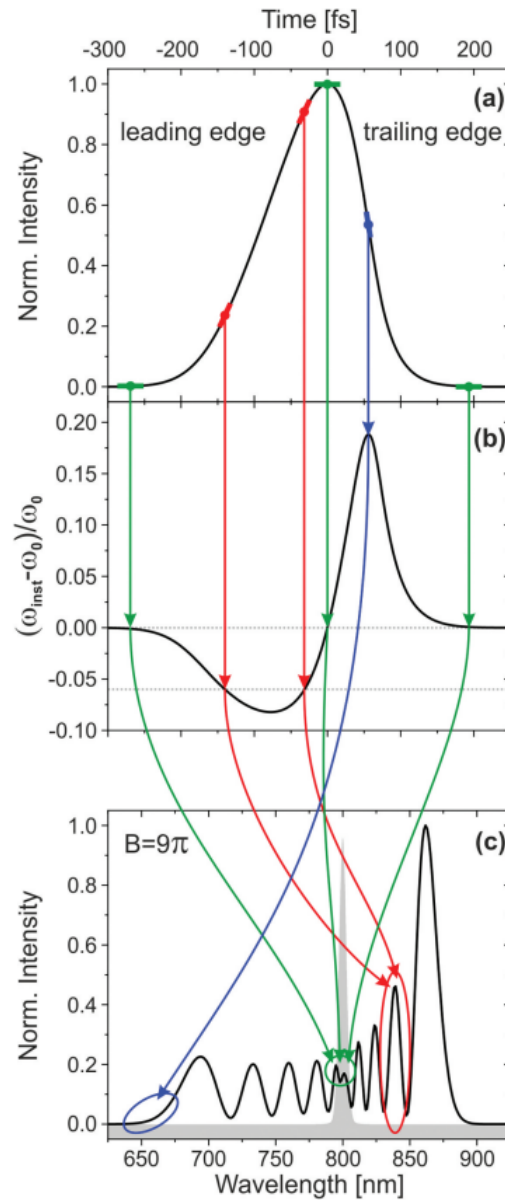


FIGURE 2.1: Kerr-effect induced self-phase modulation with (a) initial pulse shape, (b) instantaneous frequency shift and (c) SPM-based spectrally broadened pulse for B-integral =  $9\pi$  (initial pulse spectrum in the shaded area) [26].

### Self-action effects

Other phenomena arising from the intensity-dependent nonlinear refractive index are so-called self-action effects, which affect the laser pulse in different ways. In the following, a brief description of these effects will be given.

**Self-steepening.** When the nonlinear refractive index changes the group velocity proportionally to the intensity of the pulse, the effect known as Self-steepening arises. This phenomenon manifests itself in the form of a distorted temporal pulse shape. To be precise, the pulse slows down due to high refractive index at its highest energy point (at its peak), whereas towards the low intensity edges of the pulse the velocity is unchanged. This translates to a shift of the peak towards the trailing edge of the pulse, steepening the trailing slope while flattening out the leading edge of the pulse. Hence, in frequency domain SPM-based spectral broadening is generated asymmetrically with larger broadening on the high-frequency part. A prerequisite for the onset of self-steepening is that the pulses need to be short enough (<100 fs).

**Self-focusing.** Despite the temporal and spectral effects introduced by the intensity dependent nonlinear refractive index, it can also modify the spatial beam profile of a laser pulse, leading to Kerr-lensing in the material. This phenomenon is called self-focusing. Upon propagation through a Kerr medium, the centre part of the pulse exhibits a different velocity than at its edges. This results in a position-dependent phase shift where at high intensities the phase is the slowest, and consequently creates a concave curvature of the wavefront, letting the beam self-focus. This process gets continuously stronger until a defocusing/diffraction process counteracts or the material is damaged. For pulses with very high peak power the lensing effect increases until the beam collapses. Therefore, an important threshold is set by the critical power described as

$$P_{cr} = \alpha \frac{\lambda^2}{4\pi n_0 n_2} \quad (2.15)$$

where  $\alpha$  is a constant which needs to be calculated numerically [27]. Hence, self-focusing sets in when the input pulse power  $P$  exceeds the critical power ( $P > P_{cr}$ ).

## Chapter 3

# Multi-pass Cell compressor

There are a variety of techniques to perform laser pulse compression, such as bulk-based methods or via waveguides. In recent years, gas-filled or solid-state-based multi-pass cells have emerged as a promising alternative method, characterised by their high transmission efficiency, energy scaling compatibility, low susceptibility to beam pointing, and relatively compact and cost-efficient setups [12, 13].

In this chapter, a general description of the multi-pass cell concept, taking into account its key parameters and supported by a guide on how to experimentally implement such a compression setup, is provided in the first part. Afterwards, results based on a conventional Herriott-type single-stage MPC, utilising a gaseous medium for nonlinear spectral broadening, are introduced and explained.

### 3.1 Pulse post-compression

Pulse compression has been extensively used for shortening the time duration of laser pulses down to the few-cycle regime, and usually requires light sources already operating on the picosecond (ps) or femtosecond time scale. Often referred to as nonlinear pulse post-compression, the method is based on firstly broadening the pulses spectrally and then compressing them temporally. These steps are essential, as the gain bandwidth of common laser systems is quite narrow, hence requiring spectral broadening to achieve even further temporal compression. A clearer way to relate the frequency and time domains is through the time-bandwidth product (TBP), as described below:

$$TBP \leq \Delta\tau \cdot \Delta\nu \quad (3.1)$$

where  $\Delta\tau$  is the pulse duration,  $\Delta\nu$  represents the spectral bandwidth at full width at half maximum (FWHM), and TBP is a constant determined by the pulse shape, e.g. Gaussian pulses have a TBP of approximately 0.441. When the product of pulse duration and spectral bandwidth is equal to the TBP, the pulses are said to be Fourier-transform limited, i.e., compression to the shortest possible time duration has been achieved. Consequently, the spectra need to be broad enough and unchirped (i.e., having a flat phase throughout the spectrum) in order to generate few-cycle pulses.

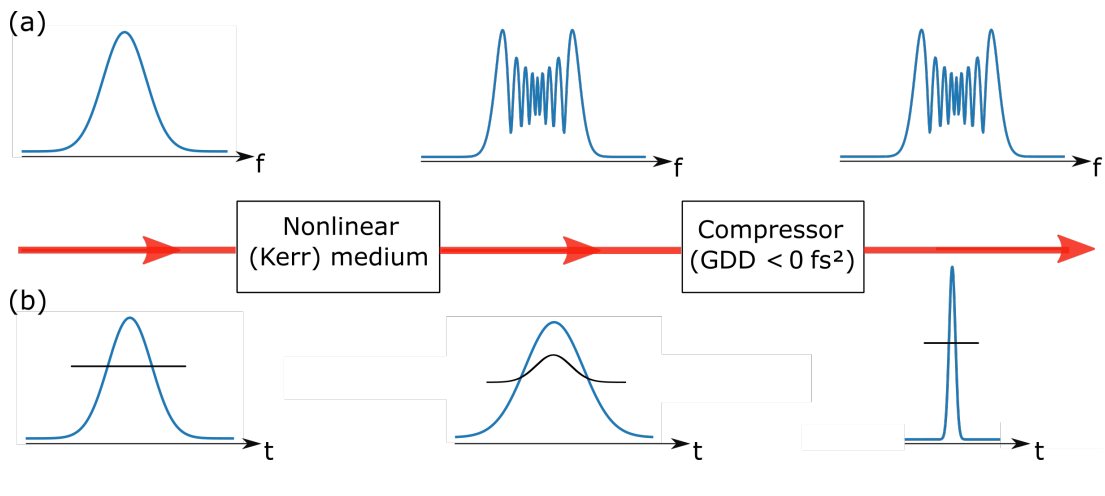


FIGURE 3.1: Sketch of SPM-based pulse post-compression principle, illustrating the evolution of the pulse in (a) frequency domain and (b) time domain with its corresponding temporal phase (black solid line).

A visual explanation of nonlinear post-compression is sketched in figure 3.1, where initially the interaction between an intense pulse and a nonlinear medium gives rise to new spectral components as a consequence of a modulated phase. This broadening process is usually based on self-phase modulation which is triggered by the optical Kerr effect, as described in 2.1.2. As new frequencies are generated, in temporal domain the pulse gets longer due to phase-modulations (positive chirp). According to the relation 3.1, the transform-limited pulse duration is much shorter, which can be achieved with adequate chirp management to bring all the frequencies in phase. Hence, after spectral broadening follows a compression part for the chirp removal by means of materials which introduce chromatic dispersion, such as prism pair, gratings and (dielectric) chirped mirrors [28, 29], just to name a few. In practice, the compressor needs to be designed according to the experimentally acquired nonlinear phase and may include a combination

of various optical elements. Over the years, various techniques have been introduced and explored to approach nonlinear post-compression, which will be discussed in the following.

**Bulk material.** A first attempt of pulse compression of high-power femtosecond pulses was made in 1988 by C. Rolland and P.B. Corkum, where the rather simple method of generating spectral broadening via free space propagation in a nonlinear bulk medium was introduced [30]. Even though a compression down to about 20 fs with up to 110  $\mu\text{J}$  of pulse energy was obtained, this technique suffers from low transmission, amounting to about 4% in this work, and most importantly from spectral inhomogeneity, which directly affects the temporal compression quality of the pulse. A further constraint of this method is the damage threshold of the medium used for spectral broadening, which will be reached if the peak power of the incoming pulse surpasses the critical power. Hence, the beam undergoes self-focusing and introduces damage to the material. These limiting factors can be overcome by distributing the amount of acquired nonlinearity over smaller steps, i.e. a small portion of B-integral is acquired with each step.

**Multi-plate setup.** Already in the year 2000, the theoretical observations made by Milosevic et al. suggested a repeated focusing and defocusing arrangement of optics in combination with bulk Kerr material to improve the spatial homogeneity of the pulse [31]. This work laid the foundation for the multi-plate setup proposed by Lu et al., where thin solid plates with a thickness ranging from 0.05 to 0.5 mm are placed around an intense focusing beam (in the order of  $\text{TW}/\text{cm}^2$ ) for supercontinuum generation [32]. Since the plates are thin enough, the beam can leave the material before collapse, even though the peak power is significantly higher than the critical power and the beam undergoes self-focusing in the Kerr medium. This way the beam focuses right after the plate in air and diverges into a subsequent plate which again experiences self-focusing. The periodic arrangement of such thin plates allows for the generation of an octave-spanning spectrum due to the nonlinearity acquired in each plate, amounting to a B-integral of about 4 to 5 [33, 34], and consequently enabling pulse compression down to the single-cycle regime [35]. This method, however, sets constraints on the energy scalability, which usually does not exceed the sub-mJ level [36].

**Waveguides.** Another approach of pulse compression is based on pulse propagation through a waveguide, such as fibres or capillaries, which circumvents the limitations imposed by a bulk-based Kerr medium. In fact, the spatial properties of the beam are preserved upon propagation through a waveguide, allowing for high intensities over long interaction lengths established by the geometry of the waveguide. This leads to a large accumulation of B-integral, resulting in large spectral broadening. Consequently, the need to operate below the critical power is avoided. Generally, the waveguide characteristics are adjusted to the specifications of the input pulse when it comes to energy scaling. For energy ranges in the order of a few microjoules, solid core photonic-crystal fibres have been successfully used for nonlinear compression in the sub-30 fs regime [37]. Propagation losses are mitigated by keeping the peak power below the self-focusing threshold, which for fused silica amounts to about 4 MW [38], making this fibre suitable for compression of low energy pulses with a high compression factor. Energy scaling beyond 100  $\mu$ J has shown to be possible by employing hollow core fibres filled with noble gases to achieve SPM-based nonlinear spectral broadening [39], and even reaching the millijoule level by using meter long fibres [40, 11]. A record of 1.3 TW in peak power (for ytterbium laser systems) with a pulse energy of 40 mJ after pulse compression has been demonstrated by G. Fan et al., where a 3 meter long gas-filled hollow core fibre with a large core size (a few hundred microns in diameter) has been applied [41]. Even though remarkable achievements are possible with capillaries, they come with limitations set by the ionisation threshold of the employed gas when upscaling the pulse energy, the setups therefore tend to be very long, and are highly susceptible to pointing instabilities.

## 3.2 Principle of Herriott-type MPC

The multi-pass cell compressor is based on the  $\chi^3$  process known as self-phase modulation, which has been explained theoretically in the previous chapter. The generation of new frequencies is achieved by repeatedly focusing the beam into a nonlinear medium, which can be either solid-state based or gaseous. In this way, a small amount of nonlinearity is accumulated with each pass through the medium, resulting in high cumulative nonlinearity, typically exceeding  $B > 3$  rad, and consequently yielding a large spectral bandwidth gain. As the pulses get temporally stretched due to SPM-induced nonlinear phase, compression is generally achieved via external dispersion

compensating dielectric mirrors introducing a negative chirp.

A commonly used approach to enable multiple passes involves employing a Herriott-type cavity geometry, which features two identical focusing mirrors positioned opposite each other, but other geometric configurations are also possible, such as increasing the number of cavity mirrors or using different ROCs. This thesis, however, is based solely on Herriott-type configurations. Generally, Herriott-type multi-pass cells effectively extend the beam propagation length through a nonlinear material in a compact and simple manner. Typical characteristics of such setups include the circular distribution of beam spots on each cell mirror which is dependent on the cell geometry as well as the angle of the incident beam. A key feature of these cavities is their ability to preserve the q-parameter of the beam mode matched to the cavity eigenmode. Moreover, iterative refocusing through the nonlinear medium allows for excellent spatio-spectral homogeneity as the spatial beam content gets redistributed from one focus to another [13].

### Solid-state MPC

In contrast to the multi-plate setup introduced in the previous chapter, which relies on acquiring large B-integral in each bulk material due to Kerr lensing effects (precisely self-focusing), the solid-state MPC creates a focus via curved mirrors to acquire small portions of B-integral with each pass. Most commonly, fused silica is used as nonlinear medium because it offers high optical quality and a relatively high damage threshold. The bulk material can be placed either in air or in vacuum at the centre of the cavity. For non-linearity tuning, however, it is favourable to move the nonlinear material out of focus along the beam propagation direction. Additional nonlinear tuning is achieved by adequately adjusting the thickness of the bulk material itself. The accumulated B-integral per pass needs to be kept low ( $B \ll \pi$ ) in order to preserve the beam parameters matched to the cavity [42]. Moreover, by modifying the characteristics of the employed optics, e.g., reflectivity of the cell mirrors and antireflection coating of the fused silica plates improves the overall pulse energy throughput exceeding 90% [43, 44]. This configuration also allows for operation in different dispersion regimes, namely normal (positive) or anomalous (negative) regime, via careful dispersion management realisable through the amount of GDD introduced by the cell mirror coatings and the dispersion from the bulk material [43, 45, 46]. When it comes to pulse energy upscaling beyond 100  $\mu\text{J}$ , gas-based MPCs are more

practical as they address the limitations imposed by the low LIDT value of bulk materials.

## Gas-based MPC

High pulse peak intensities can be addressed by means of a gaseous nonlinear medium inside a multi-pass cell. Its implementation requires an adequate overpressure chamber, since gas pressures usually exceed several bars. An advantage over solid-state material as nonlinear medium is that gas has comparably higher damage threshold, hence, enabling MPC operations at higher pulse energies for pulses in the femtosecond regime. Contrary to bulk-based MPCs, where the accumulation of nonlinearity is localised in one point (i.e. inside the bulk material), in gas-based MPCs the beam propagates continuously through the nonlinear medium, hence imposing that the peak power of the pulse always needs to be below the self-focusing critical power to prevent beam collapse. The amount of nonlinearity is therefore conditioned by the inherent qualities of the gas and its pressure. Noble gases argon (Ar), krypton (Kr) and xenon (Xe) are the most common choice for gas-filled MPCs which are designed for SPM-based pulse compression, whereas molecular gases such as nitrogen ( $N_2$ ) are the preferred option for Raman induced frequency shifting [47].

Despite the conditions imposed on the pulse peak power, two additional phenomena need to be considered, namely gas ionisation and cell mirror damage, which restrict the minimum beam size in the focus and on the cavity mirrors. Consequently, MPCs are operated close to the stability limit ( $L = 2R$ ) since in this geometry the beam decreases rapidly in the centre ( $w_0$  approaches zero) and expands rapidly on the cell mirrors ( $w_M$  towards infinity), as has been described in [48]. Taking into account these limitations, MPC compressors supporting millijoule-level pulse energies are typically several metres long [49, 50].

Similar to the solid-state MPCs, dispersion control in gas-filled cells is also feasible by, e.g., introducing negative group delay dispersion on the cavity mirrors to balance out the dispersion acquired via SPM while propagating through the nonlinear gas. This is a pivotal step for this thesis and the results will be demonstrated in the next chapter.

### 3.2.1 Basic parameters of Herriott-type MPC

Based on the studies performed in [51], a mathematical description is developed for resonator-like cells which incorporate two concave mirrors with the same radius of curvature (ROC). The following explanations are inspired by the work of A.-L. Viotti et al. [13].

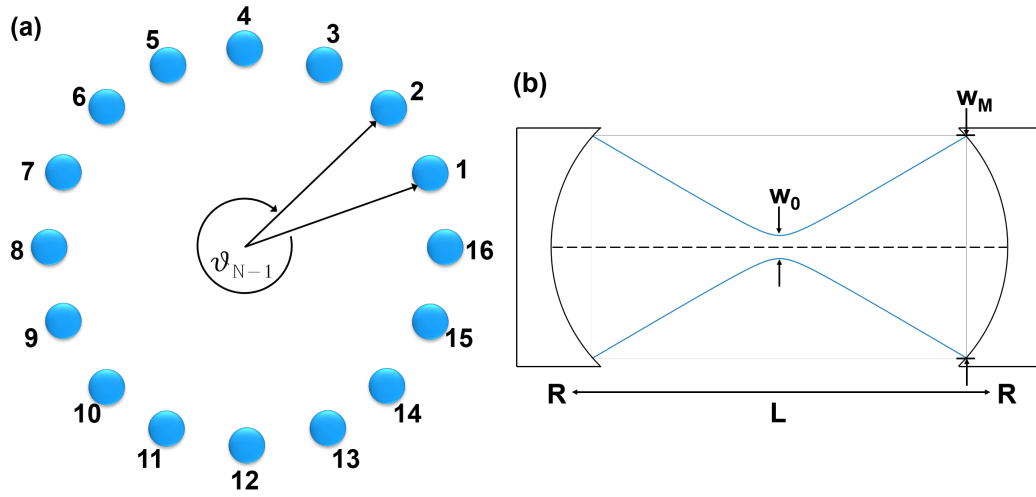


FIGURE 3.2: (a) Characteristic Herriott pattern of a full round trip propagation inside the MPC for  $k = N-1$  configurations. The angular advance of adjacent spots is given by  $\vartheta = 2\pi k/N$ . (b) Geometry of a standard symmetric MPC (modified from [48]).

The beam spot pattern arising from the periodic propagation of the beam through the cell results in a circular shape on each surface of the curved mirror (see figure 3.2). The position of each spot is determined by the radius of curvature  $R$  and the distance  $L$  between the two mirrors. For the re-entrant condition (meaning the initial and final spot overlap), where the angular displacement between successive round trips denoted by  $\vartheta$  accumulates a multiple of  $2\pi$  [51], the following relation must be fulfilled:

$$\vartheta = \frac{2\pi k}{N} \quad (3.2)$$

for  $k = 1, \dots, N - 1$ , with  $N$  symbolising the number of round trips. The length  $L$  can then be determined by the integer  $k$  for fixed ROC and number of round trips via the relation

$$C = \frac{L}{R} = 1 - \cos\left(\frac{\vartheta}{2}\right) = 1 - \cos\left(\frac{\pi k}{N}\right). \quad (3.3)$$

The re-entrant condition dictates that the beam properties are preserved, making these MPC configurations relatively immune to beam-pointing instabilities. In this regard, the input beam needs to be mode-matched to the cavity's eigenmode, which can be mathematically determined by solving equation 6.3 for a Gaussian beam. From this, the quantities focal spot radius  $w_0$  and spot radius  $w_M$  on the cell mirror are derived as follows:

$$w_0^2 = \frac{R\lambda}{2\pi} \sqrt{C(2-C)} = \frac{R\lambda}{2\pi} \sin(\pi k/N) \stackrel{k/N \rightarrow 1}{\approx} \frac{R\lambda}{2N} \quad (3.4)$$

$$w_M^2 = \frac{R\lambda}{\pi} \sqrt{\frac{C}{2-C}} = \frac{R\lambda}{\pi} \tan(\pi k/2N) \stackrel{k/N \rightarrow 1}{\approx} \frac{2R\lambda N}{\pi^2}. \quad (3.5)$$

As can be seen, both quantities are represented by the wavelength  $\lambda$  and the ratio  $C$ , and more specifically by the integer  $k$  and the number of round trips. For typical operation regimes of gas-filled MPCs close to the stability limit defined as  $k = N - 1$  with  $N \rightarrow \infty$ , both equations give an approximate solution, where the focus spot size is minimised and  $w_M$  is maximised. Here, this limit is denoted as  $k/N \rightarrow 1$ . As SPM-based spectral broadening inside MPCs is controlled by the intensity-dependent refractive index change, energy upscaling is possible by reducing the nonlinearity while maintaining the broadening features. Especially for gas-filled MPCs, the nonlinear refractive index is tuneable through the pressure. Limitations, however, are set by the laser-induced damage threshold (LIDT) of the cavity mirrors as well as ionisation threshold of the gaseous medium. Hence, the fluence  $F_m$  on the mirrors as well as the focus peak intensity  $I_0$  are described as

$$F_m = \frac{2E}{R\lambda} \sqrt{\frac{2-C}{C}} = \frac{2E}{R\lambda} \frac{1}{\tan(\pi k/2N)} \stackrel{k/N \rightarrow 1}{\approx} \frac{\pi E}{R\lambda N} \quad (3.6)$$

$$I_0 = \frac{4P}{R\lambda} \frac{1}{\sqrt{C(2-C)}} = \frac{4P}{R\lambda} \frac{1}{\sin(\pi k/N)} \stackrel{k/N \rightarrow 1}{\approx} \frac{4PN}{\pi R\lambda} \quad (3.7)$$

where  $E$  is the pulse energy and  $P$  the pulse peak power. Note that these equations are valid for negligible self-focusing inside MPCs. If the pulse energy is so high as to induce Kerr lensing, the dimensions of the beam spot will be affected and the mode-matching no longer satisfied. As a consequence, the estimated values of  $F_m$  and  $I_0$  become much larger, causing mirror damages and gas ionisation. In the particular case of gas-filled MPCs, self-focusing leads to very small beam dimensions in the focus and on the cell mirrors with each round trip [52].

### 3.2.2 MPC Design and Numerical Modeling

This section will focus on instruction points for the design and implementation of a common Herriott-type multi-pass cell for pulse post-compression, which utilises either gas or bulk material as nonlinear medium, as explained in [13]. Key parameters which need to be taken into account are the nonlinear medium, the ROC of the cell mirrors and their diameter as well as their separation length, the number of round trips, optical coating of the cavity mirrors and the compressor configuration:

1. Depending on the input pulse peak power, the nonlinear medium for achieving spectral broadening is chosen accordingly. Gas-filled multi-pass cells are usually employed for peak powers reaching beyond 100 MW, where the most common choice is the use of noble gases like argon, krypton or xenon. Instead, solid-state MPCs are typically chosen for peak powers up to 1 GW, and utilise antireflection (AR) coated fused silica plates. The gas pressure or bulk thickness is selected according to the input pulse characteristics as well as taking into consideration the subsequent points.
2. Based on equations 3.6 and 3.7, the ROC of the cell mirrors as well as their separation length are chosen as to minimise the fluence on the mirror (below their LIDT value), and decrease the focal peak intensity below the ionisation of the gas/ damage threshold of the bulk material. Note that the ionisation threshold of gases changes according to the type of noble gas and its pressure.
3. For a fixed ROC, the length of the MPC is defined by tuning the parameters  $k$  and  $N$  (number of round trips). Latter is chosen according to the desired compression factor of the entire system. Solid-state MPCs can be operated in  $k < N - 1$  configurations to increase the broadening factor while keeping a short overall length of the system. For gas-filled MPCs, however, it is favourable to operate in a  $k = N - 1$  configuration to maintain the fluence on the mirror low while maximising the spectral broadening.
4. The dimension of the cell mirror is determined by the number of bounces and should be selected to ensure the entire pattern fits within its surface while having sufficient angular separation between neighbouring beam spots to avoid losses upon in- and out-coupling.

5. The next thing to consider is the mirror coating of the cell mirrors as they should be designed in a way to cover the desired spectral bandwidth with highest possible reflectivity. Bulk-based MPCs usually use dispersive cell coatings to compensate for the GDD acquired during propagation through the medium, but also complementary mirror pairs can be employed to reach even larger bandwidth as they introduce a flatter phase over a larger spectral width. In general, standard dielectric quarter-wave stack mirrors with low GDD values are used, which support spectral bandwidths in the sub-30 fs regime in gas-based configurations. However, especially when targeting few-cycle pulses such dielectric mirrors are not sufficient anymore and instead metallic coatings are used to cover a broader spectral range at a cost of transmission efficiency.
6. Once all the multi-pass cell parameters are set, the final step consists in designing the compressor, which is used to compress the commonly positively chirped pulses from the MPC. This can comprise dielectric chirped mirrors or even mirror pairs to cover larger spectral bandwidth with high reflectivity.

**Numerical Modelling.** At this point it is equally important to fully comprehend the effect of nonlinear propagation on the light pulse, which can be described by numerical models. A complete description is provided through a 3D-model introduced and employed by M. Hanna et al. in 2017 [48], which is adaptable to both gas-based and solid-state MPCs. On the basis of a symmetric split-step Fourier algorithm, many phenomena arising from nonlinear propagation are taken into account, comprising diffraction in frequency domain, linear and higher order dispersion, phenomena arising from the optical Kerr effect such as self-phase modulation, self-focusing and self-steepening. This model enables the integration of cell mirror dispersion and reflectivity, as they directly influence the propagation characteristics. The grid size requires adjustment in both spatial domain, to cover the entire beam size in the focus and on the cell mirrors, and temporal domain, to encompass the broadened spectrum along with the initial pulse duration [12, 48], hence expanding the computation time drastically. A simpler and less time-consuming one-dimensional model has been presented alternatively, showing good agreement with the three-dimensional model in predicting both spectral and temporal propagation [53]. In this thesis work, however, the 3D

model has been employed as it has demonstrated to give a more realistic outcome of the experiment. In a collaborative effort, the nonlinear compression in multi-pass cell simulations mentioned in this work were all performed by Esmerando Escoto from the FS-LA group at DESY, Hamburg.

### 3.3 State-of-the-art MPC compressors

Over the past several years, multi-pass cell for pulse post-compression has developed as an attractive alternative to the more conventional methods, as it overcomes many of the limitations mentioned beforehand. Its first experimental demonstration was carried out in 2016 by Schulte et al. [42], where an initial 850 fs long pulse was compressed down to 170 fs via a single-stage Herriott-type MPC with a transmission of about 90% at 10 MHz repetition rate. A total pulse energy of around 45  $\mu\text{J}$  was available after the MPC, corresponding to an average power of 375 W. The approach employed by the authors involved utilising the cell mirror substrates (fused silica) as the nonlinear material for SPM-based spectral broadening with each pass, achieved by applying an antireflection (AR) coating on the front side and a highly reflecting (HR) coating on the back of the mirror. By opting for a material thickness that remains below the self-focusing distance, this method facilitated the operation of the system at peak power levels that exceed the critical power threshold of the material, effectively leveraging the nonlinear optical properties without triggering detrimental self-focusing effects. In subsequent years, works have been published reporting post-compressed pulses ranging from 115 fs to 35 fs, in other words achieving a maximum compression ratio of 7.5, supporting repetition rates exceeding 10 MHz [43, 44], in which one or more fused silica plates were placed around the centre of the MPC. This methodology has shown to be also effective for pulse compression below 100 fs of thin-disk oscillators [54, 55]. Due to the low damage threshold nature of bulk material, pulse energy scaling has proven to be feasible in gas-filled MPCs, first studied numerically in 2017 by Hanna et al. [48], and later experimentally demonstrated by Lavenu et al., who achieved pulse compression from 250 fs down to 33 fs with an output pulse energy of 135  $\mu\text{J}$  at 7 bar argon [56]. Further pulse energy upscaling was successfully performed, for example, a 4f imaging geometry of the MPC was employed to compress an initial pulse energy of 2 mJ down to 37 fs at 500 mbar argon [57]. Additionally, larger compression factors were achieved [58, 59, 60], even exceeding factor 30 within an MPC filled with 600 mbar argon, supporting 18 mJ pulses [61].

In this case, 1.3 ps were successfully compressed down to 41 fs. In 2021, the same group was able to increase the pulse energy to 112 mJ in a roughly 8 m long cell filled with 250 mbar of argon [49]. A pulse duration of 37 fs with a compression factor of 35 was achieved, where a so-called donut mode of the beam was utilised for mode preservation of the beam, and to avoid exceeding the gas ionisation threshold. A few years later, Pfaff et al. demonstrated pulse energy upscaling to 150 mJ within an argon-based MPC, compressing the pulses down to 39 fs [50]. In both works, however, the compression of the pulses needed to be performed after attenuation of the pulse to prevent nonlinear effects arising in air. Moreover, average power scalability of gas-filled MPCs has been shown [62], even up to the kW regime [63].

All the previously mentioned works have utilised a single-stage multi-pass cell configuration. However, hybrid setups [64] as well as cascaded arrangements of MPCs [65] are also possible, especially when targeting pulse durations close to and in the few-cycle regime. First pulse durations reaching 13 fs were achieved by Balla et al. where a two-stage krypton-filled MPC setup, each 2 m long, was used for SPM-induced spectral broadening of 1.2 picosecond (ps) pulses [14]. This work (in which I also participated), however, suffered from high overall transmission losses originating from the metallic cell mirrors employed in the second stage to cover larger bandwidth. To improve the overall efficiency, Müller et al. exploited dielectrically enhanced metallic cavity mirrors in the second compression stage [66]. These mirrors are built on silicon substrates and are water-cooled, allowing the compression down to 6.9 fs with a pulse energy of about 780  $\mu$ J, corresponding to an overall transmission of more than 80 %. Energy scaling to around 7 mJ has been shown in a recent work, where in a cascaded arrangement of gas-based MPCs compression down to 9.6 fs has been achieved with an overall efficiency of 70 % [67]. In this particular case, the second compression stage utilised a dielectric chirped mirror pair as cell mirrors to cover the large bandwidth. Furthermore, repetition rate scalability in the MHz regime has been demonstrated [45, 68, 69] with sub-7 fs pulse post-compression at 10 mJ via supercontinuum generation in a second argon-filled MPC stage [70].

Other geometries to the more common Herriott-type configuration have also been proposed for energy scaling, such as convex-concave geometries [71], or bow tie configurations supporting 100 mJ pulse energies at large compression factors [72].

Multi-pass cells are not only limited to SPM, but they have also shown to

be suited for pulse self-compression of a 1550 nm pulse by exploiting soliton dynamics, which has been demonstrated in [46]. In this study, a single-stage MPC is operated in the net anomalous dispersion regime via an AR-coated silica plate placed close to one cavity mirror for dispersion tuning, resulting in a self-compressed pulse of 22 fs with 14  $\mu\text{J}$  of pulse energy at 125 kHz. Besides noble gases, molecular gases have also been used in MPCs for Raman-based frequency redshifting [47].

TABLE 3.1: Summary of experimentally achieved pulse post-compression results utilising various configurations of multi-pass cell compressors. The achievements are divided into single-stage MPC setups based on either solid-state material or gaseous medium, multi-stage MPCs as well as hybrid setups. The listed works are all seeded by Yb-based laser systems centred at 1030 nm wavelength.

	Ref.	$\tau_{in}$ [fs]	$\tau_{out}$ [fs]	$E_{out}$	Trans. [%]	$P_{avg}$ [W]	Rep. rate
<b>Single-stage Bulk MPC</b>	[42]	850	170	45 $\mu\text{J}$	88	375	10 MHz
	[43]	860	115	7.5 $\mu\text{J}$	90	300	40 MHz
	[44]	230	35	4.5 $\mu\text{J}$	88	84	18.5 MHz
	[54]	534	88	8.4 $\mu\text{J}$	88	112	13.4 MHz
	[55]	550	97	9.2 $\mu\text{J}$	91	123	13.3 MHz
	[73]	250	40	4 $\mu\text{J}$	90	100	18.4 MHz
<b>Single-stage Gas-based MPC</b>	[61]	1300	41	17.8 mJ	96	500	5 kHz
	[57]	210	37	1.9 mJ	93	186	100 kHz
	[56]	275	33	135 $\mu\text{J}$	85	20	150 kHz
	[58]	590	30	1.1 mJ	96	530	500 kHz
	[62]	675	70	8.3 mJ	85	836	100 kHz
	[63]	200	31	1 mJ	96	1000	100 kHz
	[59]	1100	60	0.8 mJ	80	100	100 kHz
	[49]	1300	37	108 mJ	91	500	5 kHz
	[60]	840	38	9.7 mJ	97	30	3 kHz
	[50]	461	39	150 mJ	96	780	5 kHz
<b>Hybrid setup /Cascaded MPC</b>	[68]	534	27	9.4 $\mu\text{J}$	80	98	13.4 MHz
	[45]	220	18	2.1 $\mu\text{J}$	60	100	28.3 MHz
	[64]	330	6.8	140 $\mu\text{J}$	61	21	150 kHz
	[65]	460	22	15.6 $\mu\text{J}$	76	40	200 kHz
	[14]	1200	13	2 mJ	20	200	100 kHz
	[66]	200	6.9	776 $\mu\text{J}$	82	388	500 kHz
	[69]	265	17	4.5 $\mu\text{J}$	60	1000	16 MHz
	[67]	1200	9.6	6.7 mJ	70	200	1 kHz
	[70]	230	6.9	10 mJ	84	12	1 MHz

### 3.4 Single-stage gas-based MPC

Having understood the basic concept behind the multi-pass cell post-compression technology, this section proceeds with a detailed description of the general implementation. In particular, experimental results of a conventional gas-filled MPC configuration are presented and discussed, and additionally compared to numerical simulations.

#### 3.4.1 Experimental setup

The overall experimental layout of the pulse compression setup is depicted in figure 3.3. It comprises a mode-matching lens telescope to match the beam's mode to the eigenmode of the cell, a single-stage gas-filled MPC placed inside a chamber and a dielectric chirped-mirror compressor. The following subchapters will provide a more detailed description of each part of the setup.

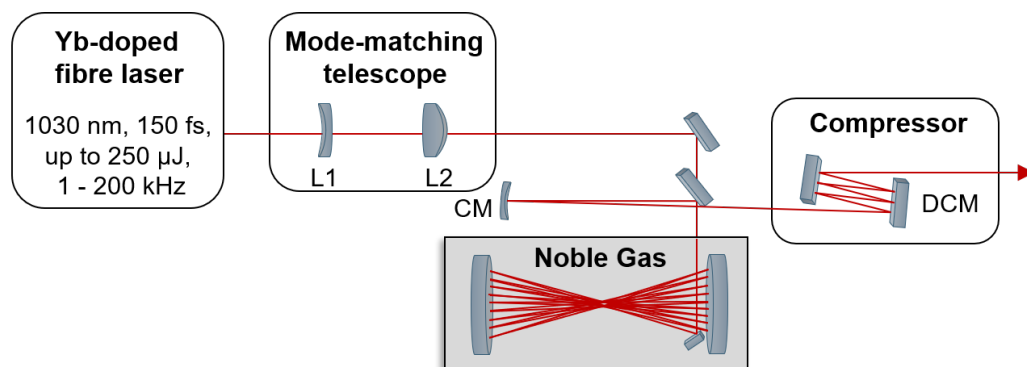


FIGURE 3.3: Schematic of the overall pulse compression setup composed of a mode-matching lens telescope (L1: concave lens and L2: convex lens), a gas-based single-stage conventional MPC, a spherical mirror (CM: concave mirror) for collimation and dispersion-compensating mirrors (DCMs) for post-compression.

#### Laser system

The setup is driven by a commercial diode-pumped ultrafast fibre amplifier system (Tangerine, Amplitude). It uses ytterbium-doped photonic crystal fibres as amplifying medium, as they can be diode-pumped and are able to amplify the pulses to energy levels exceeding 100 μJ. Additionally, high average power operation is possible due to reduced thermal effects provided by

the fibre geometry. Moreover, the laser system is characterised by a good output beam quality attributed to the guiding features of the single mode fibre. The laser unit is water cooled by a SMC HECR 008 autonomous chiller and is used for temperature regulation of the laser bench, the amplifier laser diode and opto-mechanical components inside the laser. The cooling unit requires regular maintenance to ensure the system operates within specifications.

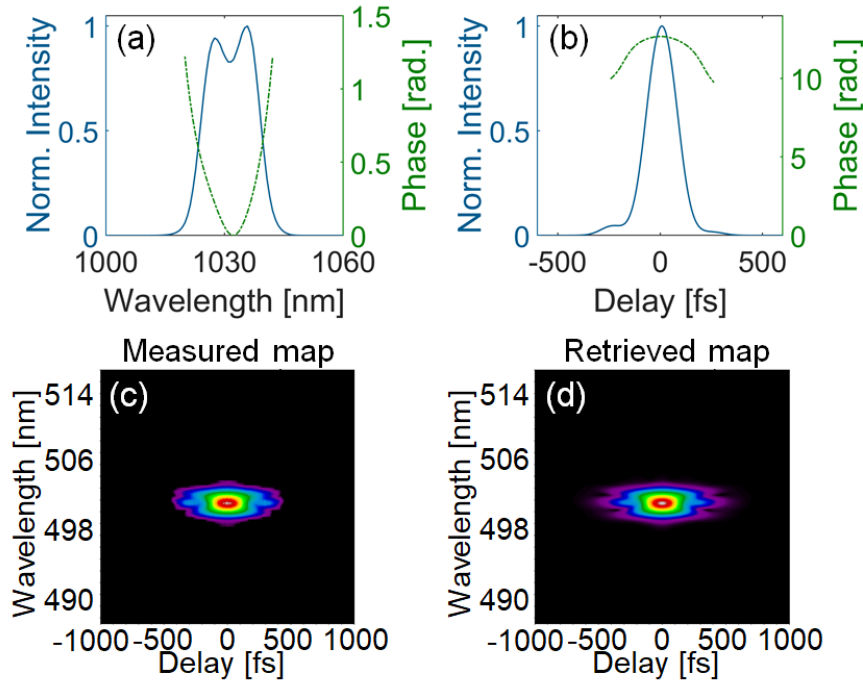


FIGURE 3.4: Characteristics of the laser pulse. (a) FROG retrieved spectrum (blue) and phase (dashed green). (b) FROG retrieved temporal profile (blue) and phase (dashed green). (c) Measured and (d) retrieved FROG trace.

Consequently, this laser system delivers up to  $250 \mu\text{J}$  pulse energy at a centre wavelength of 1030 nm, with the option of repetition rate tuneability from 1 kHz up to 200 kHz via integrated external modulator, corresponding to an average power of about 250 mW to 50 W, respectively. The pulse duration is characterised via a home-built second harmonic generation FROG (SH-FROG), retrieving in this case a pulse duration of about 170 fs at full-width half-maximum with a FROG error of approximately 0.09%. As can be seen in figure 3.4, the temporal pulse retrieval as well as the spectral retrieval exhibit a residual second-order chirp and slight third-order dispersion (TOD) at the leading edge of the pulse, which cannot be compensated for with the grating compressor incorporated in the laser module. Upon installation, the

caustic measurement of the laser system results in a beam quality factor of  $M_{x,y}^2 = 1.26 \times 1.23$ .

### MPC configuration

Initially, a spare rectangular vacuum chamber with a  $605 \times 275$  mm footprint was used for preliminary tests on the MPC. Two mirrors are placed in a Herriott-type configuration at a maximum distance of 400 mm from each other inside the chamber. In- and out-coupling of the beam is achieved via a small rectangular mirror with the dimensions  $5 \text{ mm} \times 25.4 \text{ mm}$  positioned in front of one of the cell mirrors, as can be seen in figure 3.5. To let the beam pass through the chamber, a viewport containing a 2-inch fused silica NIR antireflection (AR) coated window of 3 mm thickness is attached to the flange in front of the small rectangular mirror. The cell mirror M2 (as labelled in figure 3.5) is mounted on a manual linear stage to precisely adjust the number of round trips passing through the MPC. Moreover, millimeter precision is needed for the equidistant separation of the beam spots on the cell mirrors. On the other hand, cell mirror M1 (cf. figure 3.5) is clamped on a breadboard inside the chamber. Pumping and gas supply are achieved via two separate connectors, and a plexiglass cover allows for direct beam path observation inside the MPC.

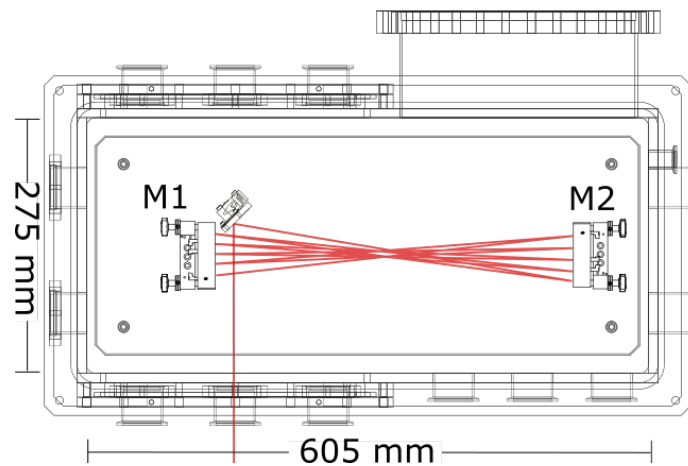


FIGURE 3.5: Herriott-type MPC configuration inside a vacuum chamber composed of two spherical cell mirrors M1 and M2, and a small rectangular in-/out-coupling mirror in front of mirror M1. The dimensions of the chamber are included in the figure.

The chamber is designed to support vacuum levels in the order of  $10^{-5}$  mbar, hence, setting a limit on the maximum achievable overpressure value usable

for the MPC compressor. Furthermore, the excessively large volume of the chamber amounting to approx. 80 L makes the setup rather costly, due to the substantial amount of gas needed to fill the chamber. Consequently, a more compact overpressure chamber tailored to the high gas pressures needed for specific MPC configurations has been designed and will be introduced in the subsequent chapter.

### Compressor

As the pulses do not undergo self-compression while travelling through the MPC, but rather experience a temporal pulse broadening imposed by the gas dispersion, broadband dispersion-compensating mirrors (DCMs) are utilised for pulse post-compression.

Two different coatings are used due to their availability at the time of the measurements. In the case of the conventional MPC setup, two DCMs are used, each introducing about  $-200 \text{ fs}^2$  of GDD over a bandwidth range of 990 - 1090 nm (cf. figure 3.6).

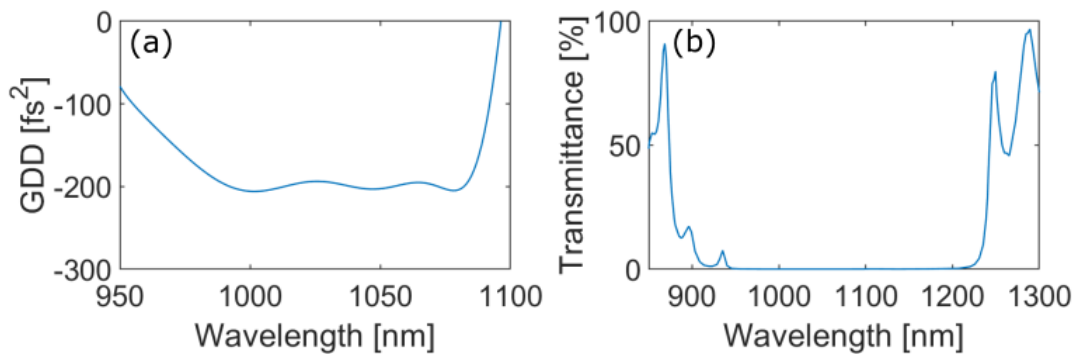


FIGURE 3.6: Specifications of the dielectric compressor mirrors for  $\text{AOI} = 5^\circ$ , depicting (a) the group delay dispersion and (b) transmittance of the mirror.

A broadband DCM pair is used in combination with the dispersion-engineered MPC configuration, which will be introduced and explained in chapter 4 in more detail, to support the compression of larger spectral bandwidths. The average GDD value given by one reflection on each mirror pair results in an oscillatory value around  $-100 \text{ fs}^2$  over a spectral range of 790 - 1400 nm (cf. figure 3.7).

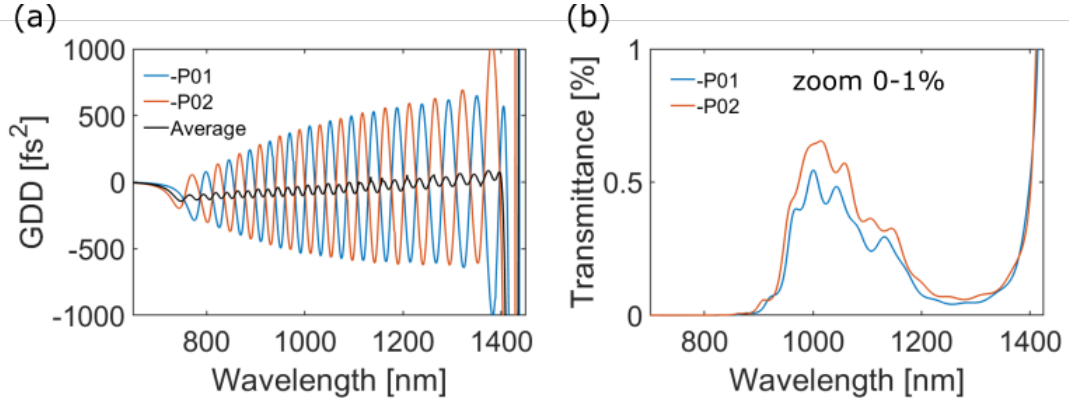


FIGURE 3.7: Specifications of the broadband DCM pair for AOI = 5°. (a) depicts the group delay dispersion of the two mirror coatings P01 and P02 (blue and red, respectively) and their average (black), and (b) shows their transmittance zoomed in from 0 to 1%.

### 3.4.2 Conventional MPC

The conventional MPC comprises two 2-inch plano-concave standard quarter-wave stack multi-layer mirrors with a radius of curvature (ROC) = 200 mm placed at a distance  $L \approx 379.9$  mm from each other, which results in an L/R ratio of about 1.90. Based on the equations mentioned previously in 3.2.1, the cell parameters have been calculated as follows

- focal beam waist:  $w_0 = 119.7 \mu\text{m}$
- beam radius at the mirror:  $w_M = 1.1 \text{ mm}$
- fluence on the mirror:  $F_M = 55.8 \frac{\text{mJ}}{\text{cm}^2}$
- B-integral per round trip:  $B \approx 3.6,$

indicating a fluence on the cell mirrors below the LIDT value of the designed mirror coating. For dielectric mirrors this value typically amounts to  $0.1 - 0.4 \frac{\text{J}}{\text{cm}^2}$ . Since from a technical and engineering point of view the coating of the cell mirrors is directly correlated to the producible spectral width, it is worthwhile mentioning its specifications, having in the present configuration a defined GDD value within the area  $\pm 10 \text{ fs}^2$  over a spectral bandwidth ranging from 990 – 1090 nm with at least 99.5% reflectivity within the specified spectral region, as can be seen in figure 3.8. For simplicity, the cell mirror with this specific coating will be referred to as low-GDD mirror throughout the thesis.

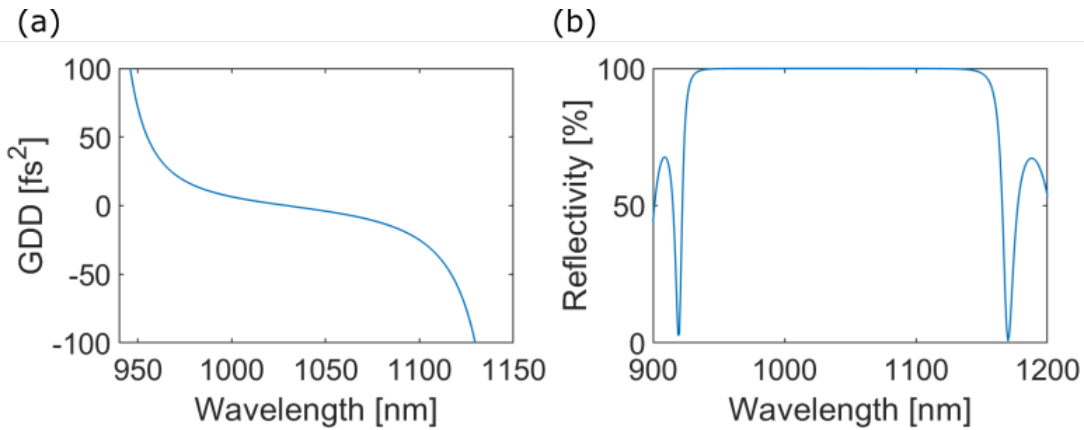


FIGURE 3.8: Coating specifications of the standard quarter-wave stack multi-layer mirrors used in the conventional multi-pass cell configuration showing (a) the group delay dispersion curve and (b) reflectivity.

Due to the vacuum compatibility of the chamber, different operation regimes of this specific MPC configuration have been explored, i.e. the pressure range it can be operated at. In order to avoid the use of excessively high gas pressures, the noble gas krypton has been chosen to drive the nonlinear process inside the MPC, as it has a rather high nonlinearity. Note that the laser is operated at 1 kHz repetition rate (250 mW average power) throughout this chapter. The evolution of the SPM-based spectral broadening process is depicted in figure 3.9 (a) for 22 round trips through the MPC within a pressure range from 0.6 bar to 1.6 bar. As can be seen, a maximum bandwidth of 140 nm tail-to-tail is generated at gas pressures of at least 1.4 bar, however, with a lower transmission efficiency at 1.5 bar and 1.6 bar. This might be related to the rather narrow bandwidth of the low-GDD cell mirrors, preventing the formation of even broader spectra. In addition, a further limitation is clearly set by the chamber, since it can withstand a maximum gas pressure of 1.6 bar. Exceeding this gas pressure results in a strong leakage located at the plexi-glass lid.

To circumvent the restraints imposed by the chamber and test if the major limiting factor related to the spectral broadening can be allocated to the cell mirror coating, further tests exploiting the higher nonlinearity of xenon gas were performed. For the same MPC configuration, the broadening of the spectral bandwidth with increasing gas pressure in the range from 0.1 to 0.6 bar is shown in figure 3.9 (b). A maximum bandwidth of 140 nm tail-to-tail is generated at 0.6 bar, which matches exactly the spectrum at 1.4 bar krypton.

TABLE 3.2: Spectral bandwidth values tail-to-tail of the conventional MPC configuration generated in krypton (left) and xenon (right) at different gas pressures.

Pressure Kr	Spectral bandwidth Kr	Pressure Xe	Spectral bandwidth Xe
0.6 bar	96 nm	0.1 bar	83 nm
0.8 bar	110 nm	0.2 bar	97 nm
1 bar	117 nm	0.3 bar	109 nm
1.2 bar	120 nm	0.4 bar	118 nm
1.4 bar	140 nm	0.5 bar	126 nm
1.5 bar	140 nm	0.6 bar	140 nm
1.6 bar	140 nm		

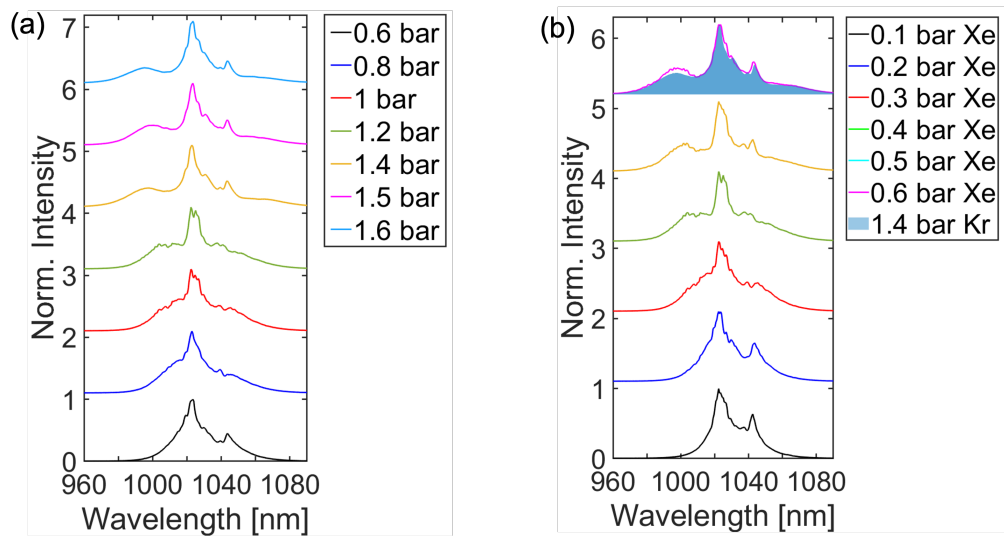


FIGURE 3.9: Spectral broadening evolution of the conventional MPC achieved for two types of noble gases at 1 kHz (250mW average power). MPC output spectra measured at different gas pressures in (a) krypton and (b) xenon.

While further increasing the gas pressure the total transmission efficiency dropped rapidly and no further broadening was possible. Moreover, since the ionisation potential of xenon is significantly lower than krypton, using excessively high gas pressures of pure xenon can cause plasma generation inside the MPC, which should be avoided.

Comparing the performances between the argon filled MPC and xenon filled one, it is evident that overall the nonlinear spectral broadening process is certainly limited by the design specifications of the low-GDD cell mirrors, meaning that the nonlinear phase-shift is "controlled" by the flat phase in the specified range of the coating design.

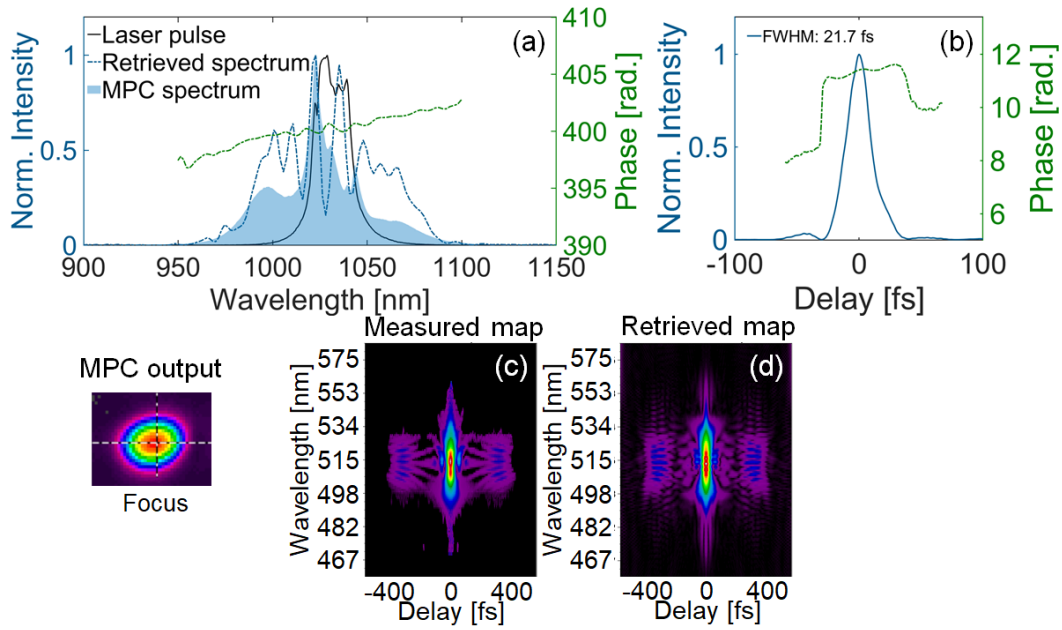


FIGURE 3.10: Output pulse characteristics of the conventional MPC configuration at 1 kHz (250 mW average power) with image of the focused beam at the output of the MPC. (a) Spectral comparison between laser pulse (black), MPC configuration with low-GDD cell mirrors (blue-filled) and its FROG retrieved spectrum (dashed blue) and phase (dashed green). (b) FROG retrieved temporal profile (blue) and phase (dashed green). (c) Measured and (d) retrieved FROG trace.

After having determined the optimal operation regime of this MPC configuration, its pulse characterisation at 1.4 bar krypton gas has been performed. The AvaSpec-2048XL spectrometer by Avantes is used to detect the generated spectrum, reaching a bandwidth of about 140 nm tail-to-tail, as shown before, with a transform limit of approximately 22 fs at FWHM (cf. figure 3.8). The spectrometer grating covers the spectral range within 200 nm to 1160 nm, however, with a lower responsivity at the limits, resulting in a depleted/flattened spectral shape on the red side of the MPC output spectrum. The transmission efficiency of this MPC configuration is measured to be 86% at its output. This rather low transmission, with respect to the characteristic transmission of MPCs exceeding 90%, could be attributed to a minor clipping of the propagating beam inside the cell. As mentioned already, pulse compression is achieved via two DCMs (cf. figure 3.6) to compensate for roughly  $1850 \text{ fs}^2$  of positive GDD acquired during the nonlinear

process and additional uncoated 8 mm fused silica glass. The characterisation of the generated pulses is performed by means of a home-built second-harmonic frequency-resolved optical gating (SH-FROG) setup, for which a  $100\ \mu\text{m}$  thick BBO crystal has been utilised. The measurement is done on a grid of  $512 \times 512$  points, retrieving in this case a pulse duration of 21.7 fs (FWHM) with a FROG error of approximately 0.4%, which corresponds to a compression factor of 6.9 (cf. figure 3.10).

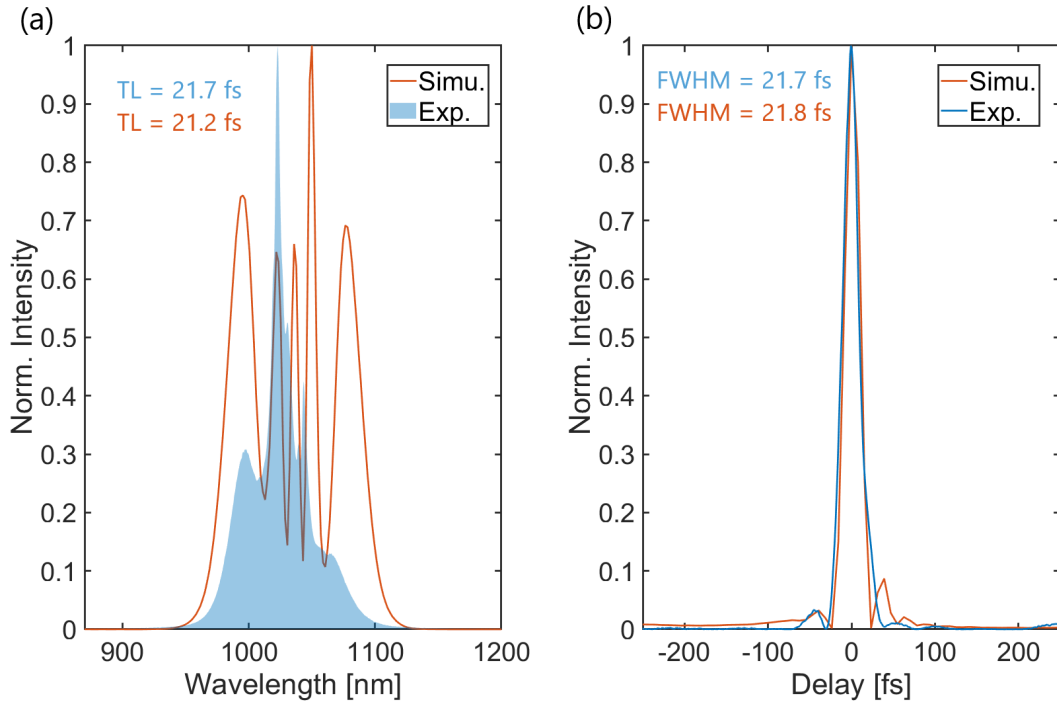


FIGURE 3.11: Comparison between 3D-simulation and experimental output of the conventional MPC. (a) Simulated (orange) and measured (blue-filled) output spectrum of the MPC with corresponding calculated transform limit values (FWHM). (b) Simulated (orange) and measured (blue) temporal profile after compression. The effective pulse duration at FWHM of each is mentioned in the figure.

The experimentally obtained data is supported by numerical simulations based on the 3D model described already before, which were performed in collaboration with Esmerando Escoto from the FS-LA group at DESY, as mentioned previously. Since the effectiveness of SPM-based spectral broadening relies heavily on the shape of the input pulse, the pulse used in the simulations is modeled after the laser system utilised in the experiment (cf. figure

3.4). Note that a Gaussian beam is considered in this case, as major spatio-spectral effects are not expected to occur in MPCs. In order to keep the simulations as close as possible to the real experimental scenario, the cell mirror coating is incorporated in the numerical model. Hence, an unchirped input pulse duration of 150 fs at 250  $\mu$ J is considered. The simulations predict a transform limited pulse duration of 21.1 fs at FWHM (cf. figure 3.11 (a)), which matches the transform limit calculated from the experimental spectrum. A discrepancy between the simulated and measured spectrum is noticeable especially on the red side, which is related to the spectrometer responsivity, as mentioned before. Furthermore, the temporal profile of the compressed pulse from simulations agrees very well with the FROG retrieved one with a pulse duration of 21.8 fs (FWHM), as can be seen from figure 3.11 (b). Note that to perform pulse compression numerically, the sum of the total second-order dispersion (GDD) from both cell mirrors and gas has been compensated for.

## 3.5 Conclusion

In this chapter, a conventional Herriott-type multi-pass cell compressor has been introduced and tested. Fundamental parameters, which are essential to optical cavities, were determined for the construction of a compact, roughly 400 mm long, single-stage MPC based on nonlinear spectral broadening in gaseous media, specifically noble gases. By means of standard dielectric low-GDD cavity mirrors, pulse post-compression down to approximately 22 fs pulse duration has been achieved at 1 kHz repetition rate (about 250 mW average power), characterised by an MPC throughput exceeding 90%. These results are additionally supported by simulations based on a 3D propagation model. This configuration, however, is limited on the one hand by the employed chamber, which is designed for operations in the (low) vacuum regime. On the other hand, the coating design of the cavity mirrors is restricting spectral bandwidth gain. Hence, for targeting shorter pulse durations, ranging from sub-20 fs all the way down to the few-cycle regime, modifications to the chamber as well as the cell mirror coatings are essential.



## Chapter 4

# Dispersion control in MPC

In the previous chapter, spectral broadening limitations of a conventional single-stage gas-based multi-pass cell configuration have been shown and explained. A route to overcome these limitations is the use of negatively chirped dielectric cavity mirrors for direct dispersion control within the MPC compressor to optimise the spectral broadening process while applying high-pressure gases.

This chapter starts by introducing the general concept of dispersion management based on the parameters dispersion length and nonlinear length, followed by numerical predictions and experimental achievements showing sub-20 fs pulse compression as well as average power scalability. Lastly, improvements for future work on this setup will be briefly addressed.

### 4.1 Principle of dispersion management

Effectively controlling the dispersion and nonlinearity is essential for overcoming inherent restrictions associated with spectral broadening, including decreases in peak power, self-steepening, and temporal pulse breakup. In this regard, the two parameters dispersion length  $L_D$  and the nonlinear length  $L_{NL}$  can be formulated as follows

$$L_D = \frac{T_0^2}{|k_2|} \quad (4.1)$$

$$L_{NL} = \frac{1}{\gamma P_0} \quad (4.2)$$

where  $T_0$  symbolises the input pulse duration,  $P_0$  describes the incident peak power and  $\gamma = n_2\omega_0/cA_{\text{eff}}$  is the nonlinear coefficient [74]. Latter is dependent on the effective area  $A_{\text{eff}} = \pi w^2$  of a Gaussian beam with radius  $w$ .

The ratio  $L_D/L_{NL}$  dictates the regime of spectral broadening. When this ratio is much greater than 1, i.e.  $L_D/L_{NL} \gg 1$ , a rapid temporal expansion of the laser pulse takes place, eventually leading to a saturation of the spectral broadening effect. On the other hand, when the ratio is much smaller than 1, i.e.  $L_D/L_{NL} \ll 1$ , a dispersion-balanced / dispersion-free regime is reached. Here, SPM is the prevalent phenomenon, leading to the efficient generation of additional spectral components with only minor repercussions on the temporal profile of the pulse.

Dispersion control has been explored through various methods, such as gas pressure gradients within bandgap hollow-core photonic crystal fibres (HC-PCFs) [75, 76] and the use of Kagomé-type structured fibres. Although spectral bandwidths corresponding to sub-10 fs pulse durations were achieved, these methods are often restricted by high energy losses during transmission and typically operate at rather moderate pulse energies [77, 78]. Furthermore, achieving dispersion-balanced regimes with fibre-based spectral broadening methods becomes challenging when aiming for significant compression factors and wide bandwidths. In this context, multi-pass cells present a viable solution, facilitating dispersion control and thereby enabling SPM-dominated spectral broadening across extensive parameter ranges.

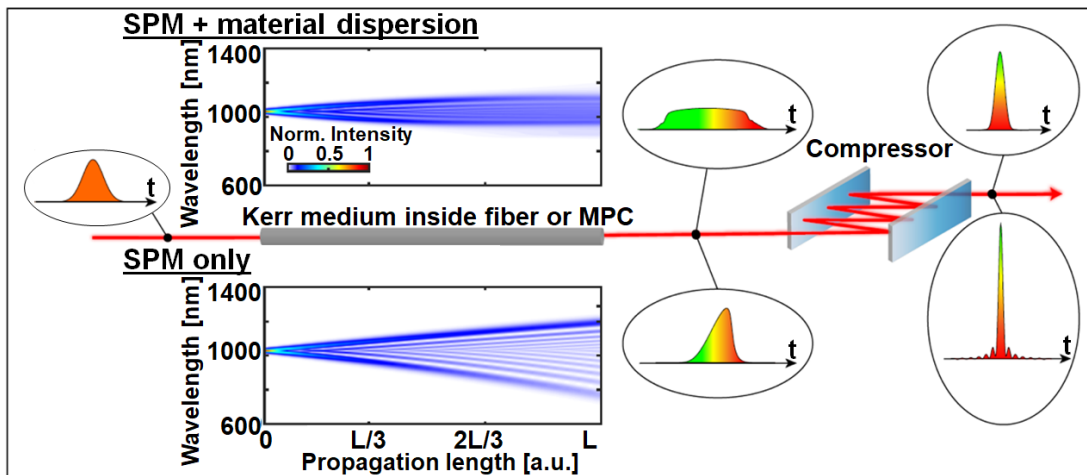


FIGURE 4.1: SPM-based spectral broadening in a normal dispersive medium (top) and a dispersion-balanced scheme (bottom): Simulated SPM-based spectral evolution over Kerr medium length  $L$  and corresponding temporal pulse intensity profile before and after compression. In both cases, the simulations were performed considering an input pulse duration of 150 fs.

The impact of precise dispersion management on the nonlinear broadening process can be easily demonstrated numerically, for which two different scenarios are compared. In each case, the analysis begins with a Gaussian-shaped pulse characterised by a 150 fs duration in the infrared range at a centre wavelength of 1030 nm. In the first case, where the pulse propagates through a conventional waveguide, such as an MPC filled with a nonlinear (Kerr) medium, the broadening process becomes saturated quite rapidly, due to the decrease in peak power as the pulse propagates further through the medium, and leads to significant temporal pulse reshaping (cf. figure 4.1, top). Conversely, in the second scenario involving an ideally fully dispersion-balanced waveguide, spectral broadening induced by self-phase modulation expands over a wider spectral bandwidth as the peak power in this case is kept relatively constant during propagation through the medium, and temporal pulse reshaping is minimal (cf. figure 4.1, bottom). This facilitates the generation of temporally shorter pulses and increases peak intensities, although the resulting temporal profile shows characteristic pre- and post-pulses of unperturbed SPM [79]. It is worth highlighting that, as previous studies have indicated, the temporal profile of the pulse may appear sharper in conventional non-dispersion-balanced techniques [80].

The approach of embedding negatively chirped dielectric cell mirrors inside multi-pass cells is not entirely new, as it has been applied in relation to solid-state materials, demonstrating self-compression by exploiting the anomalous dispersion regime [81]. Most commonly, in bulk-based methods the peak intensity of the pulse is restricted by damage to the antireflection coatings or the risk of exceeding the LIDT value of the nonlinear material. By moving to a gaseous medium, these constraints can be bypassed, allowing for more effective dispersion management and optimisation of the spectral broadening process, even under high-pressure conditions. In the following, experimental achievements based on the dispersion control principle are presented and explained. Moreover, due to the constraints dictated by the vacuum chamber used so far for implementing the MPC, a new chamber design supporting overpressures will be introduced.

## 4.2 Scaling of post-compressed pulse duration

The overall experimental layout of the pulse compression setup is almost identical to the previous layout (cf. chapter 3, figure 3.3), i.e., it comprises a mode-matching lens telescope, a single-stage gas-based MPC and a mirror compressor. The primary difference lies with the MPC setup itself, since in this case the linear dispersion arising from the propagation through the nonlinear medium is compensated for by introducing dispersion on the cell mirrors. The experimental implementation is quite straightforward as a simple exchange of the previously used low-GDD standard quarter-wave stack multi-layer mirrors with dispersive dielectric mirrors is sufficient. This work, in particular, distinguishes between two dispersion-engineered MPC configurations, here labelled as setup 1 and setup 2 (cf. figure 4.2). The green colour coding inside the MPC indicates the added dispersion on the cell mirror.

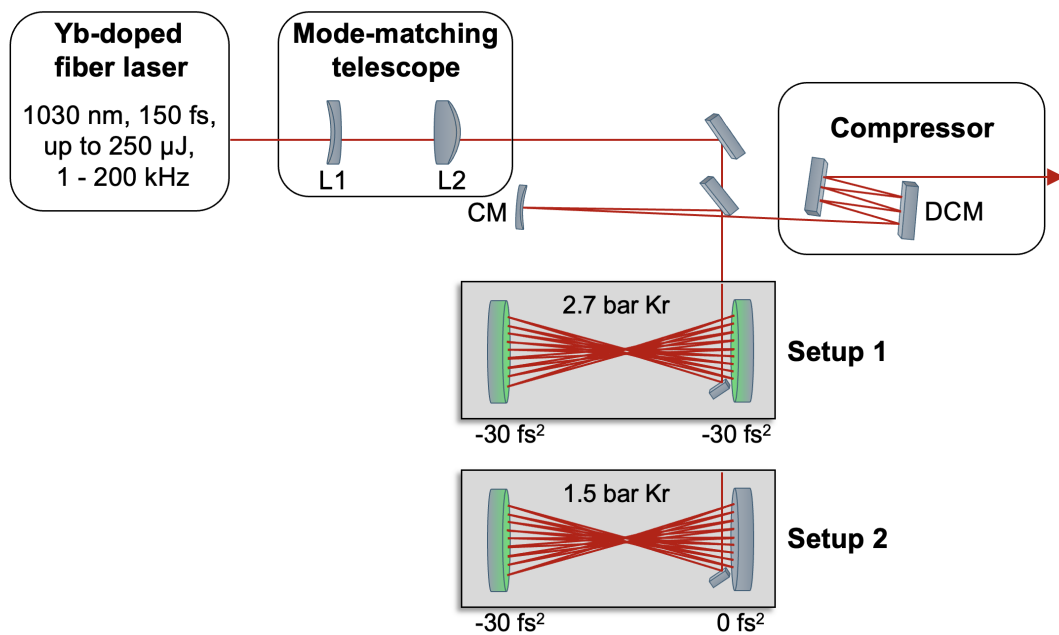


FIGURE 4.2: Modified schematic of the overall pulse compression setup composed of a mode-matching lens telescope (L1: concave lens and L2: convex lens), a gas-based single-stage MPC, a spherical mirror (CM: concave mirror) for collimation and dispersion-compensating mirror pair (DCM) for post-compression. Two MPC configurations are introduced: a dispersion-engineered MPC comprising two dispersive cell mirrors (setup 1), and a dispersion-optimised MPC consisting of one dispersive and one low-GDD cell mirror (setup 2). The green colour coding in each MPC setup symbolises the dispersive cell mirror.

In order to get a quantitative assessment of dispersion management in multi-pass cell compressors, numerical simulations based on the 3D propagation model, introduced in the previous chapter, are performed to investigate different dispersion-engineered configurations. In this context, experimental input parameters outlined in this work are employed to ensure that the simulations closely mirror the conditions in the laboratory. As mentioned already in the previous chapter, the input pulse shape has a strong impact on SPM-based spectral broadening. Therefore, the input pulse employed in these simulations possesses identical characteristics to the one used in the conventional MPC simulation discussed in chapter 3.4.2. The first configuration (figure 4.2, setup 1), introduces  $-30 \text{ fs}^2$  of group delay dispersion per cell mirror bounce and supports pulse energies up to  $122 \mu\text{J}$ . The corresponding numerical simulations suggest that the spectral bandwidth is notably wider compared to that of a conventional MPC, resulting in a TL of 11.8 fs (cf. figure 4.3 (a)) with a compressed pulse duration of 12.2 fs at FWHM (cf. figure 4.3 (c)). Note that pulse compression is performed numerically via the same method applied in chapter 3.4.2. Closely tuning the dispersion by employing only a single dispersive cell mirror (figure 4.2, setup 2) allows to utilise the entire  $250 \mu\text{J}$  of pulse energy provided by the laser system itself. In this case, the simulation yields a transform-limited pulse duration of 13.3 fs with a numerically compressed pulse of 16.4 fs at FWHM (cf. figure 4.3 (b) and (d), respectively). By simply adjusting the pressure of the gas, simulations for both setups were conducted to optimise spectral broadening within an experimentally manageable range, while also ensuring minimal losses in transmission.

In contrast to the conventional MPC configuration which is operated in an overall normal dispersion regime (i.e. overall positive dispersion), setup 1 is run in a slightly overall anomalous dispersion regime (i.e. overall negative dispersion), supporting a dispersion-balanced scenario. As a result, the overall dispersion regime is influenced by both the gas density and the mirror coating. Modifying these parameters allows for the adjustment of pulse energy while preserving similar spectral broadening properties. However, such parameter adjustments are often restricted by limitations in the experimental setup and ionisation thresholds, particularly in setup 1, where self-compression may lead to ionisation, thereby imposing constraints on the maximum pulse energy. Note that, in this case, the simulations were performed by taking into account the cell mirror specifications mentioned in figure 3.8 and 4.5.

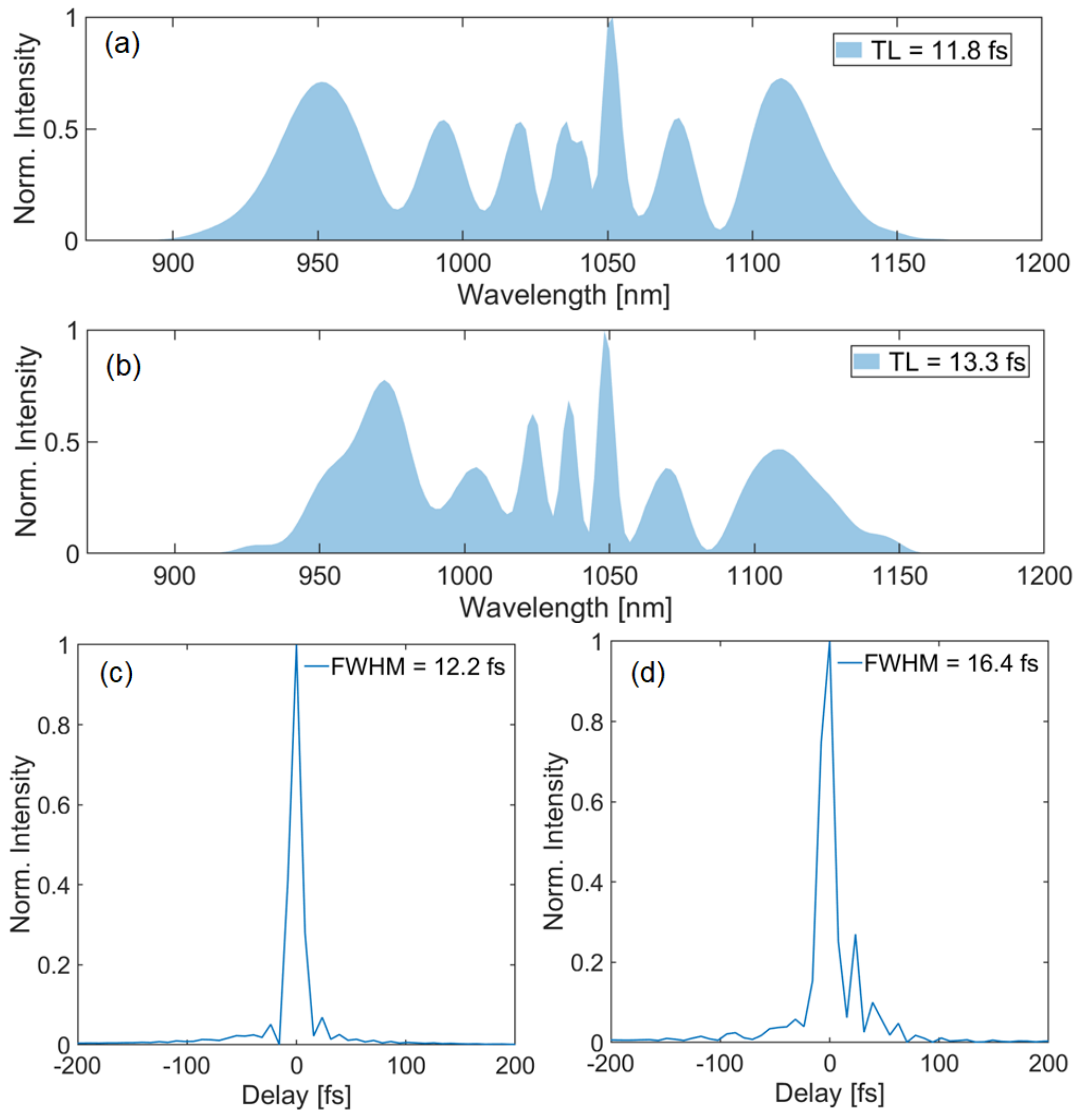


FIGURE 4.3: Numerical simulations based on the 3D model for two different dispersion-balanced MPC configurations. (a) Simulated spectrum of the dispersion-engineered MPC containing two  $-30 \text{ fs}^2$  cell mirrors. (b) Simulated spectrum of the dispersion-optimised MPC configuration with one dispersive and one low-GDD cell mirror. (c) and (d) are the simulated temporal profiles after compression of the respective MPC configurations.

### 4.2.1 Overpressure chamber

The spectral broadening stage is composed of a compact (500 mm length) overpressure chamber which has been designed in collaboration with the FS-LA group at DESY, Hamburg. A cage assembly incorporating two concave mirrors facing each other is utilised to create the Herriott-type MPC. Here as well, a small rectangular dielectric mirror with the dimensions 4 - 5 mm

(depending on the accuracy of the cutting of the mirror)  $\times 25.4$  mm is placed in front of one of the large mirrors to achieve in- and out-coupling of the beam. The cage assembly is screwed on a 160 mm diameter flange, which is then fixed with an L-shaped clamp directly on the optical table. Latter clamp is needed to give additional stabilisation to the cage assembly upon closing the chamber. A metallic cylindrical cover is slid onto the cage assembly to air-tighten the compression chamber, supporting pressures up to 3 bar absolute. To facilitate the sliding of the cover a rail system is placed underneath the cylinder. Once the chamber is closed and filled with gas, the beam passes in and out of the MPC via a viewport containing a 1-inch diameter and 3 mm thick broadband AR coated UV-FS window. A visual description of the chamber configuration is given in figure 4.4.

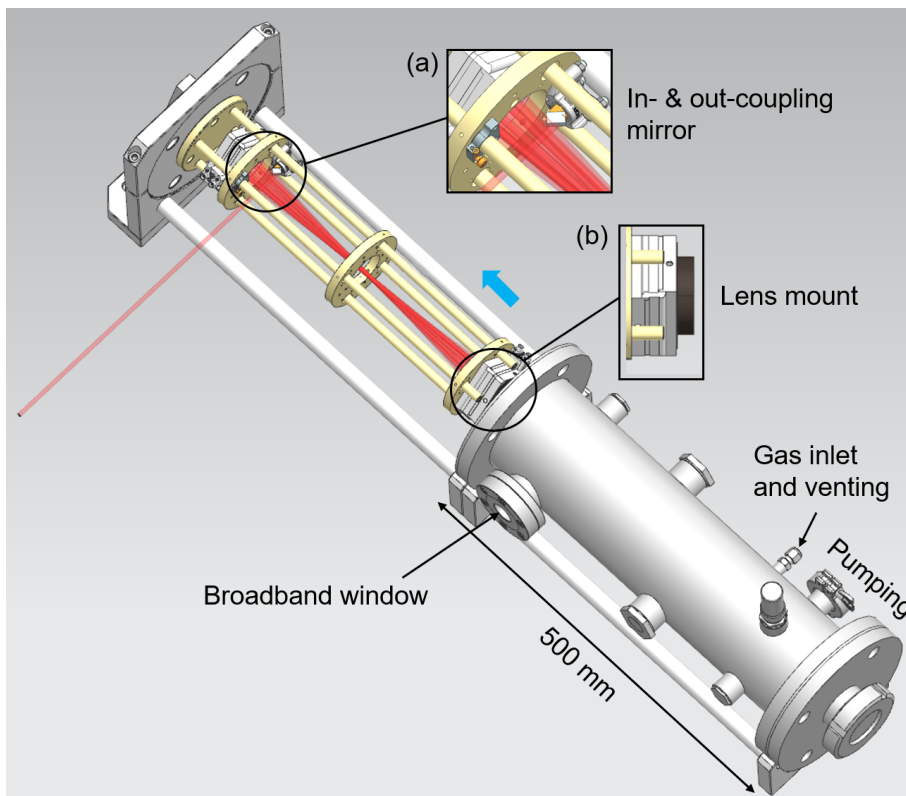


FIGURE 4.4: Technical drawing of the compact overpressure chamber showing the cage assembly (yellow) which forms the MPC, the metallic cylindrical cover and clamping system to fix the chamber to the optical table. The blue arrow indicates the sliding direction of the metallic cover to air-tighten the chamber. Inset (a) is a zoom-in on the in- and out-coupling mirror mount, whereas inset (b) shows the mounting of a 2-inch lens behind one of the cavity mirrors for observing the pattern with closed chamber.

In order to observe possible misalignments inside the chamber as well as mode mismatches, the leakage of the Herriott-pattern through one of the cavity mirrors is projected onto a beam block outside the chamber. For this purpose, a 2-inch focusing lens is screwed behind one of the cavity mirrors and a 2-inch window incorporated into a 160 mm diameter flange. Gas supply and pumping of the air/gas are achieved via two distinct connectors, as highlighted in figure 4.4. Due to its availability at the time of the measurements, an Ecodry 40 plus pump by Leybold is used to evacuate the chamber, but a conventional scroll pump would also be sufficient since high vacuum levels are not needed.

### 4.2.2 Dispersion-engineered MPC

Based on the predictions from the numerical simulations discussed before, experimental tests were performed to assess the feasibility of the dispersion-management concept in MPCs. The overall experimental layout has already been introduced and depicted in figure 4.2. In this particular case, two lenses with focal lengths of -150 mm and 250 mm, respectively, are used to match the laser beam to the eigenmode of the cell. For fine adjustments, they are each mounted on a manual linear stage.

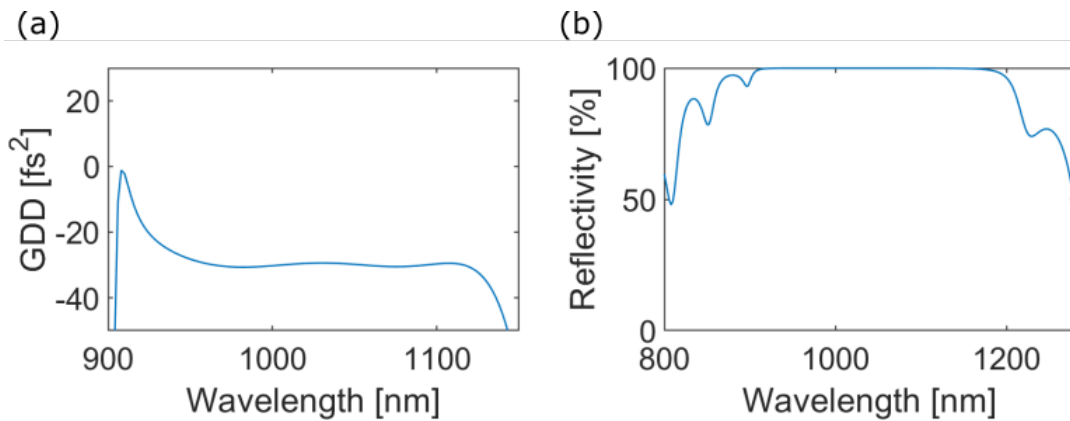


FIGURE 4.5: Custom coating design of the dispersive mirrors showing (a) the group delay dispersion curve and (b) reflectivity. These are used as cavity mirrors in the dispersion-engineered multi-pass cell setups.

To achieve nonlinear spectral broadening inside the MPC, we first consider the configuration labelled as setup 1 in figure 4.2, operated at 1 kHz repetition rate. It incorporates two 2-inch plano-concave mirrors with a ROC = 200 mm, which are placed at a distance  $L \approx 396$  mm from each other.

Hence, the L/R ratio amounts to 1.98. These cell mirrors are custom-coated and introduce a GDD of about  $-30 \text{ fs}^2$  each over a spectral bandwidth extending from approximately 950 – 1120 nm with at least 99.5% reflectivity within the specified spectral region, as can be seen in figure 4.5. Moreover, they correct for the linear dispersion accumulated during a single propagation through the cell filled with 2.7 bar krypton, considering 15 round trips through the MPC. Based on the equations mentioned previously in 3.2.1, the focal beam waist and beam radius on the mirror have been calculated to be  $w_0 = 80.8 \mu\text{m}$  and  $w_M = 1.6 \text{ mm}$ , respectively, resulting in a peak fluence on the mirror of roughly  $F_M = 24.4 \frac{\text{mJ}}{\text{cm}^2}$ , which is below the LIDT value of these mirrors. After passing through the MPC, the beam is recollimated by one plano-concave broadband dielectric mirror with ROC = 1500 mm and redirected to the compressor. Two distinct spectrometers, Ocean FX and NirQuest by Ocean Insight Inc., are utilised to fully detect the generated spectral range of the MPC output spectrum. As depicted in figure 4.6 (a) (blue-filled curve), a bandwidth of approximately 130 nm at FWHM (ca. 220 nm tail-to-tail) is produced which corresponds to a transform limit of about 12 fs at FWHM. These findings align very well with the forecasts provided by the 3D simulations discussed earlier and illustrated in figure 4.3. Compared to the results obtained with the conventional configuration, significant additional spectral broadening can be achieved via dispersion control inside the MPC (cf. chapter 3), whereby the overall throughput is maintained high and measured to reach 98% directly at the output of setup 1 (dispersion-engineered MPC configuration). The pulses are temporally compressed by employing a broadband DCM pair (cf. chapter 3, figure 3.7) to compensate for roughly  $800 \text{ fs}^2$  of GDD acquired during propagation through the MPC.

The SH-FROG measurement performed for the characterisation of the pulse retrieves a pulse duration of 16.4 fs (FWHM) with a FROG error of roughly 0.2%, corresponding to a compression factor of 9.1, as shown in figure 4.6 (b). This measurement is carried out for a  $100 \mu\text{m}$  thick BBO crystal on a grid of  $512 \times 512$  points. The experimentally recorded and numerically reconstructed FROG traces (figure 4.6 (c) and (d), respectively), as well as the retrieved pulse duration (figure 4.6 (b)), show residual third-order dispersion. This most likely stems from the DCM pair coating used for post-compression of the pulses, which is not designed to fully compensate for the generated spectral phase. Moreover, discrepancies between the FROG retrieved and the experimentally measured spectra are attributed to the narrow

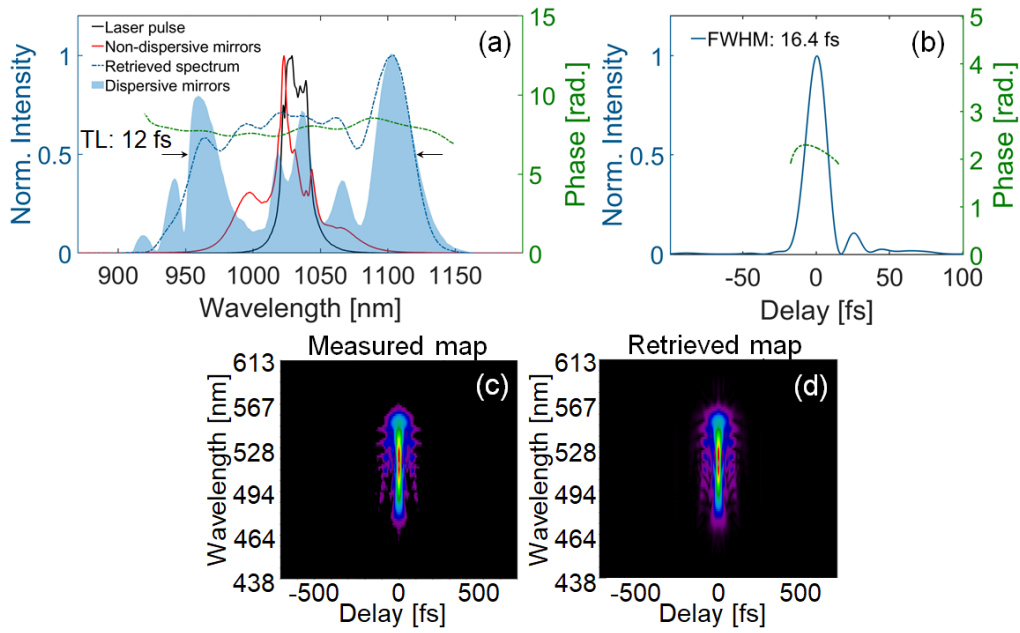


FIGURE 4.6: Output pulse characteristics of the dispersion-engineered MPC (setup 1) at 1 kHz repetition rate for 122  $\mu\text{J}$  input pulse energy. (a) Spectral comparison between the laser pulse (black), conventional cell configuration (red), MPC configuration containing two dispersive cell mirrors (blue-filled) and the corresponding FROG-retrieved spectrum (dashed blue) and phase (dashed green). (b) FROG-retrieved temporal profile (blue) and phase (dashed green). (c) Measured and (d) retrieved FROG trace.

dynamic range of the SH-FROG measurements. Therefore, latter puts constraints on the precise retrieval of potential temporal artifacts with spectral components near the centre wavelength. Additionally, the generated MPC output spectrum exhibits a noticeable asymmetry on the blue side, indicating that the coating of the cell mirror is restricting the extent of possible spectral broadening.

Contrary to the conventional MPC setup, which can be operated at maximum laser pulse energy of 250  $\mu\text{J}$ , the dispersion-engineered configuration presented here can only support 122  $\mu\text{J}$ , which is half of the pulse energy. The fundamental restriction stems from the incorporated dispersive cell mirrors, as they overcompensate for the phase, consequently increases the intensity and leads to ionisation. However, a straightforward approach to address this issue is to effectively balance the negative dispersion of the cell mirrors with the accumulated positive dispersion during propagation through the non-linear medium. This is easily implemented experimentally as replacing one

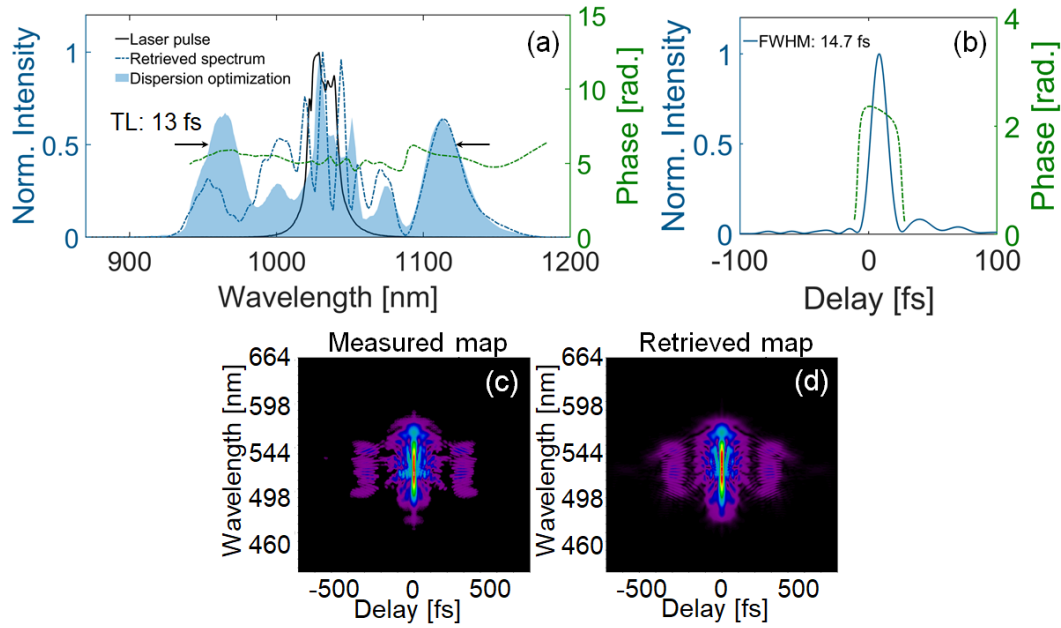


FIGURE 4.7: Output pulse characteristics of the dispersion-optimised MPC (setup 2) at 1 kHz repetition rate for  $250 \mu\text{J}$  input energy. (a) Spectral comparison between the laser pulse (black), the MPC configuration with one dispersive and one low-GDD cell mirror (blue-filled) and its FROG-retrieved spectrum (dashed blue) and phase (dashed green). (b) FROG-retrieved temporal profile (blue) and phase (dashed green). (c) Measured and (d) retrieved FROG trace.

dispersive cell mirror with a low-GDD one, and adjusting the gas dispersion by reducing its pressure to 1.5 bar is sufficient (cf. figure 4.2), which corresponds to an almost fully dispersion-balanced scenario. For the same number of round trips (in total 15) and utilising the entire pulse energy of the laser system as input, the bandwidth of the generated spectrum is clearly being preserved in this configuration and corresponds to a transform-limited pulse of about 13 fs (FWHM), as can be seen in figure 4.7 (a) from the blue-filled curve. This result also aligns well with the predictions from the 3D simulations presented in figure 4.3. Furthermore, the overall throughput measured directly at the output of the MPC exceeds 90%, demonstrating that the overall efficiency is not degraded but kept high. In this case, pulse post-compression is achieved by compensating for roughly  $600 \text{ fs}^2$  of total GDD using a broadband DCM pair, which has been used previously. It should be noted that these mirrors introduce additional pulse energy losses of approximately 8%. The FROG measurement is performed exactly as for the previous setup, retrieving in this case a pulse duration of 14.7 fs (FWHM) with a FROG error

of approximately 0.5% (cf. figure 4.7 (b)), which corresponds to a compression factor of 10.2. Minimal residual third-order dispersion is still present in both measured and retrieved FROG traces (figure 4.7 (c) and (d)), as well as in the retrieved pulse duration (figure 4.7 (b)), which is again attributed to the DCM pair.

In addition, caustic measurements were performed to provide a quantitative estimate of the beam quality after passing through the MPC compressor. These result in a measured beam quality factor of  $M_x = 1.05 \pm 0.01$  and  $M_y = 1.06 \pm 0.02$ , as can be seen in figure 4.8. This shows that there is no degradation in beam quality, and may also suggest that beam cleaning is possible in MPCs. However, this is only a hypothesis and would require further thorough investigation.

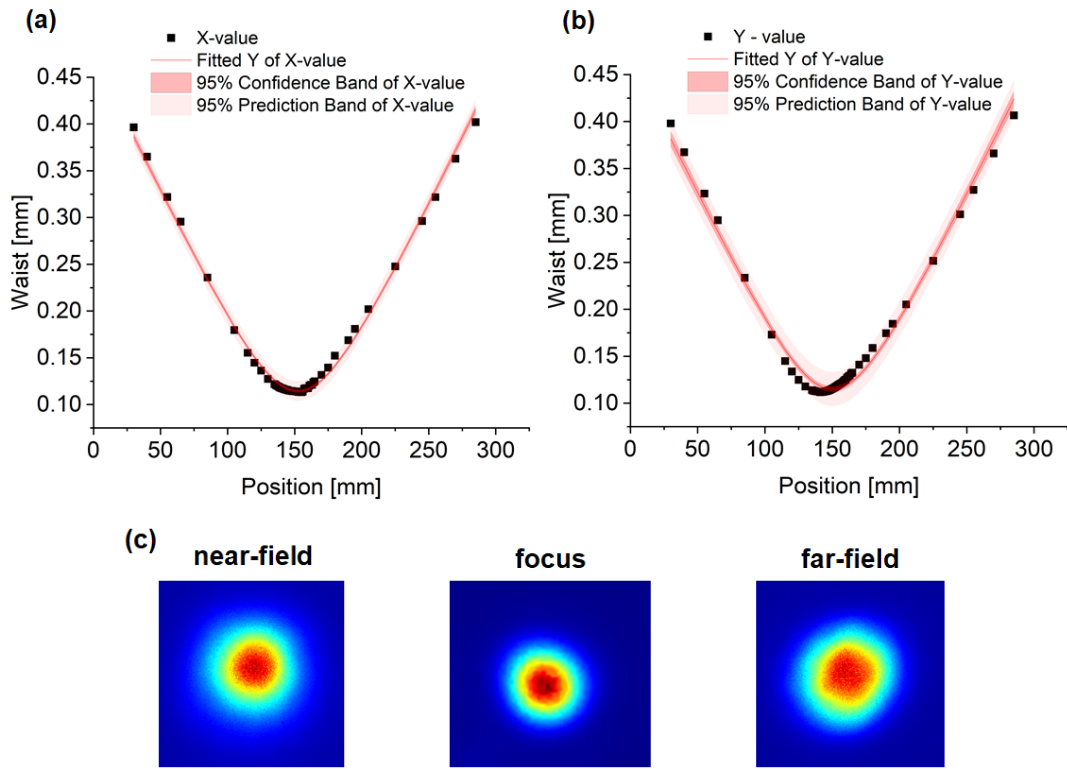


FIGURE 4.8: Output beam profile characteristics of the dispersion-optimised MPC configuration (setup 2). Beam caustic measurements in (a) x- direction (horizontal axis) and (b) y-direction (vertical axis), and corresponding fit for determining the  $M^2$  value. (c) Images of the output beam profile taken in near-field, focus and far-field.

### 4.3 Scaling in average power

So far, the previously presented results have been all achieved at 1 kHz repetition rate, corresponding to about 250 mW average power. The aim of this thesis, however, is to operate a pump-probe beamline at high repetition rates. Therefore, the full capability of the laser system will be exploited in the following, allowing for performances up to 200 kHz repetition rate, which corresponds to about 50 W average power.



FIGURE 4.9: Sketch of the pulse selection modules of the laser incorporating two optical modulators: a pulse picker (PP) to select the repetition rate in the main amplifier, and an external modulator (MOD) for repetition rate and energy adjustment via the software interface. Latter does not affect pulse amplification or compression.

The repetition rate tuning is provided by the laser system itself which comprises two optical modulators: the pulse picker (PP) and the external modulator (MOD), as depicted in figure 4.9. Former is utilised to select the repetition rate in the main amplifier, which is set by the technician upon installation; latter allows the user to adjust the repetition rate and pulse energy of the output pulse via the software interface without affecting the pulse amplification and compression. The maximum values of repetition rate, average power and pulse energy are set by the pulse picker, whereas the external modulator can only adjust these parameters within the predefined range. It is also possible to modify repetition rate and pulse energy independently from each other, meaning, for example, that the pulse energy can be reduced from 100% (full pulse energy) to essentially 0% via the software's internal MOD Efficiency mode at a fixed repetition rate. It should be noted that the energy scaling is not linear; hence 50% MOD Efficiency does not correspond to 50% of the pulse energy and therefore requires additional power measurement. Note that this method of energy tuning has been used for the MPC measurements presented so far.

The average power scalability of the proposed dispersion-optimised MPC configuration has been investigated by gradually increasing the repetition rate up to 200 kHz, without any alterations to the optical setup. The MPC

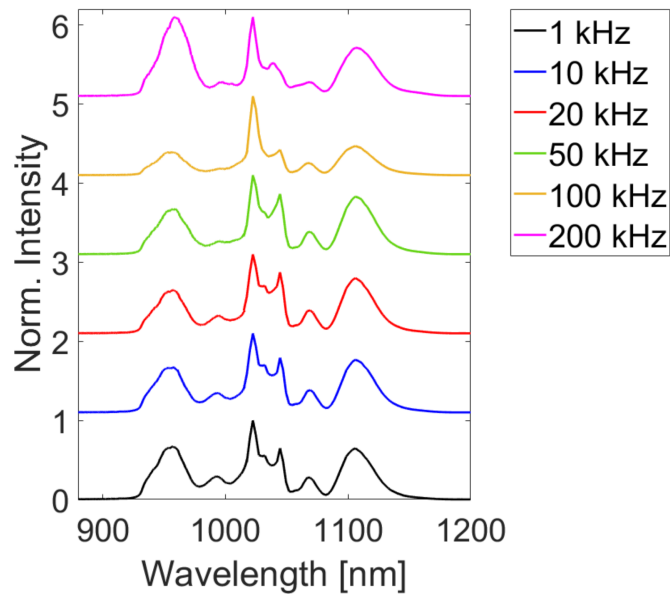


FIGURE 4.10: Comparison of measured MPC output spectra detected at different repetition rates, ranging from 1 kHz to 200 kHz. These rates correspond to average powers ranging from approximately 256 mW to 50 W.

output spectra are measured at 1 kHz, 10 kHz, 20 kHz, 50 kHz, 100 kHz, and 200 kHz using the previously employed two spectrometers. These measurements correspond to approximately 256 mW, 2.57 W, 5.13 W, 13 W, 25.9 W, and 50.6 W of average power, respectively. As can be seen from figure 4.10, the measured spectra generated due to self-phase modulation exhibit each a bandwidth of approximately 200 nm tail-to-tail, resulting in a transform-limited pulse duration of roughly 13 fs at FWHM. This demonstrates that spectral broadening characteristics are preserved upon average power scaling. Moreover, no deterioration in throughput is observed, as it is measured to exceed 90% right at the output of the MPC at each repetition rate. It should be noted that after several months of laser operation, a change in beam size at the front end of the laser system was observed when tuning the repetition rate, which affected the performance of the MPC in terms of spectral broadening. This can be resolved by carefully adjusting the mode-matching of the input beam to the eigenmode of the cavity. As a final remark, it is important to avoid air turbulence when operating the system at high repetition rates (high average powers), as it has been shown to affect the pointing of the beam. Therefore, the optical beam path surrounding the multi-pass cell chamber is enclosed by anodised aluminium plates.

## 4.4 Conclusion

This work has demonstrated the potential of precise dispersion management inside single-stage multi-pass cell compressors based on gaseous media and its effectiveness in improving the SPM-dominated nonlinear broadening process to achieve sub-15 fs pulse durations while maintaining high throughput efficiency and excellent beam quality for large compression factors. The following table provides an overview and summary of the achieved parameters of the three different configurations, namely the conventional MPC utilising only low-GDD cavity mirrors, as described in chapter 3, the dispersion-engineered configuration comprehending two dispersive mirrors, each introducing  $-30 \text{ fs}^2$  GDD operating, however, at reduced pulse energy, and lastly the dispersion-optimised configuration which accomodates the full laser pulse energy:

TABLE 4.1: Summary of pulse post-compression parameters via three different MPC configurations of an Yb-laser centred at 1030 nm wavelength with an initial pulse duration of 150 fs.

	Conventional	Dispersive (Setup 1)	Dispersion optimised (Setup 2)
$N$	22	15	15
Pressure [bar]	1.4	2.7	1.5
$E_{in}$ [ $\mu\text{J}$ ]	250	122	250
$E_{out}$ [ $\mu\text{J}$ ]	215	120	233
Trans. [%]	86	98	93
$\tau_{out}$ [fs]	21.7	16.4	14.7

Moreover, this method enables scaling of average power while maintaining all output characteristics. A further noteworthy observation is better illustrated by comparing this work with previous work, as can be seen in figure 4.11. It is evident that accurate dispersion control enables reaching pulse duration regimes going towards the few-cycle, which were previously accessible only through a cascaded arrangement of MPCs or hybrid setups composed of one MPC and an additional post-compression scheme, within a single-stage MPC. Consequently, this method suggests a solution for making the overall setups more compact. The precise dispersion engineering method introduced in this thesis holds promise for expanding the application scope of MPCs beyond self-phase modulation, towards other nonlinear phenomena such as soliton generation [82], dispersive wave generation [16], four-wave mixing, and nonlinear frequency shifting [83].

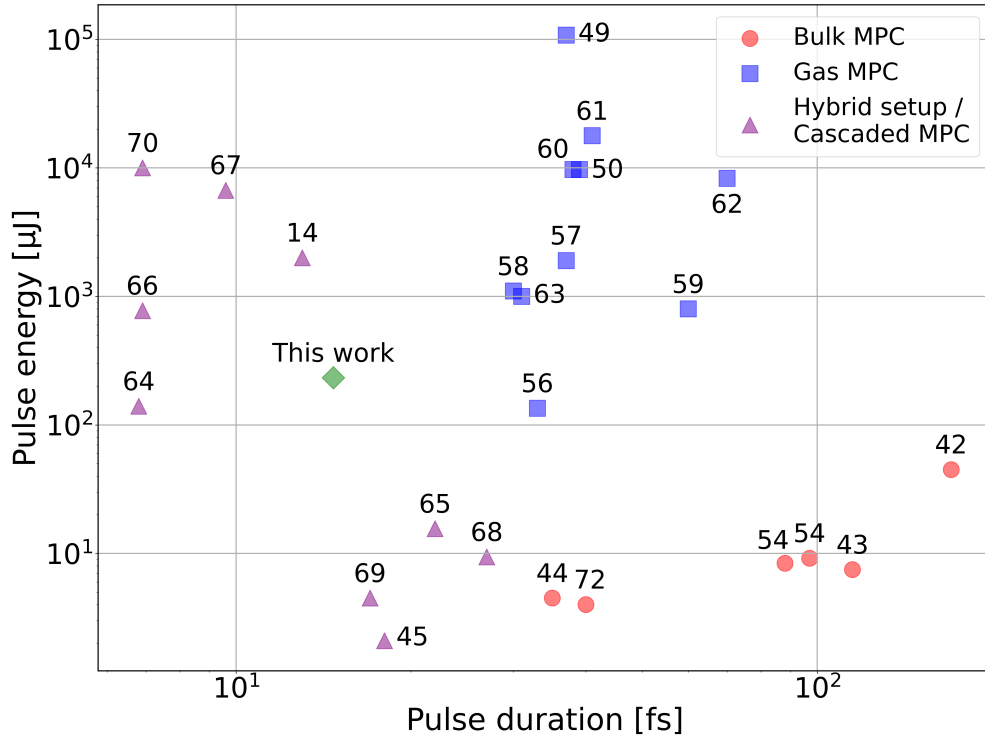


FIGURE 4.11: Comparison of MPC output pulse energy and output pulse duration achieved in this work with results of previous works utilising Yb-based laser systems centred at 1030 nm. The data mentioned here are equivalent to those listed in table 3.1.

## 4.5 Improvement work

Enhancements related to the multi-pass cell technology presented here can be classified into two categories: engineering improvements to the setup and enhancements linked to the physical phenomenon of SPM-based spectral broadening. A significant source of improvement is attributed to the MPC chamber or overpressure chamber, which has been found to be impractical to use. Specifically, the cage assembly comprising the cell mirrors has been observed to be relatively unstable, as the beam alignment is easily lost when air-tightening the chamber. Therefore, an L-shaped clamp connecting the DN 160 flange and the optical table was later added to the chamber design. However, the chamber needs to be closed very carefully to avoid touching the cage assembly, and the tightening of the cylindrical cover to the flange needs to be carried out iteratively to avoid beam misalignments caused by

the bending of the cage assembly inside the chamber.

Another drawback of this design is the actual alignment of the Herriott-pattern on the mirrors. On the one hand, the cell mirror mounts are mounted at 45 degrees, meaning that the x- and y-axes are coupled to each other. On the other hand, the advantage of precisely adjusting the distance between the cavity mirrors by mounting one mirror on a linear stage is no longer available. Therefore, in this work, a combination of one linear stage with screwed posts on top was used to increase the distance between the mirrors, thereby reducing possible tilts of the mirror mounts. Consequently, based on this acquired experience, a monolithic rectangular chamber would be the most suitable solution to achieve a stable and user-friendly MPC setup. It would not only bypass the aforementioned issues, but also facilitate rapid optics exchange while essentially maintaining the distance between the cavity mirrors and beam alignment, necessitating only minor adjustments.

Concerning the improvement of the SPM-based spectral broadening process, the observed restrictions on pulse duration and spectral bandwidth can be circumvented by further improving the coating design of the cell mirrors, with a focus on spectral bandwidth coverage of the group delay dispersion. One approach could involve utilising a mirror pair as cavity mirrors, as demonstrated in [67], due to their renowned capability for covering larger bandwidths with high reflectivity. As a result of the shorter pulse durations and larger bandwidths that can be achieved, the subsequent mirrors for compression and beam steering need to be chosen accordingly. For latter, dielectric mirrors are necessary, as has been observed during this thesis, where thermal effects emerge with metallic mirrors at high average powers.



## Chapter 5

# Few-femtosecond UV generation in HCF

Besides the phenomenon of self-phase modulation, which has been vastly exploited in the previous sections,  $\chi^{(3)}$  effects in nonlinear optical media can also give rise to solitonic waves, or solitons. These shape-preserving waves require the perfect balance between dispersion and nonlinearity to be generated, i.e., the Kerr effect compensates for the dispersive spreading of the pulse during propagation. Under certain conditions, solitons can exhibit very interesting dynamics, such as the emission of a resonant dispersive wave (RDW) when perturbed by higher-order dispersion.

This chapter will introduce the fundamental concepts of soliton formation and RDW emission, along with the scaling rules necessary to observe these dynamics when propagating the laser pulse through a hollow-core fibre (HCF). Following this, experimental implementations and measurements (carried out in collaboration with the LUPO group at Heriot-Watt University in Edinburgh, Scotland), will be presented, demonstrating tuneable RDW emission from the UV range to the visible spectrum. In particular, it will be shown, that the post-compressed pulse from the previously introduced multi-pass cell can efficiently drive these soliton dynamics inside a hollow-core fibre setup.

### 5.1 Introduction

In the field of ultrafast optics, the use of gas-filled waveguides, such as photonic crystal fibres (PCFs) and hollow-core / hollow capillary fibres (HCFs), has benefited various applications, including frequency conversion via Raman scattering [84] and four-wave mixing [85], high-harmonic generation [86, 87], temporal self-compression [88], and pulse compression based on

nonlinear spectral broadening [9, 89], which is one of their main applications.

The operation of PCFs is not limited to these nonlinear effects, but has also demonstrated the efficient generation of tuneable deep ultraviolet (DUV) radiation at the few-femtosecond scale via resonant dispersive wave (RDW) emission from self-compressed solitons. Because these fibres can support only tens of microjoules of pump pulse energies due to their small core sizes, typically in the range of few-tens of micrometres, the conversion efficiency from the infrared to the deep-UV is as high as 8%, corresponding to UV pulse energies of up to 1  $\mu$ J [90, 91, 92, 93]. Moreover, further tuning to the vacuum-ultraviolet (VUV) has also been demonstrated, however, also here with low conversion efficiency ( $\sim 1\%$ ) and VUV pulse energies up to 50 nJ [94]. In contrast, hollow-core fibres can overcome these energy limitations due to their large core sizes, which can extend to hundreds of micrometres. Their dispersion properties scale with core size and are anomalous practically over the entire spectral range. When filled with gas, however, the dispersion landscape of the capillary changes, reaching even the normal dispersion regime, which is unfavourable for soliton formation. This can be counteracted by short enough pump pulses or long fibre lengths to maintain the total dispersion in the anomalous regime. Furthermore, with the advent of the fibre-stretching technique [95], bending losses at long fibre lengths have been significantly reduced. These advancements and observations have enabled the efficient generation of soliton self-compression down to the sub-cycle and tuneable high-energy pulses (up to 16  $\mu$ J) in the range of 110 nm to 400 nm via RDW emission within a gas-filled hollow-core fibre [16].

As the pulse duration of the pump pulse is a key factor for the observation of soliton dynamics, it is common practice to temporally shorten the laser pulses via a first fibre stage solely intended for nonlinear SPM-based spectral broadening with subsequent pulse post-compression. While sub-20 fs durations of the pump pulse have been achieved to drive the RDW in hollow-core fibres [16, 96], these fibre-based compression stages suffer from relatively low fibre throughput and instabilities. MPC-based compressors can offer an alternative solution, providing throughputs well above 90% and optimal beam quality, as discussed and demonstrated in the previous chapters. Hence, this work will prove the efficient generation of tuneable RDW emission in HCF driven by a single-stage gas-based MPC compressor.

## 5.2 Principle of optical solitons and RDW emission

Solitons are self-sustaining waves which arise during propagation in the anomalous dispersion regime through a material with a positive nonlinear refractive index described by 2.10c. To better understand the formation of solitons, it is advantageous to recall the two previously introduced parameters dispersion length  $L_D$  (equation 4.1) and nonlinear length  $L_{NL}$  (equation 4.2), which are derived from the nonlinear Schrödinger equation (NLSE). Analogously to the dispersion control in MPCs for pulse post-compression (cf. chapter 4.1), the behaviour of a soliton is determined by the balance between dispersion and nonlinearity. Therefore, the soliton order can be represented as

$$N^2 = \frac{L_D}{L_{NL}} = \frac{T_0^2 \gamma P_0}{|k_2|}. \quad (5.1)$$

Two types of solitons can be identified from this relation: first-order solitons ( $N = 1$ ) and higher-order solitons ( $N > 1$ ). Former are most commonly referred to as fundamental solitons since their temporal and spectral shape remain constant during propagation. This arises due to the precise balance between dispersion and nonlinearity, where SPM-induced nonlinear phase is continuously compensated for by anomalous dispersion (GDD) as the pulse propagates [97].

Conversely, higher-order solitons evolve periodically upon propagation as the pulse initially experiences self-compression, followed by broadening and compression again, to ultimately return to its initial shape. Their periodicity is described by the soliton period  $z_0 = \frac{\pi}{2} L_D$ , which is not dependent on the soliton order for fixed dispersion length  $L_D$  [97, 98]. This dynamical behaviour can be better understood when considering a non-perturbed higher-order soliton oscillating along the fibre with its soliton period. Initially, the pulse experiences chirp and undergoes spectral broadening induced by the dominating SPM phenomenon. As the bandwidth increases, dispersion effects become prominent, leading to pulse compression. Note that in the initial stage there is some residual positive chirp from SPM. During the self-compression process, anomalous dispersion (from the fibre) plays a significant role as it balances out the SPM-induced chirp by shifting the high- and low-frequency components generated at the trailing and leading edge of the

pulse, respectively, towards the centre of the pulse [97]. This cyclic process of temporal compression and spectral broadening continues until the pulse is maximally self-compressed.

So far, only pure soliton dynamics arising from SPM and second-order dispersion (GDD) have been considered, which, however, are not present in real experimental settings. Hence, an important aspect to include in these observations is the perturbation of solitons by higher-order dispersions and higher-order nonlinearities, as it leads to soliton fission at the point of maximum temporal self-compression and the broadest spectrum of the pulse [99]. In this context, the characteristic soliton fission length is approximately defined as [100]

$$L_{\text{fiss}} = \frac{L_D}{N} \quad (5.2)$$

and describes the exact length at which the soliton self-compresses and a resonant dispersive wave (RDW) is emitted. The scaling laws for the propagation of very high-order solitons ( $N$  up to 40) are numerically found to be  $F_{\text{SC}} \approx 4.6N$  and  $Q_{\text{SC}} \approx 3.7/N$  [101]. Former symbolises the self-compression factor, which is calculated by the ratio of the initial pulse duration to the compressed pulse duration at FWHM; latter represents the compression quality factor, which is determined by the energy ratio contained within the pulse duration of the compressed pulse to the initial pulse duration at FWHM. Consequently, increasing the soliton order to achieve shorter self-compressed pulse durations results in a deterioration of the compressed pulse quality, thus imposing constraints on the maximum soliton number usable to obtain high-quality short pulses [101]. Note that the quality of the self-compressed pulse refers to the amount of total energy contained in the main peak of the compressed pulse compared to the pedestals. Hence, achieving direct soliton self-compression to the single-cycle regime requires sufficiently short pump pulses. As a result, few-hundred femtosecond pulses from Yb-based fibre laser systems, for example, are not suitable and would therefore require initial pulse compression.

Interestingly, the perturbation of optical solitons by higher-order dispersions causes energy transfer to a phase-matched linear wave at a resonance frequency different from the soliton's centre frequency [102]. This phenomenon, known as resonant dispersive wave (RDW) emission, occurs at the fission

point when the pulse achieves its shortest self-compressed duration and broadest spectrum, extending well beyond the fibre's zero-dispersion wavelength (ZDW) into the normal dispersion region. The RDW emission frequency needs to satisfy the momentum conservation relation

$$\beta(\omega) = \beta_{\text{sol}}(\omega) \quad (5.3)$$

where  $\beta$  and  $\beta_{\text{sol}}$  are the propagation constants of the linear wave and soliton at angular frequency  $\omega$ , respectively. Latter is described by

$$\beta_{\text{sol}}(\omega) = \beta(\omega_{\text{sol}}) + \beta_1(\omega_{\text{sol}}) [\omega - \omega_{\text{sol}}] + \frac{\gamma P_0}{2} \quad (5.4)$$

with the soliton centre frequency  $\omega_{\text{sol}}$ , the peak power of the initial pulse  $P_0$  and the nonlinear coefficient  $\gamma$ , which is proportional to the nonlinear refractive index  $n_2$  of the medium [103, 104]. Thus, the phase-matching and RDW emission wavelength can be adjusted by the dispersion within a gas-based HCF through gas pressure, and by the peak power of the soliton through the input pulse energy and its duration. An exemplary spectrum of a self-compressed soliton with the emission of a resonant dispersive wave achieved in a gas-filled hollow-core fibre is depicted in figure 5.1.

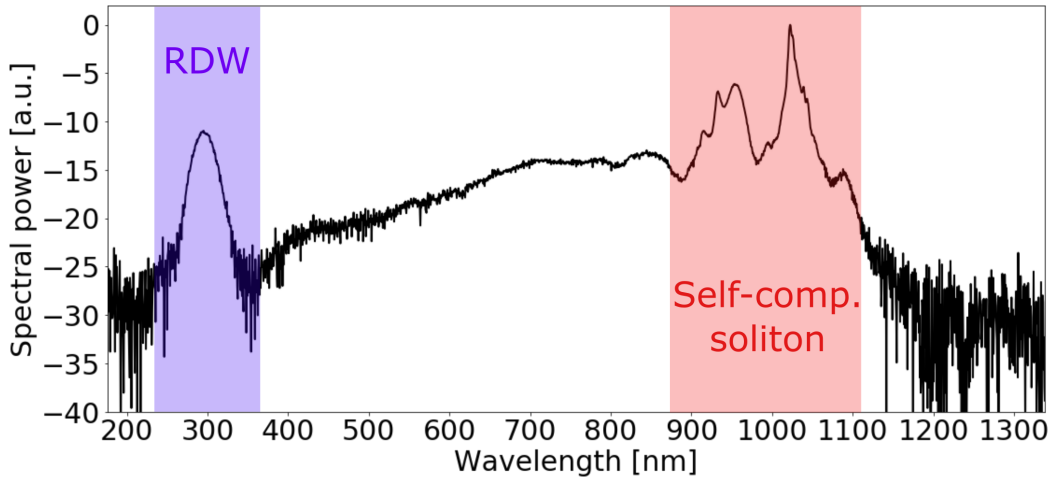


FIGURE 5.1: Generated spectrum at the output of a hollow-core fibre operated in negative pressure gradient at 1 kHz repetition rate. In this example, the sub-20 fs compressed pulses from the MPC are used to drive the resonant dispersive wave centred around 290 nm for 350 mbar of argon. Spectrum plotted in logarithmic scale.

### 5.3 MPC driven resonant dispersive wave emission in a hollow-core fibre

The conditions under which soliton dynamics are observed underlie specific scaling rules, which are designed to achieve a proper balance between non-linearity and dispersion. For pump pulses in the infrared region, soliton propagation through a nonlinear medium, such as noble gases, takes place in the anomalous dispersion regime, i.e.,  $D_2(\lambda_0) < 0$  (as defined in equation 2.5), with  $\lambda_0$  being the centre wavelength of the pump pulse. The target point of RDW emission is determined by the zero-dispersion wavelength, as the dispersion changes its sign. Hence, considering a fixed ZDW, the dispersion length of a hollow-core fibre can be defined as [104]

$$L_{\text{disp}}^{\text{HCF}} \propto a^2 \tau_0^2. \quad (5.5)$$

From this relation it is clear that the dispersion length is mainly affected by the core size of the fibre  $a$  and the pulse duration of the pump  $\tau_0$ . Another important parameter is the fission length which determines soliton self-compression and resonant dispersive wave emission. Based on equation 5.2 and considering also here a fixed ZDW and pump wavelength, the fission length in a hollow-core fibre is determined by

$$L_{\text{fiss}}^{\text{HCF}} \propto \frac{\tau_{\text{FWHM}} a^2}{\sqrt{I_0}} \quad (5.6)$$

which is dependent on the pump pulse duration at FWHM  $\tau_{\text{FWHM}}$  and inversely proportional to the square root of the peak intensity  $I_0$  [16]. The observation of soliton dynamics in hollow-core fibres is therefore conditioned by the relation

$$L_{\text{fiss}} \lesssim L_{\text{loss}} \quad (5.7)$$

to prevent or hinder losses related to the HCF that might interfere with these dynamics [16]. Since  $L_{\text{loss}}^{\text{HCF}} \propto a^3$  and the fission length is proportional to  $a^2$  (see equation 5.6), the specified relation between fission length and loss length can be fulfilled for large core size fibres but with long fibre length. Latter can be reduced by decreasing the pulse duration of the pump [16, 104].

Based on these scaling rules, and in collaboration with the group of John Travers at the Herriot-Watt University in Edinburgh (Scotland), a fibre setup has been designed, which is pumped by sub-20 fs pulses from a multi-pass cell pulse post-compressor. In the following, the experimental layout and achievements will be presented and discussed.

### 5.3.1 Experimental setup

For the efficient generation of tuneable resonant dispersive wave, a two-stage setup has been used and is depicted in figure 5.2. Firstly, the laser pulses are compressed down to sub-20 fs via the previously introduced dispersion-engineered multi-pass cell (cf. chapter 4.2.2). In a second stage, a hollow-core fibre setup is employed to generate deep ultraviolet (DUV) radiation. To control the input pulse energy, a broadband attenuator is utilised. It consists of an air-spaced  $\frac{\lambda}{2}$  - waveplate (HWP) with a clear aperture of 19.5 mm in diameter and covers a spectral range from 600 to 1200 nm (provided by B-Halle), and a 2-inch thin-film polariser (TFP) with a substrate thickness of 9.52 mm. Latter is coated for a spectral range of 925-1150 nm, offering an average reflectivity  $R_s > 85 - 90\%$  at an angle of incidence (AOI) of  $72^\circ$  (provided by Laser Components). The transmitted beam through the TFP is intercepted by a beam block, whereas the reflected beam is directed towards a mirror telescope for coupling into the fibre. These broadband dielectric mirrors have a radius of curvature of  $ROC_1 = +1000$  mm (M1) and  $ROC_2 = -1000$  mm (M2), resulting in a focus spot size of about  $134 \times 132 \mu\text{m}$ , i.e. approximately 67% of the fibre's core size. Both mirrors are installed in motorised mirror mounts (Picomotor mounts by Newport) to achieve better alignment precision and improved coupling conditions. Additionally, the concave mirror is mounted on a manual linear stage for fine adjustments of the focus position and size.

A polymicro capillary is used for the generation of RDW emission, and its parameters are calculated based on the previously mentioned scaling rules which result in a 1.7 meter long fibre with a core diameter of  $200 \mu\text{m}$ . The fibre is stretched and cleaved manually, and each end is glued onto a V-groove chuck. The inlet and outlet of the fibre setup are each enclosed in a gas cell and sealed. The two cells are not connected by a single tube, leaving the HCF exposed and vulnerable to accidental damage. To protect it, a plastic cover is mounted around the fibre. Moreover, the fibre between the two gas cells exits each cell through a short steel tube with an inner diameter of 3 mm,

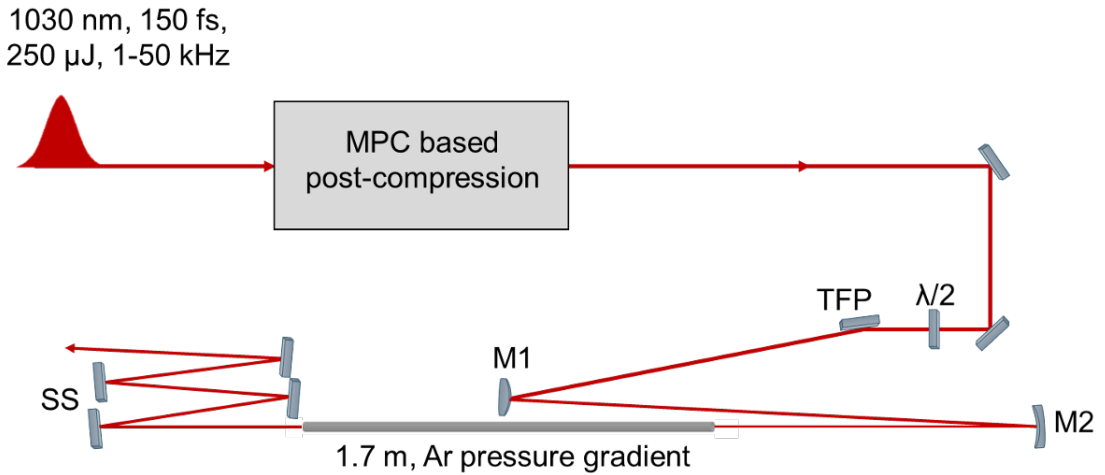


FIGURE 5.2: Overall experimental setup comprising a 1.7 m long gas-filled hollow-core fibre with a core size of  $200\ \mu\text{m}$ , pumped by sub-20 fs pulses from a multi-pass cell for resonant dispersive wave emission. The MPC-based compressed pulses are directed through a variable broadband attenuator composed of a half-waveplate ( $\lambda/2$ ) and thin-film polariser (TFP), followed by a mirror telescope (M1: convex mirror, M2: concave mirror) for HCF coupling. The fibre is filled with argon gas at different pressures to achieve RDW tuning and operated in negative pressure gradient.

which must be filled with glue to ensure a proper seal. Note that UV-cured optical component adhesive is used for gluing the fibre, as it is compatible with high vacuum environments due to its low outgassing properties, and provides long-term stability for the adhesion of glass to metal. The gas cells are mounted on pedestals to match the fibre's height with the MPC output beam height, resulting in roughly 130 mm from the optical table. Approximately 500 mm from the fibre tip on the inlet side, a half-inch, 1 mm thick fused silica window with an antireflection coating (covering the wavelength range 950-1150 nm) is mounted and connected to the gas cell by a tube. This distance is chosen to prevent damage to the window caused by the focusing of the beam for fibre coupling. On the outlet side of the fibre, a 1-inch, 1 mm thick uncoated fused silica window is installed inside a mount with a clear aperture of 20 mm in diameter at the aforementioned distance. This fibre setup allows for the independent pumping and gas filling of the cells. A negative pressure gradient [103] operation is employed, where the nonlinear gas is injected at the inlet of the HCF setup and a single roughing pump is connected to the outlet for continuous pumping. In this case, the gradient configuration is preferred over the static one, as the HCF setup will be

directly connected to a vacuum chamber as the main UV source of a pump-probe beamline. A digital gauge is connected at the fiber input to measure the gas pressure. Lastly, at the fibre output, four 1-inch spectral separators (SS) from Optoman are used for the separation of UV and IR light, allowing for UV energy measurements. These separators provide reflectivity above 70% within the specified wavelength range of 210 - 360 nm at  $\text{AOI} = 0^\circ - 25^\circ$ .

### 5.3.2 RDW tuneability range

Initial tests of driving resonant dispersive wave emission in a hollow-core fibre via post-compressed pulses based on the MPC method are performed at 1 kHz repetition rate, where about 15 fs pulses are coupled into an argon-filled HCF. The total effective pulse energy obtained after the pulse compression stage is approximately  $214 \mu\text{J}$ . Subsequent losses occur due to the broadband attenuator and broadband dielectric steering mirrors. Latter are specifically designed for a wavelength range of 925 - 1150 nm, offering high reflectivity of about 98% at low GDD. Consequently, the maximum energy available at the fibre input amounts to approximately  $180 \mu\text{J}$ . Before starting the actual measurements, it is important to perform a leak test of the fibre setup to avoid air contamination. Afterwards, the beam coupling into the fibre is optimised, reaching a maximum transmission of about 44% in vacuum for this specific HCF. A calibration of the HWP is performed prior to the RDW measurements to establish a quantitative relation between the HWP's angle and the corresponding pulse energy that is sent into the fibre. The generated spectra are acquired directly at the fibre output (before the spectral separators) via an integrating sphere connected to the AvaSpec 2048XL spectrometer by Avantes. Figure 5.3 depicts the tuneability range of the resonant dispersive wave at 1 kHz repetition rate (250 mW average power), generated in argon gas under a negative pressure gradient ranging from 300 mbar to 950 mbar. The total RDW range extends from 270 nm at low gas pressure (300 mbar) with maximum energy ( $\sim 180 \mu\text{J}$ ) to approximately 530 nm at high gas pressure (950 mbar) with reduced energy ( $\sim 85 \mu\text{J}$ ). This tuning process towards longer RDW centre wavelengths is related to an increase in nonlinearity when utilising higher gas pressures. Therefore, by utilising lower pump energies to drive the RDW, saturation can be avoided while the group velocity dispersion (GVD) of the hollow-core fibre becomes more pronounced [96]. The total transmission, measured directly at the output of the fibre, amounts to

about 38% at lower gas pressures and reduces to roughly 34% at higher pressures. The energy content of the RDW emitted UV light is measured after the four spectral separators and amounts to approximately  $1.24 \mu\text{J}$  at 270 nm and roughly  $2.09 \mu\text{J}$  at 350 nm, considering the losses introduced by the SS. Energy measurements of the resonant dispersive wave emitted even beyond the UV into the visible could not be performed due to the unavailability of spectral separators covering the specifically generated spectral range. Note that the resonant dispersive wave is primarily generated in the fundamental mode of the hollow-core fibre, specifically the  $\text{HE}_{11}$  mode.

TABLE 5.1: Measured parameters at 1 kHz repetition rate comprehending the gas pressure (in gradient configuration), the input and output power of the HCF, the UV pulse energy, the centre wavelength of the generated RDW and the calculated transform limit (FWHM) of the RDW emitted in the UV. The energy content of the UV listed in the table also includes the losses introduced by four spectral separators.

Pressure [mbar]	$P_{\text{in}}$ [mW]	$P_{\text{out}}$ [mW]	$\lambda_{\text{RDW}}$ [nm]	$E_{\text{UV}}$ [ $\mu\text{J}$ ]	$\text{TL}_{\text{UV}}$ [fs]
300	180	69	270	1.24	3.3
350	180	67	295	0.84	3.5
400	160	60	310	1.39	3.3
450	144	50	335	1.59	3.5
500	110	43	350	2.09	3.5
550	110	35	360		
600	98	32	400		
640	98	28	420		
700	98	32	440		
750	85	26	450		
800	85	27	470		
850	85	26	500		
900	85	27	510		
950	85	29	530		

The Fourier transform limit at FWHM of each RDW curve in the UV region is computed, resulting in approximately 3.3 fs pulse at the shortest generated wavelength and assuming a flat phase. The transform limit increases slightly to roughly 3.5 fs at an RDW centre wavelength of 350 nm. A comprehensive and detailed list of the achieved parameters is documented in table 5.1. The generated UV light, however, is assumed to be slightly chirped, as in this specific case the light travels through dispersive media, specifically the

output window of the fibre setup and air.

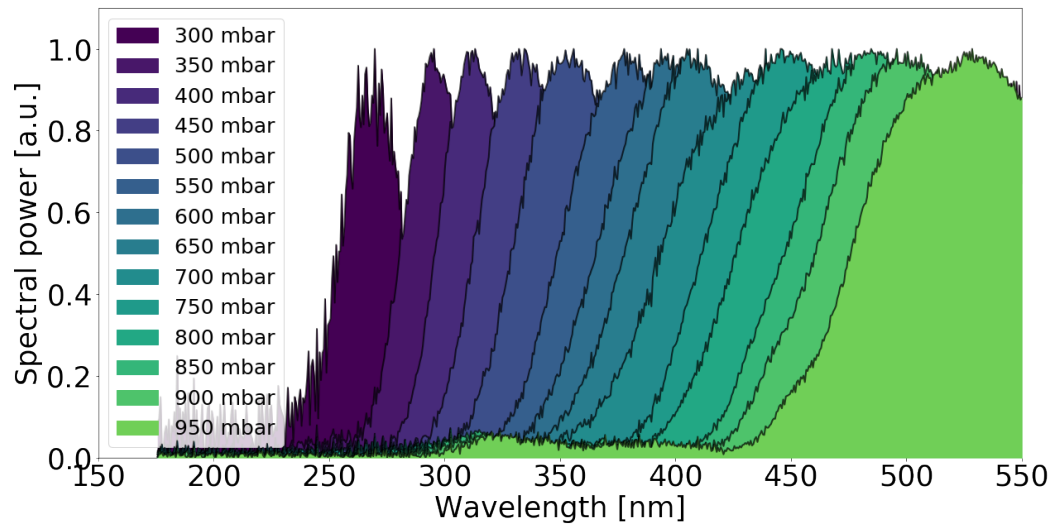


FIGURE 5.3: Tuneability range of RDW emission in a hollow-core fibre acquired in argon in negative pressure gradient configuration at 1 kHz repetition rate. Higher gas pressures and lower pump pulse energies are employed to target longer RDW wavelengths.

The direct temporal characterisation of the generated UV pulses is quite challenging in this spectral region. However, several methods have been developed over the years, including the fringe-resolved interferometric autocorrelation (FRIAC) technique [105], which is planned to be used with this fibre setup in the near future in collaboration with the group of Prof. Markus Drescher from Hamburg University. This method exploits an interlocked reflective grating, specifically a silicon double-comb mirror (D-CM), for wavefront splitting. This creates a diffraction pattern with well-defined orders and intensity distribution, as the two partial beams propagate with a small angle between them, resulting in partial destructive interference. An advantage of this method is that it allows for the extraction of information on both the pulse duration and the temporal phase of UV light.

### 5.3.3 Scaling in average power

The successful generation of tuneable RDW by combining a multi-pass cell for pulse post-compression with a hollow-core fibre for the dispersive wave emission has been tested at 1 kHz. The current challenge is to scale the repetition rate up to ideal 200 kHz, corresponding to 50 W average power. In a recent work, promising results have been achieved in a compact two-stage HCF setup for initial pulse compression and subsequent RDW emission operating at 50 kHz repetition rate [96]; however, it suffers from low fibre throughput and instabilities in the compression stage. Therefore, this section presents tests on increasing the average power of the setup that incorporates MPC and HCF.

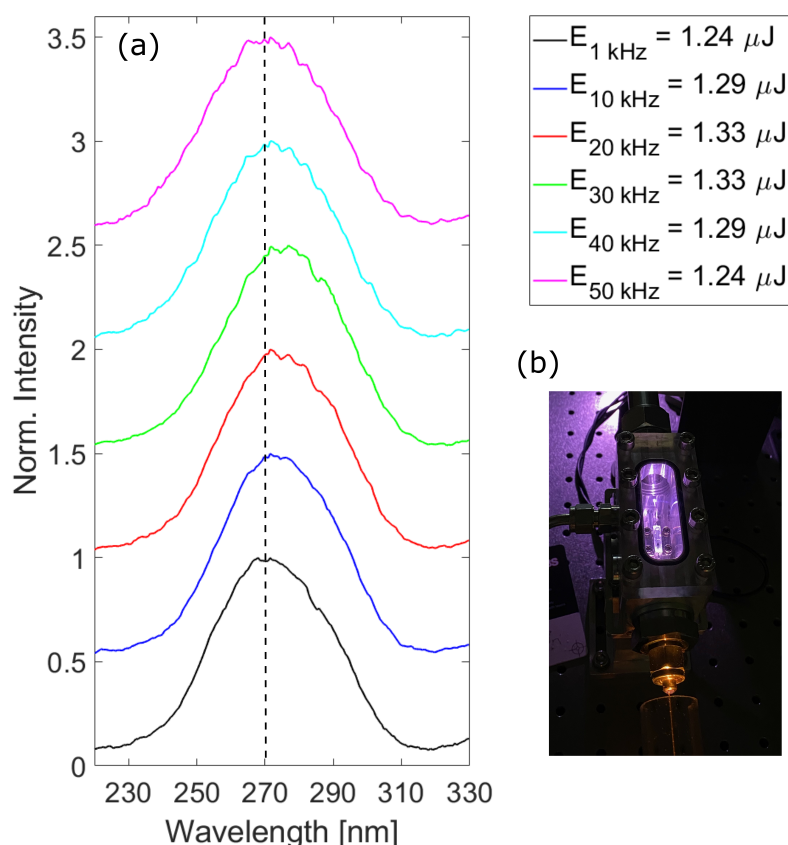


FIGURE 5.4: (a) Average power scalability of the resonant dispersive wave centred at about 270 nm wavelength, generated in argon in negative pressure gradient configuration. The UV energy content of the pulse at different repetition rates is provided in the legend. (b) Image of the hollow-core fibre output emitting UV light.

The measurements are performed by gradually increasing the repetition rate starting from 1 kHz (250 mW laser average power) up to 50 kHz ( $\sim 13$  W

laser average power) while keeping the RDW at one fixed centre wavelength. As before, the spectra are measured directly at the fibre exit by an integrating sphere connected to the AvaSpec 2048XL spectrometer. Figure 5.4 (a) depicts the normalised spectra of the resonant dispersive wave centred at approximately 270 nm for input average powers 180 mW, 1.7 W, 3.8 W, 5.9 W, 7.8 W and 9.4 W, and argon pressures around 330 mbar (at low repetition rate) and 350 mbar (at high repetition rate). Note that these average power values refer to the power available at the input of the fibre setup. The total transmission through the fibre ranges from 39% to 37% at low and high average power, respectively. A slight shift in centre wavelength of a few nanometres is noticeable at different repetition rates due to the gas pressure not being entirely stable and requiring occasional fine adjustments, as the fibre is continuously evacuated at its end to maintain the pressure gradient. Additionally, minor beam pointing instabilities also contribute to this shift in RDW wavelength, as the setup operates without a pointing stabilisation system and air fluctuations, particularly at higher average powers, affect the beam. Accounting for the losses of the four spectral separators, the pulse energy content of the generated UV light amounts to a minimum of approximately  $1.24 \mu\text{J}$  at 1 kHz and 50 kHz repetition rate, and a maximum of about  $1.33 \mu\text{J}$  at 20 kHz and 30 kHz. The spectral bandwidth of the emitted RDW supports pulse durations of approximately 3 fs (FWHM) at all average powers / repetition rates. Consequently, all parameters of the generated dispersive wave emitted at 270 nm are preserved when increasing the average power, with no significant losses.

Having demonstrated that the resonant dispersive wave generation at a fixed centre wavelength and low gas pressures remains practically unaffected by increases in average power, the next step is to determine its tunability range, which may be particularly critical at higher repetition rates, and therefore higher average powers, with large gas pressures. Initial measurements at 10 kHz, corresponding to approximately 1.7 W average power of the pulse at the fibre input, demonstrate the reproducibility of the RDW tuning range previously achieved at low repetition rate (1 kHz), as depicted in figure 5.5 (a). Also in this case argon gas has been chosen for the RDW generation. The total transmission, measured directly at the fibre output, remains quite stable across all gas pressures and amounts to about 38%. Accounting for the losses introduced by the spectral separators, the energy contained within the UV pulse centred at 270 nm amounts to about  $1.29 \mu\text{J}$  and

decreases slightly to roughly  $1.12 \mu\text{J}$  at 350 nm. The generated spectral bandwidths support Fourier transform limited pulse durations of approximately 3 fs (FWHM) at the shortest wavelength, increasing to roughly 3.6 fs (FWHM) at 350 nm. These results are consistent with the achievements observed at 1 kHz repetition rate.

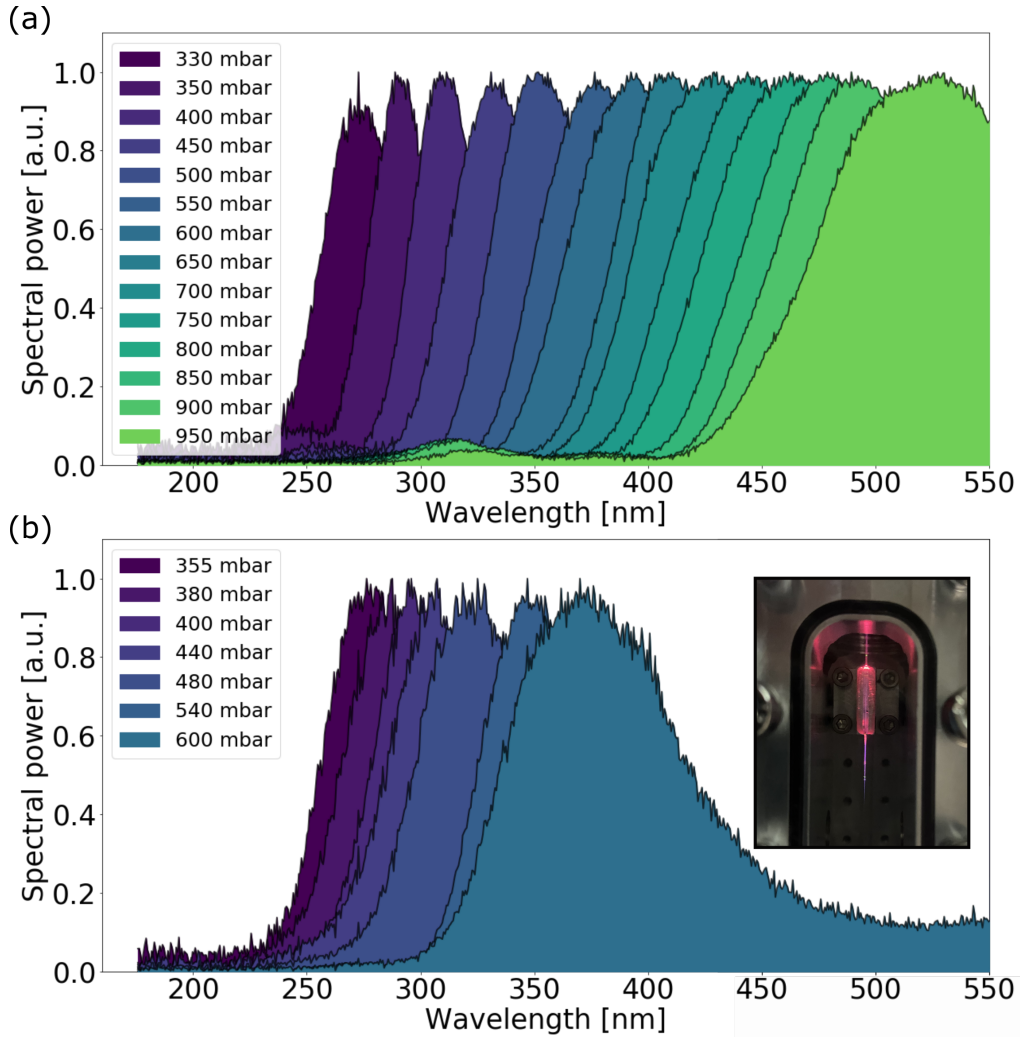


FIGURE 5.5: Tuneability range of RDW emission in a hollow-core fibre acquired in argon in negative pressure gradient configuration at (a) 10 kHz repetition rate and (b) 50 kHz repetition rate. Inset displays the onset of filamentation at the fibre tip for gas pressures exceeding 500 mbar at 50 kHz.

In contrast, the tuneability range of the resonant dispersive wave is significantly shorter at 50 kHz repetition rate, as illustrated in figure 5.5 (b), spanning only from 270 nm to 370 nm. Regarding the characteristics of the emitted RDW, the pulse energy at the shortest wavelengths (270 nm) is approximately  $1.24 \mu\text{J}$ , and its spectral bandwidth supports pulse durations of

about 3 fs at FWHM. This is consistent with the results achieved at lower average powers and repetition rates (cf. figure 5.4 (a)). As the dispersive wave is tuned towards longer wavelengths, however, its pulse energy decreases drastically to about  $1 \mu\text{J}$  and below, starting from a centre wavelength of 330 nm. On the other hand, there are no significant changes in the fourier transform limited pulse duration, reaching roughly 3.6 fs (FWHM) at 350 nm, which aligns with earlier observations. The decrease in UV pulse energy at higher gas pressures and longer RDW wavelength, along with the limited tuneability range, is due to the onset of filamentation which causes damage to the fibre tip (cf. inset in figure 5.5 (b)). In fact, the total transmission through the fibre drops drastically to approximately 21% at higher gas pressures due to the fibre tip burning away, which significantly impairs the beam coupling into the fibre. This suggests that in this specific configuration, at high repetition rates, heat builds up in the medium due to insufficient heat dissipation time between pulses. This thermal accumulation induces thermal lensing which could potentially enhance self-focusing effects that result in filamentation.

## 5.4 Conclusion and Improvement work

So far, resonant dispersive wave emission in gas-based hollow-core fibres reaching the deep-UV regime has been achieved in a cascaded arrangement of fibre setups, where the first one is used for pulse post-compression to subsequently drive the RDW in a second HCF. In this work, however, the first fibre compression stage has been replaced by a gas-based multi-pass cell pulse post-compressor, demonstrating an efficient and robust method for driving resonant dispersive wave in a gas-filled hollow-core fibre. To be precise, a tuneability range from the deep-UV at 270 nm all the way up to the visible at 530 nm, with UV pulse energies at the microjoule level and supporting few-cycle pulses, has been achieved. Additionally, the repetition rate and average power scalability of the entire setup, tested up to 50 kHz and 13 W respectively, demonstrated that the RDW spectral shape in the deep-UV regime remains preserved during average power upscaling. The observed high losses in the separation of the generated UV from the fundamental IR can be circumvented by improving the coating design of the spectral separators. Alternatively, silicon wafers can be used for this purpose, which have been successfully implemented in previous works [106].

Another observation resulting from these tests is the restriction set by the onset of filamentation, which causes a shorter tuneability range achievable at the highest average power/repetition rate and significantly reduces the RDW pulse energy at longer target wavelengths. Using a medium with higher ionisation potential, such as neon or helium, could not only resolve this limitation but has also shown an extension of the RDW cut-off towards the VUV region, achieving wavelengths shorter than 120 nm for helium [107].

As air convection resulting from the increased repetition rate has proven to affect the beam pointing, implementing a stabilisation system in the fibre setup would be beneficial, a measure that has already been addressed and is currently being implemented. Due to space constraints, this system is designed to pick up the leaked beam of the defocusing mirror telescope and send it to a stabilisation camera by means of different optics. On the outlet side of the fibre, the fused silica window could be replaced by a magnesium fluoride window of the same thickness, as it has higher transmission properties extending into the VUV compared to fused silica, which could improve the UV yield through the fibre. This improvement is, however, only useful for current tests and would be instead irrelevant for future pump-probe measurements, as the fibre output will be directly connected to a vacuum chamber, thereby bypassing the need for an output window.

The implementation of the here suggested modifications and improvements should allow for further measurements dedicated to the upscaling in average power and repetition rate, reaching up to 50 W and 200 kHz, respectively.

## 5.5 Outlook on UV-pump and IR-probe beamline

The achievements presented in this thesis will be crucial elements of an ultrafast UV-IR pump-probe beamline, aimed to operate at 200 kHz repetition rate. To this end, significant efforts have been made to conceptualise a pump-probe scheme, as will be presented in the following.

In an initial layout, the table-top beamline, composed of a few-femtosecond UV-pump and IR-probe, is designed to separate the fibre output into two distinct pathways: the RDW emitted in the UV and the self-compressed soliton in the IR. As can be seen from the overall pump and probe setup in figure 5.6, the diverging output beam first needs to be collimated by a concave mirror

(CM) to achieve a collimated beam size of 5 mm in diameter. Via two steering mirrors, the UV is then reflected on silicon wafers to separate the UV from the IR. According to the polarisation of the light (s-polarised), these wafers need to be mounted vertically on a periscope and reflect the UV light at Brewster's angle to reduce losses. At this point, the height difference between the transmitted IR and the reflected UV is considered to be approximately 5 cm. The height difference between the UV and IR beams can be adjusted after their separation by minimally tuning the vertical axis of one or two steering mirrors of the UV arm, without changing its polarisation. Alternatively, a second periscope may need to be implemented. The collimation of the beam and separation of the two wavelengths take place in a first smaller vacuum chamber with the dimensions  $330 \times 280 \times 262$  mm, which includes a 30 mm thick plexiglass lid for beam path observation. This chamber will be directly attached to the output of the fibre via a long enough tube and a bellow.

From the first vacuum chamber, the two separated radiations are directed along two distinct paths towards a second, larger vacuum chamber with the dimensions  $560 \times 530 \times 260$  mm. The IR arm includes steering mirrors and a delay stage used for pump-probe experiments to time the arrival of the IR pulses. The UV arm is designed to integrate a stationary FRIAC setup for temporal pulse characterisation of the UV radiation. This setup allows the UV beam to either propagate through the chamber via steering mirrors or be directed for temporal characterisation by moving two 45-degree steering mirrors, each mounted on a motorised linear stage, out of the beam path. Lastly, the two arms propagate through a second large vacuum chamber, identical to the previous one. Here, both the UV and IR arms are each focused into an experimental chamber by a focusing mirror (FM). To direct the two beams towards the experiment, a drilled mirror (DM) mounted on a motorised linear stage is utilised, allowing the UV radiation to pass through the hole while the IR is reflected on the mirror surface. Hence, the total length of the two arms amounts to 2638 mm.

For the UV arm aluminium optics need to be used, whereas either broadband dielectric optics with low GDD or metallic mirrors could be employed for the IR arm, depending on whether thermal effects arise with metallic mirrors at higher repetition rate and average power. The beamline includes also motorised irises and motorised mirror mounts, which are all vacuum compatible. Moreover, motorised vacuum-compatible gate valves with a

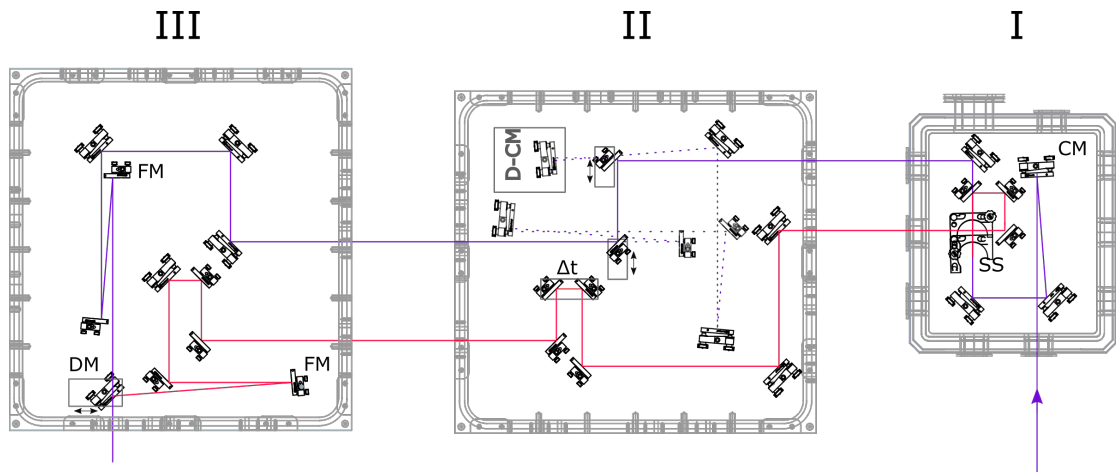


FIGURE 5.6: Schematic overview of the UV-pump and IR-probe beam paths. Vacuum chamber I is connected to the outlet of the fibre setup. It contains a collimation mirror (CM) to collimate the divergent beam exiting the fibre and spectral separators (SS) for the separation of UV and IR radiation into distinct beam paths. The two beams are then directed towards a larger vacuum chamber II, which incorporates a delay stage ( $\Delta t$ ) in the IR arm. The UV arm includes a temporal pulse characterisation setup based on the FRIAC method, featuring a double-comb mirror (D-CM). The beam path of this characterisation setup is indicated by the dashed violet lines. Vacuum chamber III contains a focusing mirror (FM) in each arm to focus the two beams onto a sample target for time-resolved spectroscopy measurements. The copropagation of the two beams towards the experiment is achieved via a drilled mirror (DM), which reflects the IR beam while transmitting the UV pulse. Black arrow: movement direction of the motorised linear stage.

mounted window will be installed between the chambers to enable alignment of the two arms under vacuum. Concerning the pumping, a magnetically levitated turbopump ATH1603 M by Pfeiffer is attached to the last vacuum chamber and should be sufficient to keep the vacuum level  $\leq 10^{-6}$  mbar in both big chambers. However, there is the option to attach one more turbopump on the first big chamber. The pumping of the smaller chamber, which is connected to the fibre output, is provided by an Ecodry 40 plus by Leybold. Vacuum tests have shown that a vacuum level of  $8 \times 10^{-2}$  mbar can be held for 1.4 bar of argon gas pressure operated in negative gradient inside the fibre. Alternatively, instead of separating the UV and IR after they exit the fibre, a second design for the pump and probe beamline could involve splitting the beam before it is coupled into the fibre. This would create an IR arm that propagates parallel to the fibre and is directed into the first

small vacuum chamber, while the residual IR from the fibre would be fully attenuated, leaving only the UV light.

## UV-IR separation

As mentioned before, in order to get a functioning UV-pump and IR-probe beamline, one approach is to separate the resonant dispersive wave emitted in the UV from the soliton self-compressed fundamental in the IR. The challenge here is to preserve the characteristics of both radiations as much as possible, with only minor losses in energy and minimal temporal stretching. So far, throughout this work spectral separators have been used to attenuate the fundamental for UV energy measurements. However, for future applications, the separators are not optimal as they have a defined GDD  $< 15 \text{ fs}^2$  over the wavelength range 210-360 nm. This would cause a significant temporal stretching of the generated sub-4 fs UV pulses. In addition, these SS introduce spectral modulations in the region from about 350 nm to 500 nm (cf. figure 5.7), since the generated supercontinuum spectrum extends weakly up to roughly 350 nm before emitting the RDW at 270 nm.

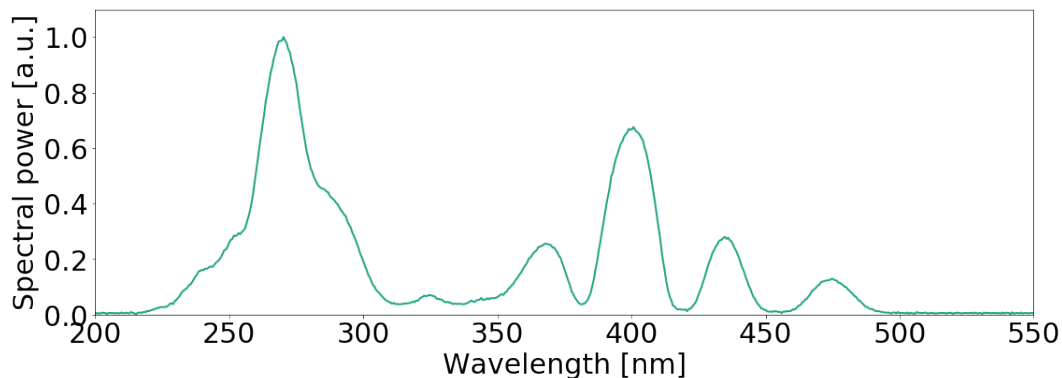


FIGURE 5.7: Example of the UV spectrum measured after four spectral separators. The RDW is emitted at approximately 270 nm from an HCF filled with 355 mbar of argon in negative pressure gradient at 50 kHz repetition rate.

An alternative approach involves using silicon wafers, which have good reflection properties in the UV range but higher absorption in the IR region [23], addressing the issue of temporal stretching in the UV. To reduce the IR losses in transmission, a 2-inch diameter silicon substrate with a minimum thickness of  $80 \mu\text{m}$  and polished on both sides will be used, affecting only minimally the temporal profile of the IR. Thus, the separation of IR and UV into two distinct pathways occurs with this first silicon wafer, where the IR

passes through the substrate and the UV is reflected vertically onto another thicker silicon wafer. Since a small portion of IR will be reflected along with the UV, the precise number of wafers required to fully attenuate this residual IR must be determined experimentally.

## Chapter 6

# Conclusions

Within the scope of this thesis, advancements in pulse compression techniques as well as in the generation of broadband ultraviolet light have been exploited to design and construct a novel and compact tuneable few-femtosecond UV source operated at high repetition rate, which constitutes the backbone of a table-top UV-pump and IR-probe beamline, making it a valuable source for time-resolved spectroscopy experiments on molecules.

One of the fundamental components of this beamline is the multi-pass cell technique, which has undergone remarkably rapid development in less than a decade. It offers a straightforward, compact, and highly effective solution for pulse post-compression, delivering excellent beam quality and pointing stability. Nowadays, it has found applications in many laboratories even to the extent of being commercialised by companies. This scheme provides numerous ways to fine-tune and control nonlinear interactions by adjusting various aspects of the multi-pass cell configuration, including its geometry, the choice of nonlinear media, and its cell mirror design. Special interest has also been devoted to the investigation of few-cycle pulse compression at increased average powers and repetition rates, which so far has been achieved only in different stages of meter-long MPCs.

Therefore, in the first part of this thesis, it has been demonstrated that a compact configuration with a footprint of no more than 50 cm can be implemented to address this task. Pumped by a Yb-based laser system, initial tests at 1 kHz repetition rate and 250 mW average power showed broadened spectra supporting about 20 fs pulses in both krypton and xenon gas within a single-stage MPC with a total transmission exceeding 90%, which is characteristic of these setups. The rather narrow bandwidth coverage of the cell mirror design proved to be a critical limiting factor for SPM-induced spectral broadening.

In a further study, a different configuration based on the precise dispersion control inside a krypton-filled single-stage MPC has been introduced and initially tested at 1kHz repetition rate. Without altering the geometry of the previously used MPC, a new set of specially engineered cell mirrors was implemented, where the negative dispersion of these mirrors counteracts the positive dispersion accumulated during propagation through the gas. Initial results obtained by utilising only dispersion-engineered cell mirrors showed a remarkable improvement in nonlinear spectral broadening, resulting in spectra supporting 12 fs pulse durations. While in this case only half of the laser pulse energy can be sustained by this MPC configuration, reducing the overall negative dispersion introduced by the cell mirrors has shown to overcome this restriction without modifying the SPM-based broadening process. Furthermore, average power scalability up to 50 W and 200 kHz repetition rate has been demonstrated, where all the characteristics of the MPC output pulse have been maintained with excellent output beam properties.

Another important element is the generation of few-femtosecond UV pulses via resonant dispersive wave emission in a gas-filled hollow-core fibre. This technology offers a relatively simple and cost-effective solution for improving conversion efficiency in frequency upconversion and pulse energy up-scaling. Typically, implementing this requires short pulse durations of the driving beam, which is most often achieved using an initial gas-filled hollow-core fibre specifically intended for pulse compression, at the cost of transmission losses.

Therefore, efficient resonant dispersive wave emission driven by compressed pulses from an MPC setup has been demonstrated. First, the tunability range from 270 nm up to 530 nm at 1 kHz repetition rate via an argon-filled HCF has been achieved with UV pulse energies in the microjoule regime supporting few-cycle femtosecond pulses. In a subsequent test, average power and repetition rate scaling up to 13 W and 50 kHz, respectively, were accomplished while maintaining the UV pulse characteristics. Further scalability in average power and repetition rate was limited by thermal effects arising in the gas. Additionally, an overall beam path of the UV-pump and IR-probe setup has been conceptualised, including methods for adequately separating the RDW-emitted UV light from the soliton self-compressed IR to preserve the pulse characteristics of both types of radiation.

---

In conclusion, by combining a dispersion-engineered multi-pass cell with a resonant dispersive wave-based UV generation system, a compact and high-throughput tuneable UV source at high repetition rates is achieved. This approach is expected to overcome the temporal resolution and signal-to-noise ratio limitations of existing beamlines, enabling advancements in ultrafast time-resolved spectroscopy with tuneable wavelengths in the deep-UV region.



# Appendix

## Beam propagation using ABCD matrix

Following the description of nonlinear effects that dominate in the MPC-based pulse compression method, this section provides an explanation of light beam propagation through optical systems, including lenses, mirrors, and free space. The approach relies on the ray transfer matrix, or ABCD matrix, which can be applied both to geometrical rays and Gaussian beams. Note that this method requires the paraxial approximation  $\sin(\theta) \approx \theta$ , i.e., the beam divergence and angles are kept small for simplification and more precise calculations. The method described here is important to this work, as it has been used for the numerical simulation of beam propagation through the multi-pass cell setup.

When considering a laser beam as light ray, its propagation can be characterised by two parameters: the transverse offset  $r$  and the angular offset  $\theta$ , both offsets with respect to the optical axis. A linear relation between input and output ray is given by

$$\begin{bmatrix} r_2 \\ \theta_2 \end{bmatrix} = \begin{bmatrix} A & B \\ C & D \end{bmatrix} \begin{bmatrix} r_1 \\ \theta_1 \end{bmatrix} \quad (6.1)$$

where  $[r_1; \theta_1]$  and  $[r_2; \theta_2]$  represent input and output, respectively. The ray transfer matrix  $M := [A \ B; C \ D]$  is a 2x2 matrix containing the four elements A,B,C, and D, which represent specific characteristics of the optical system. In particular, the horizontal (spatial) and vertical (angular) magnification of a light beam are given by A and D, respectively, whereas the focusing and defocusing strength of the system are described by B and C, respectively.

For systems, which are composed of multiple optical elements, the final ABCD matrix is calculated via simple matrix multiplication of the matrices representing each section of the system. It should be noted, that the multiplication is performed in reverse order compared to the order of each element.

For instance, in the case of a system composed of four different optical elements the final matrix is calculated to be  $M_{1234} = M_4 M_3 M_2 M_1$ . Examples of basic matrices such as curved mirrors ( $M_{cm}$ ) and free space ( $M_{fs}$ ) are described as

$$M_{cm} = \begin{bmatrix} 1 & 0 \\ -\frac{2}{R} & 1 \end{bmatrix}, M_{fs} = \begin{bmatrix} 1 & d \\ 0 & 1 \end{bmatrix}. \quad (6.2)$$

In general, the determinant of the ABCD matrix is defined by the ratio between input refractive index and output refractive index. However, if the input and output are located in the same environment the determinant must always be 1, which is very common for optical systems. This makes the ABCD formalism a useful and rather simple tool for the design of resonator-like systems such as multi-pass cells, where free space propagation and focusing of the beam alternate over multiple passes.

As mentioned at the beginning, the ray transfer matrix is not only applied in geometrical optics, but also in the estimation of the effects imposed by optical elements on a Gaussian beam during propagation. Combining the matrix formalism with the complex  $q$ -parameter, as described for example in [108], the correlation between the output  $q_o$  and input parameter  $q_i$  reads as follows:

$$q_o = \frac{Aq_i + B}{Cq_i + D}. \quad (6.3)$$

From the complex representation of the  $q$ -parameter, as described in [109], the quantities related to the radius of curvature  $R$  and the beam spot size  $w$  at the output of the system can be calculated from equation 6.3, which is also beneficial for designing an MPC. A more detailed description and explanation of the ray transfer formalism is given e.g. in [108].

# Bibliography

- [1] L. Gallmann, C. Cirelli, and U. Keller. "Attosecond Science: Recent Highlights and Future Trends". In: *Annual Review of Physical Chemistry* 63. Volume 63, 2012 (May 2012), pp. 447–469. ISSN: 0066-426X, 1545-1593. DOI: [10.1146/annurev-physchem-032511-143702](https://doi.org/10.1146/annurev-physchem-032511-143702).
- [2] F. Calegari et al. "Advances in Attosecond Science". In: *Journal of Physics B: Atomic, Molecular and Optical Physics* 49.6 (Feb. 2016), p. 062001. ISSN: 0953-4075. DOI: [10.1088/0953-4075/49/6/062001](https://doi.org/10.1088/0953-4075/49/6/062001).
- [3] M. Chergui. "Ultrafast Molecular Photophysics in the Deep-Ultraviolet". In: *The Journal of Chemical Physics* 150.7 (Feb. 2019), p. 070901. ISSN: 0021-9606. DOI: [10.1063/1.5082644](https://doi.org/10.1063/1.5082644).
- [4] P. F. Moulton. "Spectroscopic and Laser Characteristics of Ti:Al<sub>2</sub>O<sub>3</sub>". In: *JOSA B* 3.1 (Jan. 1986), pp. 125–133. ISSN: 1520-8540. DOI: [10.1364/JOSAB.3.000125](https://doi.org/10.1364/JOSAB.3.000125).
- [5] S. Rausch et al. "Controlled Waveforms on the Single-Cycle Scale from a Femtosecond Oscillator". In: *Optics Express* 16.13 (June 2008), pp. 9739–9745. ISSN: 1094-4087. DOI: [10.1364/OE.16.009739](https://doi.org/10.1364/OE.16.009739).
- [6] M. Müller et al. "3.5 kW Coherently Combined Ultrafast Fiber Laser". In: *Optics Letters* 43.24 (Dec. 2018), pp. 6037–6040. ISSN: 1539-4794. DOI: [10.1364/OL.43.006037](https://doi.org/10.1364/OL.43.006037).
- [7] S. Chénais et al. "On Thermal Effects in Solid-State Lasers: The Case of Ytterbium-Doped Materials". In: *Progress in Quantum Electronics* 30.4 (Jan. 2006), pp. 89–153. ISSN: 0079-6727. DOI: [10.1016/j.pquantelec.2006.12.001](https://doi.org/10.1016/j.pquantelec.2006.12.001).
- [8] A. S. Kurkov. "Oscillation Spectral Range of Yb-doped Fiber Lasers". In: *Laser Physics Letters* 4.2 (2007), pp. 93–102. ISSN: 1612-202X. DOI: [10.1002/lap1.200610094](https://doi.org/10.1002/lap1.200610094).
- [9] M. Nisoli, S. De Silvestri, and O. Svelto. "Generation of High Energy 10 Fs Pulses by a New Pulse Compression Technique". In: *Applied Physics Letters* 68.20 (May 1996), pp. 2793–2795. ISSN: 0003-6951. DOI: [10.1063/1.116609](https://doi.org/10.1063/1.116609).

- [10] Y.-G. Jeong et al. "Direct Compression of 170-Fs 50-Cycle Pulses down to 1.5 Cycles with 70% Transmission". In: *Scientific Reports* 8.1 (Aug. 2018), p. 11794. ISSN: 2045-2322. DOI: [10.1038/s41598-018-30198-y](https://doi.org/10.1038/s41598-018-30198-y).
- [11] T. Nagy et al. "Generation of Three-Cycle Multi-Millijoule Laser Pulses at 318 W Average Power". In: *Optica* 6.11 (Nov. 2019), pp. 1423–1424. ISSN: 2334-2536. DOI: [10.1364/OPTICA.6.001423](https://doi.org/10.1364/OPTICA.6.001423).
- [12] M. Hanna et al. "Nonlinear Optics in Multipass Cells". In: *Laser and Photonics Reviews* 15.12 (Oct. 2021), p. 2100220. DOI: [10.1002/lpor.202100220](https://doi.org/10.1002/lpor.202100220).
- [13] A.-L. Viotti et al. "Multi-Pass Cells for Post-Compression of Ultrashort Laser Pulses". In: *Optica* 9.2 (Feb. 2022), pp. 197–216. ISSN: 2334-2536. DOI: [10.1364/OPTICA.449225](https://doi.org/10.1364/OPTICA.449225).
- [14] P. Balla et al. "Postcompression of Picosecond Pulses into the Few-Cycle Regime". In: *Optics Letters* 45.9 (May 2020), pp. 2572–2575. ISSN: 1539-4794. DOI: [10.1364/OL.388665](https://doi.org/10.1364/OL.388665).
- [15] M. Galli et al. "Generation of Deep Ultraviolet Sub-2-Fs Pulses". In: *Optics Letters* 44.6 (Mar. 2019), pp. 1308–1311. ISSN: 1539-4794. DOI: [10.1364/OL.44.001308](https://doi.org/10.1364/OL.44.001308).
- [16] J. C. Travers et al. "High-Energy Pulse Self-Compression and Ultraviolet Generation through Soliton Dynamics in Hollow Capillary Fibres". In: *Nature Photonics* 13.8 (Aug. 2019), pp. 547–554. ISSN: 1749-4893. DOI: [10.1038/s41566-019-0416-4](https://doi.org/10.1038/s41566-019-0416-4).
- [17] P. Agostini and L. F. DiMauro. "The Physics of Attosecond Light Pulses". In: *Reports on Progress in Physics* 67.6 (June 2004), pp. 813–855. ISSN: 0034-4885, 1361-6633. DOI: [10.1088/0034-4885/67/6/R01](https://doi.org/10.1088/0034-4885/67/6/R01).
- [18] R. W. Boyd. *Nonlinear Optics*. Third Edition. Academic Press, 2008.
- [19] P. E. Powers and J. W. Haus. *Fundamentals of Nonlinear Optics*. Second edition. Boca Raton: CRC Press, Taylor & Francis Group, 2017. ISBN: 978-1-4987-3683-1.
- [20] A. M. Weiner. *Ultrafast Optics*. Wiley Series in Pure and Applied Optics, Wiley, 2008.
- [21] J. C. Maxwell. "VIII. A Dynamical Theory of the Electromagnetic Field". In: *Philosophical Transactions of the Royal Society of London* 155 (Jan. 1997), pp. 459–512. DOI: [10.1098/rstl.1865.0008](https://doi.org/10.1098/rstl.1865.0008).

- [22] E. Grace et al. "Index of Refraction, Rayleigh Scattering Length, and Sellmeier Coefficients in Solid and Liquid Argon and Xenon". In: *Nuclear Instruments and Methods in Physics Research Section A: Accelerators, Spectrometers, Detectors and Associated Equipment* 867 (Sept. 2017), pp. 204–208. ISSN: 0168-9002. DOI: [10.1016/j.nima.2017.06.031](https://doi.org/10.1016/j.nima.2017.06.031).
- [23] M. N. Polyanskiy. *Refractive Index Database*. <https://refractiveindex.info>. (Visited on 11/05/2023).
- [24] M. Moreno. *Kerr Effect*. <https://www.accessscience.com/content/article/a363500>. 2018. (Visited on 12/01/2024).
- [25] C. Brée, A. Demircan, and G. Steinmeyer. "Method for Computing the Nonlinear Refractive Index via Keldysh Theory". In: *Quantum Electronics, IEEE Journal of* 46 (May 2010), pp. 433–437. DOI: [10.1109/JQE.2009.2031599](https://doi.org/10.1109/JQE.2009.2031599).
- [26] T. Nagy, P. Simon, and L. Veisz. "High-Energy Few-Cycle Pulses: Post-Compression Techniques". In: *Advances in Physics: X* 6.1 (Jan. 2021), p. 1845795. ISSN: 2374-6149. DOI: [10.1080/23746149.2020.1845795](https://doi.org/10.1080/23746149.2020.1845795).
- [27] G. Fibich and A. L. Gaeta. "Critical Power for Self-Focusing in Bulk Media and in Hollow Waveguides". In: *Optics Letters* 25.5 (Mar. 2000), pp. 335–337. ISSN: 1539-4794. DOI: [10.1364/OL.25.000335](https://doi.org/10.1364/OL.25.000335).
- [28] R. L. Fork, O. E. Martinez, and J. P. Gordon. "Negative Dispersion Using Pairs of Prisms". In: *Optics Letters* 9.5 (May 1984), pp. 150–152. ISSN: 1539-4794. DOI: [10.1364/OL.9.000150](https://doi.org/10.1364/OL.9.000150).
- [29] E. Treacy. "Optical Pulse Compression with Diffraction Gratings". In: *IEEE Journal of Quantum Electronics* 5.9 (Sept. 1969), pp. 454–458. ISSN: 1558-1713. DOI: [10.1109/JQE.1969.1076303](https://doi.org/10.1109/JQE.1969.1076303).
- [30] C. Rolland and P. B. Corkum. "Compression of High-Power Optical Pulses". In: *JOSA B* 5.3 (Mar. 1988), pp. 641–647. ISSN: 1520-8540. DOI: [10.1364/JOSAB.5.000641](https://doi.org/10.1364/JOSAB.5.000641).
- [31] N. Milosevic, G. Tempea, and T. Brabec. "Optical Pulse Compression: Bulk Media versus Hollow Waveguides". In: *Optics Letters* 25.9 (May 2000), pp. 672–674. ISSN: 1539-4794. DOI: [10.1364/OL.25.000672](https://doi.org/10.1364/OL.25.000672).
- [32] C.-H. Lu et al. "Generation of Intense Supercontinuum in Condensed Media". In: *Optica* 1.6 (Dec. 2014), p. 400. ISSN: 2334-2536. DOI: [10.1364/OPTICA.1.000400](https://doi.org/10.1364/OPTICA.1.000400).

- [33] Y.-C. Cheng et al. "Supercontinuum Generation in a Multi-Plate Medium". In: *Optics Express* 24.7 (Apr. 2016), pp. 7224–7231. ISSN: 1094-4087. DOI: [10.1364/OE.24.007224](https://doi.org/10.1364/OE.24.007224).
- [34] P. He et al. "High-Efficiency Supercontinuum Generation in Solid Thin Plates at 0.1 TW Level". In: *Optics Letters* 42.3 (Feb. 2017), pp. 474–477. ISSN: 1539-4794. DOI: [10.1364/OL.42.000474](https://doi.org/10.1364/OL.42.000474).
- [35] C.-H. Lu et al. "Greater than 50 Times Compression of 1030 Nm Yb:KGW Laser Pulses to Single-Cycle Duration". In: *Optics Express* 27.11 (May 2019), pp. 15638–15648. ISSN: 1094-4087. DOI: [10.1364/OE.27.015638](https://doi.org/10.1364/OE.27.015638).
- [36] C.-H. Lu et al. "Sub-4 Fs Laser Pulses at High Average Power and High Repetition Rate from an All-Solid-State Setup". In: *Optics Express* 26.7 (Apr. 2018), pp. 8941–8956. ISSN: 1094-4087. DOI: [10.1364/OE.26.008941](https://doi.org/10.1364/OE.26.008941).
- [37] C. Jocher et al. "Sub 25 Fs Pulses from Solid-Core Nonlinear Compression Stage at 250 W of Average Power". In: *Optics Letters* 37.21 (Nov. 2012), pp. 4407–4409. ISSN: 1539-4794. DOI: [10.1364/OL.37.004407](https://doi.org/10.1364/OL.37.004407).
- [38] A. V. Smith et al. "Optical Damage Limits to Pulse Energy From Fibers". In: *IEEE Journal of Selected Topics in Quantum Electronics* 15.1 (Jan. 2009), pp. 153–158. ISSN: 1558-4542. DOI: [10.1109/JSTQE.2008.2010331](https://doi.org/10.1109/JSTQE.2008.2010331).
- [39] M. Nisoli et al. "Compression of High-Energy Laser Pulses below 5 Fs". In: *Optics Letters* 22.8 (Apr. 1997), pp. 522–524. ISSN: 1539-4794. DOI: [10.1364/OL.22.000522](https://doi.org/10.1364/OL.22.000522).
- [40] J. Park, J.-H. Lee, and C. H. Nam. "Generation of 1.5 Cycle 0.3 TW Laser Pulses Using a Hollow-Fiber Pulse Compressor". In: *Optics Letters* 34.15 (Aug. 2009), pp. 2342–2344. ISSN: 1539-4794. DOI: [10.1364/OL.34.002342](https://doi.org/10.1364/OL.34.002342).
- [41] G. Fan et al. "70 mJ Nonlinear Compression and Scaling Route for an Yb Amplifier Using Large-Core Hollow Fibers". In: *Optics Letters* 46.4 (Feb. 2021), pp. 896–899. ISSN: 1539-4794. DOI: [10.1364/OL.412296](https://doi.org/10.1364/OL.412296).
- [42] J. Schulte et al. "Nonlinear Pulse Compression in a Multi-Pass Cell". In: *Optics Letters* 41.19 (Oct. 2016), pp. 4511–4514. ISSN: 1539-4794. DOI: [10.1364/OL.41.004511](https://doi.org/10.1364/OL.41.004511).
- [43] J. Weitenberg et al. "Multi-Pass-Cell-Based Nonlinear Pulse Compression to 115 Fs at 7.5  $\mu$ J Pulse Energy and 300 W Average Power". In: *Optics Express* 25.17 (Aug. 2017), pp. 20502–20510. ISSN: 1094-4087. DOI: [10.1364/OE.25.020502](https://doi.org/10.1364/OE.25.020502).

- [44] J. Weitenberg et al. "Nonlinear Pulse Compression to Sub-40 Fs at 4.5  $\mu$ J Pulse Energy by Multi-Pass-Cell Spectral Broadening". In: *IEEE Journal of Quantum Electronics* 53.6 (Dec. 2017), pp. 1–4. ISSN: 1558-1713. DOI: [10.1109/JQE.2017.2761883](https://doi.org/10.1109/JQE.2017.2761883).
- [45] K. Fritsch et al. "All-Solid-State Multipass Spectral Broadening to Sub-20 Fs". In: *Optics Letters* 43.19 (Oct. 2018), pp. 4643–4646. ISSN: 1539-4794. DOI: [10.1364/OL.43.004643](https://doi.org/10.1364/OL.43.004643).
- [46] G. Jargot et al. "Self-Compression in a Multipass Cell". In: *Optics Letters* 43.22 (Nov. 2018), pp. 5643–5646. ISSN: 1539-4794. DOI: [10.1364/OL.43.005643](https://doi.org/10.1364/OL.43.005643).
- [47] A. B. Wahid et al. "Supercontinuum Generation in a Nitrogen Filled Multipass Cell". In: *2021 Conference on Lasers and Electro-Optics Europe & European Quantum Electronics Conference (CLEO/Europe-EQEC)*. June 2021, pp. 1–1. DOI: [10.1109/CLEO/Europe-EQEC52157.2021.9542058](https://doi.org/10.1109/CLEO/Europe-EQEC52157.2021.9542058).
- [48] M. Hanna et al. "Nonlinear Temporal Compression in Multipass Cells: Theory". In: *JOSA B* 34.7 (July 2017), pp. 1340–1347. ISSN: 1520-8540. DOI: [10.1364/JOSAB.34.001340](https://doi.org/10.1364/JOSAB.34.001340).
- [49] M. Kaumanns et al. "Spectral Broadening of 112 mJ, 1.3 Ps Pulses at 5 kHz in a LG<sub>10</sub> Multipass Cell with Compressibility to 37 Fs". In: *Optics Letters* 46.5 (Mar. 2021), pp. 929–932. ISSN: 1539-4794. DOI: [10.1364/OL.416734](https://doi.org/10.1364/OL.416734).
- [50] Y. Pfaff et al. "Nonlinear Pulse Compression of a 200 mJ and 1 kW Ultrafast Thin-Disk Amplifier". In: *Optics Express* 31.14 (July 2023), pp. 22740–22756. ISSN: 1094-4087. DOI: [10.1364/OE.494359](https://doi.org/10.1364/OE.494359).
- [51] D. Herriott, H. Kogelnik, and R. Kompfner. "Off-Axis Paths in Spherical Mirror Interferometers". In: *Applied Optics* 3.4 (Apr. 1964), pp. 523–526. ISSN: 2155-3165. DOI: [10.1364/AO.3.000523](https://doi.org/10.1364/AO.3.000523).
- [52] M. Hanna et al. "Nonlinear Beam Matching to Gas-Filled Multipass Cells". In: *OSA Continuum* 4.2 (Feb. 2021), pp. 732–738. ISSN: 2578-7519. DOI: [10.1364/OSAC.418247](https://doi.org/10.1364/OSAC.418247).
- [53] N. Daher et al. "Multipass Cells: 1D Numerical Model and Investigation of Spatio-Spectral Couplings at High Nonlinearity". In: *JOSA B* 37.4 (Apr. 2020), pp. 993–999. ISSN: 1520-8540. DOI: [10.1364/JOSAB.386049](https://doi.org/10.1364/JOSAB.386049).

- [54] F. Meyer et al. "Milliwatt-Class Broadband THz Source Driven by a 112 W, Sub-100 Fs Thin-Disk Laser". In: *Optics Express* 27.21 (Oct. 2019), pp. 30340–30349. ISSN: 1094-4087. DOI: [10.1364/OE.27.030340](https://doi.org/10.1364/OE.27.030340).
- [55] F. Meyer et al. "Single-Cycle, MHz Repetition Rate THz Source with 66 mW of Average Power". In: *Optics Letters* 45.9 (May 2020), pp. 2494–2497. ISSN: 1539-4794. DOI: [10.1364/OL.386305](https://doi.org/10.1364/OL.386305).
- [56] L. Lavenu et al. "Nonlinear Pulse Compression Based on a Gas-Filled Multipass Cell". In: *Optics Letters* 43.10 (May 2018), pp. 2252–2255. ISSN: 1539-4794. DOI: [10.1364/OL.43.002252](https://doi.org/10.1364/OL.43.002252).
- [57] M. Ueffing et al. "Nonlinear Pulse Compression in a Gas-Filled Multipass Cell". In: *Optics Letters* 43.9 (May 2018), pp. 2070–2073. ISSN: 1539-4794. DOI: [10.1364/OL.43.002070](https://doi.org/10.1364/OL.43.002070).
- [58] P. Russbuedt et al. "Scalable 30 Fs Laser Source with 530 W Average Power". In: *Optics Letters* 44.21 (Nov. 2019), pp. 5222–5225. ISSN: 1539-4794. DOI: [10.1364/OL.44.005222](https://doi.org/10.1364/OL.44.005222).
- [59] A.-L. Viotti et al. "60 Fs, 1030 Nm FEL Pump–Probe Laser Based on a Multi-Pass Post-Compressed Yb:YAG Source". In: *Journal of Synchrotron Radiation* 28.1 (Jan. 2021), pp. 36–43. ISSN: 1600-5775. DOI: [10.1107/S1600577520015052](https://doi.org/10.1107/S1600577520015052).
- [60] Y. Pfaff et al. "Nonlinear Pulse Compression of a Thin-Disk Amplifier and Contrast Enhancement via Nonlinear Ellipse Rotation". In: *Optics Express* 30.7 (Mar. 2022), pp. 10981–10990. ISSN: 1094-4087. DOI: [10.1364/OE.455393](https://doi.org/10.1364/OE.455393).
- [61] M. Kaumanns et al. "Multipass Spectral Broadening of 18 mJ Pulses Compressible from 1.3 Ps to 41 Fs". In: *Optics Letters* 43.23 (Dec. 2018), pp. 5877–5880. ISSN: 1539-4794. DOI: [10.1364/OL.43.005877](https://doi.org/10.1364/OL.43.005877).
- [62] P. L. Kramer et al. "Enabling High Repetition Rate Nonlinear THz Science with a Kilowatt-Class Sub-100 Fs Laser Source". In: *Optics Express* 28.11 (May 2020), pp. 16951–16967. ISSN: 1094-4087. DOI: [10.1364/OE.389653](https://doi.org/10.1364/OE.389653).
- [63] C. Grebing et al. "Kilowatt-Average-Power Compression of Millijoule Pulses in a Gas-Filled Multi-Pass Cell". In: *Optics Letters* 45.22 (Nov. 2020), pp. 6250–6253. ISSN: 1539-4794. DOI: [10.1364/OL.408998](https://doi.org/10.1364/OL.408998).
- [64] L. Lavenu et al. "High-Power Two-Cycle Ultrafast Source Based on Hybrid Nonlinear Compression". In: *Optics Express* 27.3 (Feb. 2019), pp. 1958–1967. ISSN: 1094-4087. DOI: [10.1364/OE.27.001958](https://doi.org/10.1364/OE.27.001958).

- [65] E. Vicentini et al. “Nonlinear Pulse Compression to 22 Fs at 15.6  $\mu$ J by an All-Solid-State Multipass Approach”. In: *Optics Express* 28.4 (Feb. 2020), pp. 4541–4549. ISSN: 1094-4087. DOI: [10.1364/OE.385583](https://doi.org/10.1364/OE.385583).
- [66] M. Müller et al. “Multipass Cell for High-Power Few-Cycle Compression”. In: *Optics Letters* 46.11 (June 2021), pp. 2678–2681. ISSN: 1539-4794. DOI: [10.1364/OL.425872](https://doi.org/10.1364/OL.425872).
- [67] S. Rajhans et al. “Post-Compression of Multi-Millijoule Picosecond Pulses to Few-Cycles Approaching the Terawatt Regime”. In: *Optics Letters* 48.18 (Sept. 2023), pp. 4753–4756. ISSN: 1539-4794. DOI: [10.1364/OL.498042](https://doi.org/10.1364/OL.498042).
- [68] C.-L. Tsai et al. “Efficient Nonlinear Compression of a Mode-Locked Thin-Disk Oscillator to 27 Fs at 98 W Average Power”. In: *Optics Letters* 44.17 (Sept. 2019), pp. 4115–4118. ISSN: 1539-4794. DOI: [10.1364/OL.44.004115](https://doi.org/10.1364/OL.44.004115).
- [69] G. Barbiero et al. “Efficient Nonlinear Compression of a Thin-Disk Oscillator to 8.5 Fs at 55 W Average Power”. In: *Optics Letters* 46.21 (Nov. 2021), pp. 5304–5307. ISSN: 1539-4794. DOI: [10.1364/OL.440303](https://doi.org/10.1364/OL.440303).
- [70] S. Goncharov, K. Fritsch, and O. Pronin. “Few-Cycle Pulse Compression and White Light Generation in Cascaded Multipass Cells”. In: *Optics Letters* 48.1 (Jan. 2023), pp. 147–150. ISSN: 1539-4794. DOI: [10.1364/OL.479248](https://doi.org/10.1364/OL.479248).
- [71] V. Hariton et al. “Spectral Broadening in Convex-Concave Multipass Cells”. In: *Optics Express* 31.12 (June 2023), pp. 19554–19568. ISSN: 1094-4087. DOI: [10.1364/OE.486797](https://doi.org/10.1364/OE.486797).
- [72] C. M. Heyl et al. “High-Energy Bow Tie Multi-Pass Cells for Nonlinear Spectral Broadening Applications”. In: *Journal of Physics: Photonics* 4.1 (Jan. 2022), p. 014002. ISSN: 2515-7647. DOI: [10.1088/2515-7647/ac483a](https://doi.org/10.1088/2515-7647/ac483a).
- [73] T. Saule et al. “High-Flux Ultrafast Extreme-Ultraviolet Photoemission Spectroscopy at 18.4 MHz Pulse Repetition Rate”. In: *Nature Communications* 10.1 (Jan. 2019), p. 458. ISSN: 2041-1723. DOI: [10.1038/s41467-019-08367-y](https://doi.org/10.1038/s41467-019-08367-y).
- [74] V. C. Kuriakose and K. Porsezian. “Elements of Optical Solitons: An Overview”. In: *Resonance* 15.7 (July 2010), pp. 643–666. ISSN: 0971-8044, 0973-712X. DOI: [10.1007/s12045-010-0048-y](https://doi.org/10.1007/s12045-010-0048-y).

- [75] J. Limpert et al. "All Fiber Chirped-Pulse Amplification System Based on Compression in Air-Guiding Photonic Bandgap Fiber". In: *Optics Express* 11.24 (Dec. 2003), pp. 3332–3337. ISSN: 1094-4087. DOI: [10.1364/OE.11.003332](https://doi.org/10.1364/OE.11.003332).
- [76] D. G. Ouzounov et al. "Soliton Pulse Compression in Photonic Band-Gap Fibers." In: *Optics Express* 13.16 (Aug. 2005), pp. 6153–6159. ISSN: 1094-4087. DOI: [10.1364/OPEX.13.006153](https://doi.org/10.1364/OPEX.13.006153).
- [77] A. Suda et al. "Generation of Sub-10-Fs, 5-mJ-optical Pulses Using a Hollow Fiber with a Pressure Gradient". In: *Applied Physics Letters* 86.11 (Mar. 2005), p. 111116. ISSN: 0003-6951. DOI: [10.1063/1.1883706](https://doi.org/10.1063/1.1883706).
- [78] K. F. Mak et al. "Compressing  $\mu$ J-level Pulses from 250 Fs to Sub-10 Fs at 38-MHz Repetition Rate Using Two Gas-Filled Hollow-Core Photonic Crystal Fiber Stages". In: *Optics Letters* 40.7 (Apr. 2015), pp. 1238–1241. ISSN: 1539-4794. DOI: [10.1364/OL.40.001238](https://doi.org/10.1364/OL.40.001238).
- [79] E. Escoto et al. "Temporal Quality of Post-Compressed Pulses at Large Compression Factors". In: *JOSA B* 39.7 (July 2022), pp. 1694–1702. ISSN: 1520-8540. DOI: [10.1364/JOSAB.453901](https://doi.org/10.1364/JOSAB.453901).
- [80] D. Grischkowsky and A. C. Balant. "Optical Pulse Compression Based on Enhanced Frequency Chirping". In: *Applied Physics Letters* 41.1 (July 1982), pp. 1–3. ISSN: 0003-6951. DOI: [10.1063/1.93306](https://doi.org/10.1063/1.93306).
- [81] S. Gröbmeyer et al. "Self-Compression at 1 Mm Wavelength in All-Bulk Multi-Pass Geometry". In: *Applied Physics B* 126.10 (Sept. 2020), p. 159. ISSN: 1432-0649. DOI: [10.1007/s00340-020-07506-4](https://doi.org/10.1007/s00340-020-07506-4).
- [82] R. Safaei et al. "High-Energy Multidimensional Solitary States in Hollow-Core Fibres". In: *Nature Photonics* 14.12 (Dec. 2020), pp. 733–739. ISSN: 1749-4893. DOI: [10.1038/s41566-020-00699-2](https://doi.org/10.1038/s41566-020-00699-2).
- [83] P. Balla et al. "Ultrafast Serrodyne Optical Frequency Translator". In: *Nature Photonics* 17.2 (Feb. 2023), pp. 187–192. ISSN: 1749-4893. DOI: [10.1038/s41566-022-01121-9](https://doi.org/10.1038/s41566-022-01121-9).
- [84] F. Benabid et al. "Stimulated Raman Scattering in Hydrogen-Filled Hollow-Core Photonic Crystal Fiber". In: *Science* 298.5592 (Oct. 2002), pp. 399–402. DOI: [10.1126/science.1076408](https://doi.org/10.1126/science.1076408).
- [85] C. G. Durfee et al. "Ultrabroadband Phase-Matched Optical Parametric Generation in the Ultraviolet by Use of Guided Waves". In: *Optics Letters* 22.20 (Oct. 1997), pp. 1565–1567. ISSN: 1539-4794. DOI: [10.1364/OL.22.001565](https://doi.org/10.1364/OL.22.001565).

- [86] C. G. Durfee et al. "Phase Matching of High-Order Harmonics in Hollow Waveguides". In: *Physical Review Letters* 83.11 (Sept. 1999), pp. 2187–2190. DOI: [10.1103/PhysRevLett.83.2187](https://doi.org/10.1103/PhysRevLett.83.2187).
- [87] F. Wiegandt et al. "Quasi-Phase-Matched High-Harmonic Generation in Gas-Filled Hollow-Core Photonic Crystal Fiber". In: *Optica* 6.4 (Apr. 2019), pp. 442–447. ISSN: 2334-2536. DOI: [10.1364/OPTICA.6.000442](https://doi.org/10.1364/OPTICA.6.000442).
- [88] P. N. Anderson et al. "High-Energy Laser-Pulse Self-Compression in Short Gas-Filled Fibers". In: *Physical Review A* 89.1 (Jan. 2014), p. 013819. DOI: [10.1103/PhysRevA.89.013819](https://doi.org/10.1103/PhysRevA.89.013819).
- [89] M. Nisoli et al. "Toward a Terawatt-Scale Sub-10-Fs Laser Technology". In: *IEEE Journal of Selected Topics in Quantum Electronics* 4.2 (March-April/1998), pp. 414–420. ISSN: 1077260X. DOI: [10.1109/2944.686749](https://doi.org/10.1109/2944.686749).
- [90] N. Y. Joly et al. "Bright Spatially Coherent Wavelength-Tunable Deep-UV Laser Source Using an Ar-Filled Photonic Crystal Fiber". In: *Physical Review Letters* 106.20 (May 2011), p. 203901. DOI: [10.1103/PhysRevLett.106.203901](https://doi.org/10.1103/PhysRevLett.106.203901).
- [91] J. C. Travers et al. "Ultrafast Nonlinear Optics in Gas-Filled Hollow-Core Photonic Crystal Fibers [Invited]". In: *JOSA B* 28.12 (Dec. 2011), A11–A26. ISSN: 1520-8540. DOI: [10.1364/JOSAB.28.000A11](https://doi.org/10.1364/JOSAB.28.000A11).
- [92] P. St J. Russell et al. "Hollow-Core Photonic Crystal Fibres for Gas-Based Nonlinear Optics". In: *Nature Photonics* 8.4 (Apr. 2014), pp. 278–286. ISSN: 1749-4893. DOI: [10.1038/nphoton.2013.312](https://doi.org/10.1038/nphoton.2013.312).
- [93] F. Köttig et al. "Generation of Microjoule Pulses in the Deep Ultraviolet at Megahertz Repetition Rates". In: *Optica* 4.10 (Oct. 2017), pp. 1272–1276. ISSN: 2334-2536. DOI: [10.1364/OPTICA.4.001272](https://doi.org/10.1364/OPTICA.4.001272).
- [94] A. Ermolov et al. "Supercontinuum Generation in the Vacuum Ultraviolet through Dispersive-Wave and Soliton-Plasma Interaction in a Noble-Gas-Filled Hollow-Core Photonic Crystal Fiber". In: *Physical Review A* 92.3 (Sept. 2015), p. 033821. DOI: [10.1103/PhysRevA.92.033821](https://doi.org/10.1103/PhysRevA.92.033821).
- [95] T. Nagy, M. Forster, and P. Simon. "Flexible Hollow Fiber for Pulse Compressors". In: *Applied Optics* 47.18 (June 2008), pp. 3264–3268. ISSN: 2155-3165. DOI: [10.1364/AO.47.003264](https://doi.org/10.1364/AO.47.003264).

- [96] C. Brahms and J. C. Travers. “Efficient and Compact Source of Tuneable Ultrafast Deep Ultraviolet Laser Pulses at 50 kHz Repetition Rate”. In: *Optics Letters* 48.1 (Jan. 2023), pp. 151–154. ISSN: 1539-4794. DOI: [10.1364/OL.480103](https://doi.org/10.1364/OL.480103).
- [97] G. P. Agrawal. *Nonlinear Fiber Optics*. 3rd ed. Academic Press, 2001.
- [98] L. F. Mollenauer, R. H. Stolen, and J. P. Gordon. “Experimental Observation of Picosecond Pulse Narrowing and Solitons in Optical Fibers”. In: *Physical Review Letters* 45.13 (Sept. 1980), pp. 1095–1098. DOI: [10.1103/PhysRevLett.45.1095](https://doi.org/10.1103/PhysRevLett.45.1095).
- [99] A. V. Husakou and J. Herrmann. “Supercontinuum Generation of Higher-Order Solitons by Fission in Photonic Crystal Fibers”. In: *Physical Review Letters* 87.20 (Oct. 2001), p. 203901. DOI: [10.1103/PhysRevLett.87.203901](https://doi.org/10.1103/PhysRevLett.87.203901).
- [100] J. M. Dudley, G. Genty, and S. Coen. “Supercontinuum Generation in Photonic Crystal Fiber”. In: *Reviews of Modern Physics* 78.4 (Oct. 2006), pp. 1135–1184. DOI: [10.1103/RevModPhys.78.1135](https://doi.org/10.1103/RevModPhys.78.1135).
- [101] C. M. Chen and P. L. Kelley. “Nonlinear Pulse Compression in Optical Fibers: Scaling Laws and Numerical Analysis”. In: *JOSA B* 19.9 (Sept. 2002), pp. 1961–1967. ISSN: 1520-8540. DOI: [10.1364/JOSAB.19.001961](https://doi.org/10.1364/JOSAB.19.001961).
- [102] N. Akhmediev and M. Karlsson. “Cherenkov Radiation Emitted by Solitons in Optical Fibers”. In: *Physical Review A* 51.3 (Mar. 1995), pp. 2602–2607. DOI: [10.1103/PhysRevA.51.2602](https://doi.org/10.1103/PhysRevA.51.2602).
- [103] C. Brahms, F. Belli, and J. C. Travers. “Resonant Dispersive Wave Emission in Hollow Capillary Fibers Filled with Pressure Gradients”. In: *Optics Letters* 45.16 (Aug. 2020), pp. 4456–4459. ISSN: 1539-4794. DOI: [10.1364/OL.398343](https://doi.org/10.1364/OL.398343).
- [104] J. C. Travers. “Optical Solitons in Hollow-Core Fibres”. In: *Optics Communications* 555 (Mar. 2024), p. 130191. ISSN: 0030-4018. DOI: [10.1016/j.optcom.2023.130191](https://doi.org/10.1016/j.optcom.2023.130191).
- [105] T. Gebert et al. “Michelson-Type All-Reflective Interferometric Autocorrelation in the VUV Regime”. In: *New Journal of Physics* 16.7 (July 2014), p. 073047. ISSN: 1367-2630. DOI: [10.1088/1367-2630/16/7/073047](https://doi.org/10.1088/1367-2630/16/7/073047).

- 
- [106] F. Reiter et al. "Generation of Sub-3 Fs Pulses in the Deep Ultraviolet". In: *Optics Letters* 35.13 (July 2010), pp. 2248–2250. ISSN: 1539-4794. DOI: [10.1364/OL.35.002248](https://doi.org/10.1364/OL.35.002248).
- [107] T. F. Grigorova. "Scaling of Soliton Dynamics in Gas-Filled Hollow Capillary Fibres". Doctoral Thesis. Heriot-Watt University Edinburgh, 2022.
- [108] H. Kogelnik and T. Li. "Laser Beams and Resonators". In: *Applied Optics* 5.10 (Oct. 1966), pp. 1550–1567. ISSN: 2155-3165. DOI: [10.1364/AO.5.001550](https://doi.org/10.1364/AO.5.001550).
- [109] S. Mookherjea and A. Yariv. "Analysis of Optical Pulse Propagation with ABCD Matrices". In: *Physical Review E* 64.1 (June 2001). Comment: 10 pages, 2 figures, submitted to PRE (01/01), p. 016611. ISSN: 1063-651X, 1095-3787. DOI: [10.1103/PhysRevE.64.016611](https://doi.org/10.1103/PhysRevE.64.016611). arXiv: [physics/0103011](https://arxiv.org/abs/physics/0103011).



# Publications and Conferences

## Journal articles

- 1. A 50-kHz few-fs RDW-based UV light source efficiently driven by a dispersion-engineered multipass cell.**  
L. Silletti, A. b. Wahid, T. F. Grigorova, L. Pratolli, A. Ferreira de Oliveira e Silva, C. Brahms, V. Wanie, A. Trabattoni, C. M. Heyl, J. C. Travers and F. Calegari  
*Manuscript in preparation*
- 2. Time-resolving state-specific molecular dissociation with XUV broadband absorption spectroscopy.**  
A. Magunia, M. Rebholz, E. Appi, C. C. Papadopoulou, H. Lindenblatt, F. Trost, S. Meister, T. Ding, M. Straub, G. D. Borisova, J. Lee, R. Jin, A. v. d. Dellen, C. Kaiser, M. Braune, S. Düsterer, S. Ališauskas, T. Lang, C. M. Heyl, B. Manschwetus, S. Grunewald, U. Frühling, A. Tajalli, A. b. Wahid, L. Silletti, F. Calegari, P. Mosel, U. Morgner, M. Kovacev, U. Thumm, I. Hartl, R. Treusch, R. Moshhammer, C. Ott, T. Pfeifer  
*Science Advances* 9(47), eadk148 (2023), DOI: [10.1126/sciadv.adk1482](https://doi.org/10.1126/sciadv.adk1482)
- 3. A dispersion-engineered multi-pass cell for single-stage post compression of an Ytterbium laser.**  
L. Silletti, A. b. Wahid, P. Balla, E. Escoto, S. Rajhans, K. Horn, L. Winkelmann, V. Wanie, A. Trabattoni, C. M. Heyl and F. Calegari  
*Optics Letters* 48(7), 1842-1845 (2023), DOI: [10.1364/OL.476846](https://doi.org/10.1364/OL.476846)
- 4. Post-compression into few-cycle regime via dual-stage MPC.**  
P. Balla, A. b. Wahid, I. Sytceвич, C. Guo, A.-L. Viotti, L. Silletti, A. Cartella, S. Alisauskas, H. Tavakol, U. Grosse-Wortmann, A. Schönberg, M. Seidel, A. Trabattoni, B. Manschwetus, T. Lang, F. Calegari, A. Couairon, A. L'Huillier, C. L. Arnold, I. Hartl and C. M. Heyl  
*Optics Letters* 45(9), 2572-2575 (2020), DOI: [10.1364/OL.388665](https://doi.org/10.1364/OL.388665)

## Conference presentations

1. **A single-stage dispersion-controlled multi-pass cell setup to efficiently drive resonant dispersive wave emission**

L. Silletti, T. F. Grigorova, C. Brahms, A. b. Wahid, E. Escoto, P. Balla, S. Rajhans, K. Horn, L. Winkelmann, V. Wanie, A. Trabattoni, C. M. Heyl, J. C. Travers and F. Calegari  
CLEO/Europe – EQEC 2023, Munich (2023) - Oral presentation

2. **High-repetition rate UV pump-probe beamline for high-statistics spectroscopy at the few-femtosecond timescale**

L. Silletti, A. b. Wahid, P. Balla, E. Escoto, K. Horn, L. Winkelmann, V. Wanie, A. Trabattoni, C. M. Heyl and F. Calegari  
23<sup>rd</sup> European Conference on the Dynamics of Molecular Systems (MOLEC 2022), Hamburg (2022) - Poster

3. **Sub-20 fs post-compression of an Ytterbium fiber laser in a single-stage MPC**

L. Silletti, A. b. Wahid, P. Balla, E. Escoto, K. Horn, L. Winkelmann, V. Wanie, A. Trabattoni, F. Calegari and C. M. Heyl  
Atto-FEL 2022, London (2022) - Poster

4. **Sub-20 fs single-stage post-compression of an Ytterbium fiber laser**

L. Silletti, A. b. Wahid, P. Balla, E. Escoto, K. Horn, V. Wanie, A. Trabattoni, F. Calegari and C. M. Heyl  
High-Intensity Lasers and High-Field Phenomena (HILAS), Budapest (2022) - Oral presentation

5. **Single-stage post-compression of an Ytterbium fiber laser down to 20 fs**

L. Silletti, P. Balla, E. Escoto, K. Horn, V. Wanie, A. Trabattoni, F. Calegari and C. M. Heyl  
Frontieres in Optics (FiO), virtual (2021) - Poster

## Declaration on oath

I hereby declare and affirm that this doctoral dissertation is my own work and that I have not used any aids and sources other than those indicated.

If electronic resources based on generative artificial intelligence (gAI) were used in the course of writing this dissertation, I confirm that my own work was the main and value-adding contribution and that complete documentation of all resources used is available in accordance with good scientific practice. I am responsible for any erroneous or distorted content, incorrect references, violations of data protection and copyright law or plagiarism that may have been generated by the gAI.

24.09.2024

Date



Signature of doctoral candidate